KIEL UNIVERSITY

DOCTORAL THESIS

Characterization of Magnetization Dynamics in Structured Magnetic Films

---

A dissertation by:
Babak Mozooni

Supervisor:
Prof. Dr.-Ing. Jeffrey McCord

A thesis submitted in fulfillment of the requirements
for the degree of "Doktor der Ingenieurwissenschaften (Dr.-Ing.)" in

Materials Science and Engineering

Institute for Materials Science
2019

Dedicated to
the scientists who are promoting world peace

Declaration of Authorship

I herewith declare that all work presented in this thesis is my own and no other sources than those cited or explicitly mentioned were used.

Signature: ____

Date: ____

Reviewers:

Prof. Dr.-Ing. Jeffrey McCord

Prof. Dr. Christine Selhuber-Unkel

Prof. Dr. Rainer Adelung

Prof. Dr. rer. nat. Franz Faupel

Date for the oral exam: 26.06.2019

"*Don't you know Yet? It is your light that lights the World.*"

Rumi

Abstract

The focus of this thesis is investigating of the magnetization dynamics in patterned magnetic films by time-resolved Kerr microscopy (TR-MOKE). Therefore, various magnetic films and structures are studied using the developed TR-MOKE and inductive microwave magnetometry setup. The results of this thesis reveal new aspects of complicated magnetization dynamics in such magnetic systems. Also, it provides the knowledge of tailoring dynamic magnetic properties of modern magnetic structures.

Initially, the magneto-dynamic response of Landau-like magnetic domain configurations are examined and a method to separate the in- and out-of-plane Kerr signals is proposed. This method indicates a more elaborated model for fast magnetization processes in soft magnetic elements.

In addition, the direct observation of spin-wave generation and propagation from oscillating pinned magnetic structures is reported, and the fundamental properties of them are analyzed. Using this knowledge, an alternative way to generate and propagate spin waves that do not require any artificial structure (e.g., antenna or wave-guide) is proposed. Moreover, the results of experimental TR-MOKE imaging together with complementary micromagnetic simulations were used to design an experiment, where the spin waves are emitting from magnetic elements corners and edges. The frequencies of such spin waves shown to be tunable by the excitation frequency.

Finally, the dynamic magnetic response of weak antiferromagnetically coupled and structured magnetic films are presented. The multilayer film dynamic properties are compared to the single-layer film, and the impact of patterning on magnetization dynamics is shown.

Acknowledgments

I want to convey my most grateful to my family for their supports and encouragement on every step of my life. My parents and my two brothers Mohammad and Soroush are my life treasures.

I take this opportunity to express my heartfelt gratitude to Prof. Dr.-Ing. Jeffrey McCord; group leader of Nanoscale Magnetic Materials - Magnetic Domains (Nanomag) group of Kiel University. Prof. McCord offered me the opportunity of being his first doctoral student at Kiel University. Prof. McCord, as the supervisor of this project, gave his abundantly helpful and precious guidance in all phases of the project from practical activities to theoretical discussions.

Moreover, I need to thank Dr. Thomas von Hofe, for sharing his ideas, knowledge, and also for his invaluable assists during the first year of this project. Most of the hands-on lithographically skills that I used to conduct this research are what I learned from Dr. von Hofe.

In addition, I would like to thank Dipl.-Ing. Wolfgang Taute for building the coplanar waveguide used in this project, A. Gerber and I. Mönch for preparing the sample used in Chapter 4 and Chapter 5, Mathis Lohman for performing the simulations shown in Chapter 6 during his student job at Nanomag group and Cai Müller for our scientific discussions.

I also want to use these words to value my friendship with Dr. Ahmed Zayed that lasts for more than ten years, and I am sure it will last a lifetime.

Last but not the least, I like to thank, Dr. Onur Urs, Dr. Rasmus Holländer, Dr. Mikhail Kustov, Cai Müller, Julia Trützschler, Farzaneh Karimian, Umer Sajjad, Kadir Sentosun and Shayan Deldar for being great colleagues and friends during the four years of my stay at Nanomag group.

Babak Mozooni

Contents

List of Figures

Chapter 1

Introduction

The magnetization dynamics knowledge of structured magnetic thin films plays a significant role in development of various modern electronic devices such as magnetic storage media [1, 2, 3], magnetic random access memories (MRAM) [4, 5, 6] and microwave instruments [7, 8]. In recent years there has been a growing interest in new magnetic elements that can comply with the requirements of electronic components size shrinkage. A smaller electronic piece will lead to a faster processing time as well as lower energy consumption. All these require a deep understanding of rapid magnetic processes in magnetic media. Therefore, the understanding of magnetization dynamics is the key to fabricate new types of magnetic devices with novel and tunable properties, which was not feasible with conventional magnetic materials. Periodically structured magnetic films are an example of these new magnetic classes. Magnetic films use elementary spin excitations (magnons) to store or carry information [9, 10, 11]. Such development can be achieved by merging the physics of magnetization dynamics with top-down materials fabrication methods.

Another recent notable development in this realm is the emergence of spintronic devices [12, 13, 14, 15] such as spin-wave logic tools, signal processors or instruments using spin currents [16]. The fundamental property of spin waves (SWs) is their high propagation velocity, which makes them well suited for future ultrafast re-programmable and data storage devices [10, 13]. Spin waves can also contribute to high-frequency applications such as thin film inductors [17].

In practice, usage of spin waves requires a precise method to control spin waves excitation and propagation, which in turn demands a deep understanding of these magnetic phenomena.

Moreover, with the growing rate of data generation, new magnetic storage tools are needed. An example of these new magnetic storage devices is racetrack memory (domain-wall memory). Racetrack memory is a type of non-volatile storage system, which was firstly introduced by Parkin et al. in IBM [18, 19]. Racetrack memory is made out of a series of ferromagnetic nanowires with a specific number of magnetic domains that are acting as data bits. By passing a spin-polarized current through nanowires, due to the spin-transfer torque effect, magnetic domains move towards a reading head where magnetic domains' stray fields are detected. The racetrack memories are capable of having large storage capacity compared to mainstream storage drives though with approximately 10,000 times faster read/write performance, as well as much lower energy consumption. The two main challenges for producing racetrack memories are first the need for highly precise and reliable controlling of domains movement forward and backward in nanowires and second, the low speed of the movement of the magnetic domains. Therefore, understanding the physics of the magnetic domain and wall dynamics is vital.

In addition to the new storage technologies, conventional non-volatile storage devices such as magnetoresistive random access memory (MRAM) are still a subject of development. This demands extensive knowledge of high-speed magnetic phenomena [5]. An MRAM contains spin valves (data cells) with two ferromagnetic layers separated by a non-magnetic tunnel barrier. One of the ferromagnetic layers can alter its magnetization direction freely while the other layers' magnetization is coupled and pinned to an anti-ferromagnetic film. Data bits are then stored as the relative orientation of the magnetization of two magnetic layers. There are two possible relative magnetization directions of ferromagnetic layers, i.e., parallel or antiparallel alignments. Each of these configurations has a different resistivity (the parallel configuration has a lower resistivity) that can be detected by a reading head and later translated to "0" and "1" bits.

These exemplary applications and similar ones are the deriving force of many dynamic magnetization related research projects. To study dynamic magnetic phenomena, in this project a dynamic magneto-optical Kerr effect microscope (MOKE) is developed, which can be used to study dynamic magnetization process from nano-second down to picosecond temporal resolution. Figure 1.1 displays selected magneto dynamics phenomena and their relevant temporal dimensions. As can be seen in Fig. 1.1, domain wall motion is a rather slow process that occurs in a time scale of a few ns to a hundred μs, whereas the magnetization precession takes place in few ps. The fastest processes are exchange interactions which are fs processes.

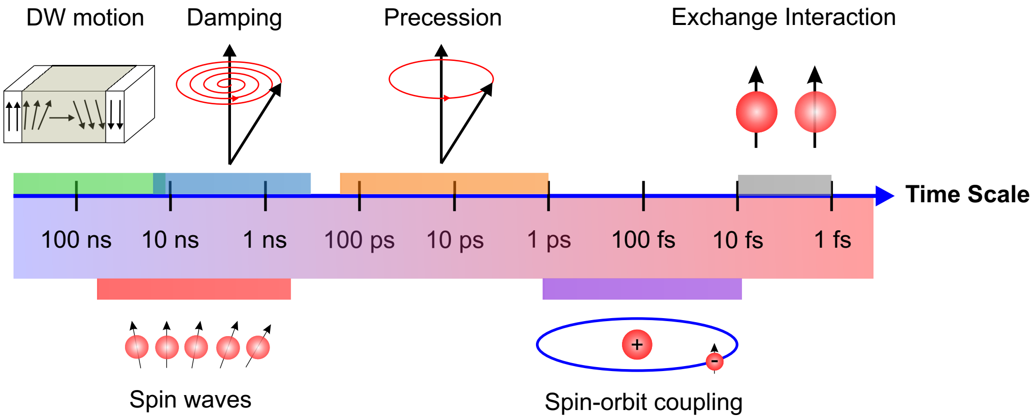

Figure 1.1: Schematic draw showing typical time scales of different dynamic magnetic processes (adapted from [20]).

In this thesis, the dynamic magnetization behavior of artificially generated magnetic domains and domain walls configurations in large area structured magnetic thin film is examined. The temporal resolution of interest in this project is the picosecond time scale and above (fs processes are beyond the scope of this work). By introducing various magnetization configurations, the effective dynamic magnetic properties are investigated. Periodic magnetic nanostructures are created by using the photolithography process. Such structures provide variable magnetic configurations. As mentioned, in this project, the lateral magnetization distribution is imaged by time-resolved high-resolution magneto-optical Kerr microscopy (TR-MOKE). Up to now, many efforts are made to observe the high-frequency (hf) response of magnetic structured films [21, 22], including x-ray transmission microscopy [23, 24], optical pump-probe [25], time-resolved scanning Kerr microscopy [26, 27], polarized neutron reflectivity [28, 29], Lorentz microscopy [30, 31], brillouin light scattering [32, 33, 34, 35], ferromagnetic resonance (FMR) [36, 37] and spin-wave resonance (SWR) [38]. During this project, in the "Nanoscale Magnetic Materials - Magnetic Domains" group of Kiel University, a state-of-the-art time-resolved Kerr microscope (TR-MOKE) with a temporal resolution in the picosecond range was designed and assembled. This magneto-optical method can be a complementary or an alternative to the above-mentioned methods.

Unlike the previously mentioned techniques, which use a pulsed-field or laser pulses to trigger the magnetodynamics response of magnetic elements, in the developed TR-MOKE here, a continues AC field excitation is used.

It should be noted that most of the magneto-optical methods are based on the application of the Kerr effect (MOKE). A conventional time-resolved imaging method is scanning Kerr microscopy [39, 40, 41, 42, 43], which is using nano-, pico- or femtosecond pulsed laser systems to probe the magnetic sample. The alternative method used in this work (TR-MOKE) has a shorter image acquisition time and higher flexibility in terms of the field of view [44, 45]. However, due to the adversity of obtaining a high signal-to-noise ratio, TR-MOKE is less common. The low signal-to-noise ratio of TR-MOKE is mainly due to the occurrence of laser speckles, in which its residual contrast can cover the low magneto-optical signals. In addition, TR-MOKE is highly sensitive to environmental parameters such as external vibrations or temperature gradients. The method shown in this thesis uses a very stable design that overcomes these obstacles.

The developed TR-MOKE of this work is used together with quasi-static and dynamic measurement techniques to obtain a complete picture of the lateral varying magneto-dynamic processes up to several GHz. The method is used to investigate the local magnetic domain and domain wall response of amorphous magnetic film elements at various frequencies. Also, other complicated dynamic magnetic responses such as localized switching events, domain wall induced effects, and the possibility of generating and imaging of spin waves (SWs) emitted from resonating magnetic domain walls, are investigated.

In addition to the imaging technique, to quantify the dynamic magnetization response, a pulsed inductive microwave magnetometer (PIMM) is being built and used in conjunction with TR-MOKE.

In the following chapters, the details of measurement techniques, as well as the results of such measurements are shown.

Chapter 2

Theoretical Background

2.1 Ferromagnetism

The presence of spontaneous magnetization in different regions of a magnetic body is called ferromagnetism and materials that show such behavior are ferromagnetic materials. Regions with uniformly aligned magnetic moments are known as magnetic domains and are separated from adjacent domains by a tiny border known as magnetic domain walls. In contrast to magnetic domains, in a domain wall, the magnetic moments gradually change. In 1906 Weiss initially introduced the concept of the magnetic domain in ferromagnetic materials [46] with the mean field theory. Weiss's theory was then extended by Heisenberg [47], Barkhausen [48] and Bloch [49] who presented other pieces of magnetic domain theory. However, the experimental proof of the existence of magnetic domains is demonstrated by Bitter in 1931 [50]. In 1935, Landau and Lifshitz [51] explained the phenomena of the formation of magnetic domains to minimize the total magnetic energy. The total magnetic energy of a magnetic body is made out of different energy contributions and can be written as:

$$E_{tot} = \int_V [\underbrace{E_{ex}(m)}_{\text{exchange energy}} + \underbrace{E_{an}(m)}_{\text{anisotropy energy}} - \underbrace{H_{ext}M}_{\text{zeeman energy}} - \underbrace{\frac{1}{2}H_d M]}_{\text{stray field}} \, dV \tag{2.1}$$

Where M is the local magnetization vector. The detailed description of each energy terms in Eq. 2.1 are presented in the following sections.

2.1.1 Exchange Stiffness Energy

In 1928, Heisenberg described a non-classical force known as exchange stiffness force, which depends on the relative alignments of spins of the two electrons. Due to the existence of exchange forces when two electrons' spins are in antiparallel configuration, electrons attract each other while a parallel spins configuration causes a repulsion force between two electrons. Considering atoms i and j with a spin angular momentum of $S_i h/2\pi$ and $S_j h/2\pi$, the exchange energy between these two atoms can be written as [52]:

$$E_{ex} = -2J_{ex}SiSj = -2J_{ex}SiSjcos\phi \tag{2.2}$$

Where J_{ex} is the exchange integral, and ϕ is the angle between two spins. Since $J_{ex} > 0$ for a parallel alignment of spins ($\phi = 0$), therefore the E_{ex} is minimum. As a result, the exchange energy favors a parallel alignment of spins. Any deviation of magnetic moments from their parallel configuration causes an increase of exchange energy in the magnetic body. Such energy increase for a magnetic body with the volume of V can be written as:

$$E_{ex} = \int A(\nabla\vec{m}(r))^2 dV, \tag{2.3}$$

Where A is the exchange constant and $m = M/M_s$ [53], M is the magnetization of sample and M_s is the saturation magnetization.

2.1.2 Anisotropy Energy

Magnetic anisotropy is the existence of an energetically favored magnetization direction in a magnetic material. In ferromagnetic materials the direction of spontaneous magnetization is called easy anisotropy axis (e.a.) of magnetization, while the perpendicular direction to that is known as hard anisotropy axis (h.a.) of magnetization. Due to the existence of the magnetic anisotropy, the magnetic body exhibits directional magnetic properties [52]. The sources of magnetic anisotropy are described in the next sections.

2.1.2.1 Magnetocrystalline Anisotropy

Magnetocrystalline anisotropy is an intrinsic property of crystalline ferromagnets. This type of magnetic anisotropy is originating from spin-orbit coupling, considering an external magnetic field's tendency to alter the spin of an electron. By changing of electron's spin, the orbital of the electron is reoriented. Due to the strong coupling between orbital and lattice, the electron's orbital is pinned to the lattice. Since the coupling between orbital and lattice is stronger than the spin to the orbital, to overcome the anisotropy energy, the external field should overcome the spin-orbit coupling energy [52]. On an atomic scale, this causes a tendency for magnetization to be aligned along with specific crystallographical directions.

The magnetic anisotropy E is expressed with regard to the anisotropy constant K_i as:

$$E = \sum_i c_i K_i \tag{2.4}$$

Where c_i depends on the magnetic moments' direction. For a cubic crystal, the magnetocrystalline anisotropy can be written as [52]:

$$e_{Kc} = K_{c1}(m_1^2 m_2^2 + m_1^2 m_3^2 + m_2^2 m_3^2) + K_{c2} m_1^2 m_2^2 m_2^2 \tag{2.5}$$

Where K_{c1} and K_{c2} are the cubic anisotropy constants and m_i is the magnetization component along the cubic axis ($m_1 = \cos\theta \cos\phi$, $m_2 = \cos\theta \sin\phi$ and $m_3 = \sin\theta$). In a polar coordination the cubic anisotropy can be re-written as:

$$e_{Kc} = (K_{c1} + K_{c2}\sin^2\theta)\cos^4\theta\sin^2\phi\cos^2\phi + K_{c1}\sin^2\theta\cos^2\theta \tag{2.6}$$

Where θ and ϕ are the zenith and azimuth angles of the magnetization vector.

2.1.2.2 Shape Anisotropy

The expansion of a magnetic element in different directions can change the internal demagnetizing field, which is sensitive to the shape of the sample. In reality, the demagnetizing field in the short axis of the magnetic body is stronger [52] and therefore in an unsymmetrical magnetic body with no magnetocrystalline anisotropy, the sample's long axis is the easy anisotropy axis. Figure 2.1 shows a spheroidal sample. In such magnetic samples, the shape anisotropy constant K_s can be written as [52]:

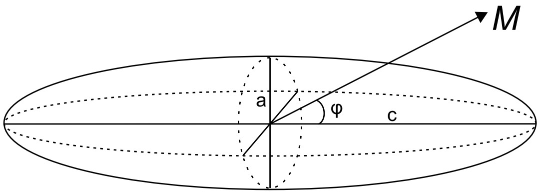

Figure 2.1: Schematic drawing of a spheroidal magnetic body (adapted from [52]).

$$K_s = \frac{1}{2}\mu_0(N_a - N_c)M^2 \tag{2.7}$$

Where N_a and N_c are demagnetization coefficient along a and c axises respectively and μ_0 is the vacuum permeability. Eq. 2.7 can also be written as:

$$K_s = \frac{1}{2}\mu_0 \Delta N M^2 \tag{2.8}$$

2.1.2.3 Stress Anisotropy

Stress anisotropy occurs via magnetoelastic coupling which energetically favors some magnetization directions [54]. This anisotropy depends on internal stress inside the magnetic body. Such a dependency causes a magnetostriction effect in the sample. Very similar to magnetocrystalline anisotropy, the origin of magnetostriction effect is due to spin-orbit coupling [53].

2.1.2.4 Induced Anisotropy

For many practical usages, it is essential to create an anisotropy direction in a controlled manner. The control of anisotropy direction can be done during film deposition or by thermal annealing in the presence of an external magnetic field. Such treatments induce an easy anisotropy direction in the sample and are therefore known as induced anisotropy. For thermal annealing, it is essential to note that the process of annealing is done in a temperature range below the sample's currie temperature (Tc).

The anisotropy can also be varied locally by utilizing an ion irradiation process in a magnetic field. A detailed review of ion irradiation anisotropy tailoring can be found in Ref. [55].

2.1.3 Zeeman Energy

Zeeman energy contribution refers to the interaction of magnetic material with an external magnetic field. Zeeman energy can be calculated as follows:

$$E_z = -\mu_0 \int H_{ext} M \; dV \tag{2.9}$$

Where H_{ext} is the external field, M is the local magnetization, μ_0 is the vacuum permeability, and V is the volume of the magnetic body [56].

2.1.4 Stray Field Energy

Stray field energy (magnetostatic self-energy) is an energy contribution, which is created by a magnetic body itself [56]. The stray field energy can be calculated as follows:

$$E_d = \frac{1}{2}\mu_0 \int_{\text{out-side of sample}} H_s^2 \; dV = -\frac{1}{2}\mu_0 \int_{\text{in-side of sample}} H_d M \; dV \tag{2.10}$$

Where H_s and H_d are stray and demagnetizing fields respectively, and V is the volume of the magnetic body.

2.2 Magnetic Domains

To minimize the total energy of a block of ferromagnetic material, separated regions with uniform magnetic moment directions (M_s) form which, are known as magnetic domains. Figure 2.2 (a) shows a magnetized block with the stray field around and the demagnetizing field inside. As seen in Fig. 2.2 (b), by formation of magnetic domains, the magnetostatic energy is reduced, but still the magnetic poles exist on the surface of the block. Landau and Lifshitz suggested the domain model, in which with the formation of flux-closure domains

(Fig. 2.2 (c)) the magnetic body magnetostatic field is entirely reduced to zero. As displayed in Fig. 2.2 (c), by formation of flux-closure domains, the magnetic poles vanish, and therefore the magnetostatic field is reduced to zero.

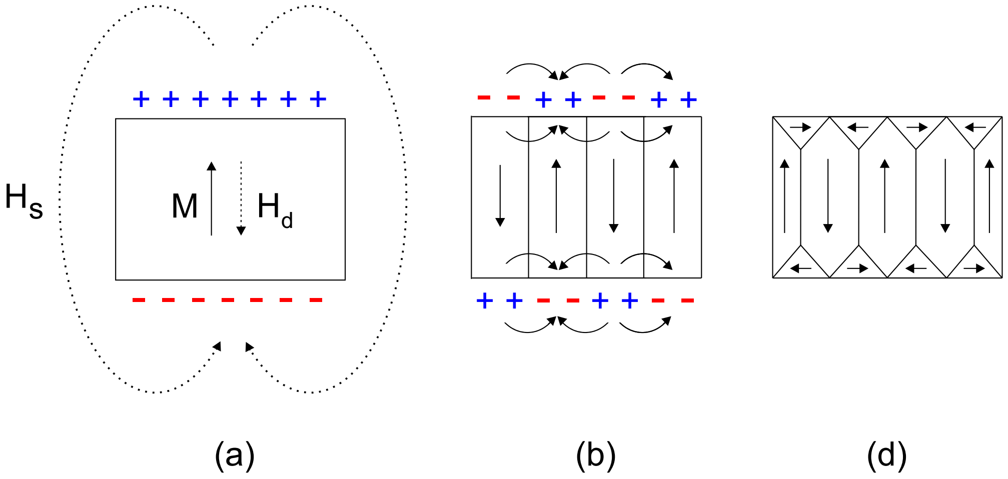

Figure 2.2: Flux-closure type domain, suggested by Landau and Lifshitz. As shown, the domains are aligned in a way to minimize the stray field energy (adapted from [57]).

2.3 Magnetic Domain Walls

Due to the existence of exchange stiffness energy, a sudden change of magnetic moments from one domain to the adjacent domain causes large exchange energy. Hence, instead of a sudden magnetic moment change, it changes gradually from one domain to its neighbor. The regions where the magnetization direction changes gradually are called the magnetic domain walls. The width of the domain wall depends on the exchange length ($l_{ex} = \sqrt{A/K}$) and can be calculated as followings: [56]:

$$\Delta_{DW} = \pi\sqrt{\frac{A}{K_u}} \tag{2.11}$$

Where Δ_{DW} is the domain wall width, "A" is the exchange stiffness constant and K_u is the uniaxial magnetic anisotropy.

As indicated in Eq. 2.11, while the exchange energy favors wider domain walls, the anisotropy energy tries to keep the domain width smaller.

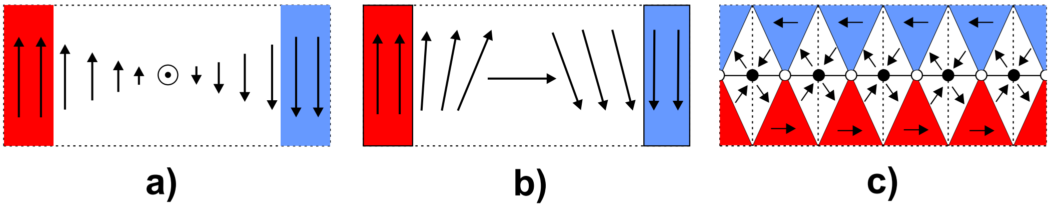

Figure 2.3: Schematic drawing of different domain wall types, (a) Bloch (b) Neel and (c) cross-tie domain walls (adapted from [58]).

Depending on the magnetic moment alignment inside the domain wall, three sorts of domain walls can form. When the magnetization $\vec{M}$ rotates perpendicularly to the domain wall cross-section the so-called Bloch domain wall forms. The cross-section of a Bloch domain wall is shown in Fig. 2.3 (a). In the case where the magnetization path inside the Bloch wall is not symmetric, and the surface distortion of the Bloch wall is a vortex, an asymmetric Bloch wall shapes [59]. When the rotation of $\vec{M}$ takes place in the cross-section of the wall, a Neel domain wall is made (Fig. 2.3 (b)). Another type of domain wall exists, which is a mixture of the Bloch and Neel walls, known as the cross tie domain wall. A schematic drawing of a cross tie wall is shown in Fig. 2.3 (c). The Bloch domain wall typically occurs in the magnetic film thickness of higher than 50 nm. In contrast, Neel's wall occurs in films with a thickness of less than 25 nm. At the intermediate film thickness range, i.e., between 25nm to 50nm cross tie domain walls form [59].

2.4 Magnetization Dynamics

To describe the switching process and time evolution of magnetization, a macrospin model is used [60]. The macrospin model assumes the magnetic moments are rotating coherently in a magnetic body and that the system consists of only one single spin. Ideally, the model can be used in magnetic systems where the exchange interaction is strong in a way that the system can be assumed as a single domain media. The disadvantage of such a model is that the contribution of the magnetic domain and domain wall or other local effects are eliminated. In other words, the macrospin model is restricting the degree of freedom to only zero-wave vector spin waves, and therefore just a homogeneous precession. Once the system is exposed to an external magnetic field, the perpendicular component of the magnetic field to the magnetic moment generates a torque. This torque acts as a deriving force that initiates the precessional magnetization motion around the effective field. The angular frequency of this precessional motion is $\omega = \gamma H_{eff}$. Once an alternating magnetic field with the same angular frequency of magnetization precession is applied, the resonance phenomena occur in which the magnetization absorbs the power from external AC field [53, 52]

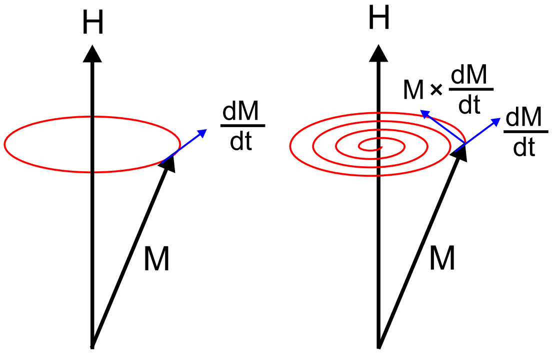

Figure 2.4: A schematic drawing displaying the magnetization precessional motion without (left) and with damping (right).

Theoretically, magnetization dynamics in a magnetic film subjected to an effective magnetic field of H_{eff} can be described by Landau-Lifshitz-Gilbert

(LLG) equation as follow [51]:

$$\frac{\partial M}{\partial t} = -\gamma\mu_0 M \times H_{\text{eff}} + \frac{\alpha}{M_{\text{s}}}(M \times \frac{\partial M}{\partial t}) \ , \tag{2.12}$$

Where μ_0 =$4\pi \times 10^6$ Vs/Am is the vacuum permeability, $\gamma = 1.76 \times 10^{11} T^{-1} s^{-1}$ is the gyromagnetic ratio, M_{s} is the saturation magnetization, and α is the damping parameter. The first term in Eq. 2.12 corresponds to gyroscopic precession with a characteristic resonance frequency f_{res} that is dependent on the effective magnetic field H_{eff}, which can be calculated by simplified Kittel's equation as [61]:

$$f_{res}^2 = (\frac{\gamma\mu_0}{2\pi})^2 M_s H_{eff}, \tag{2.13}$$

The effective field H_{eff} is made from the contribution of anisotropy field H_{an}, dipolar field H_{dipol}, exchange field H_{ex}, and external magnetic field H_{bias} and can be written as:

$$H_{eff} = H_{an} + H_{dipol} + H_{ex} + H_{bias} \tag{2.14}$$

The second term in Eq. 2.12 refers to the phenomenological damping torque. Eq. 2.12 can accurately explain the magnetization dynamics in continues magnetic films. However, by structuring the film, and by the appearance of local demagnetization effects as well as magnetic domain formation, the dynamic response deviates from the LLG equation. Despite the complicated magneto-dynamic behavior of structured magnetic films, it should be noted that H_{eff} in both the LLG and non-LLG magnetic responses strongly depends on the anisotropy field. Therefore, magnetization dynamics in ferromagnetic materials are highly dependent on magnetic anisotropy [62]. Hence, changing the magnetic anisotropy is a way of tailoring magnetization dynamics, which can be done by magnetic film structuring or magnetic film inter-coupling by using multilayer thin films.

In a simple case when there is a strong exchange coupling between adjacent magnetic moments (inside a magnetic domain), by applying an external torque, all the magnetic moments start to precess (Fig. 2.4) in phase with each other. Therefore, a homogeneous precession of magnetization in the domains occurs. However, due to the local distribution of the effective field, instead of a homogeneous precession of magnetic moments, the precession of spins occurs in different phases, though with a fixed relative phase shift with each other. Such a magnetic moment movement is called a spin-wave, and the quantum of spin-wave is called magnon. Spin waves can be categorized by the orientation of their wave vector to $\vec{M}$. In this manner when $\vec{M}$ is in-plane and $\vec{k} \parallel \vec{M}$ ($\vec{k}$ is the wave vector), the magnetostatic surface wave (MSSW) mode or Damon-Eshbach modes form [63]. The frequency of Damon-Eschbach mode can be calculated as follows:

$$f_{DE} = 2\pi\gamma\sqrt{H(H + 4\pi M_s) + (2\pi M_s)(1 - e^{-2kd})} \tag{2.15}$$

when the $\vec{k} = 0$ the Eq. 2.15 can be written as:

$$(f_{DE})_{k=0} = 2\pi\gamma\sqrt{H(H + 4\pi M_s)} \tag{2.16}$$

Which corresponds to the Kittel mode. Unlike the Damon-Eshbach modes, there are two other types of spin waves, which propagate in the volume of the magnetic element, and therefore, they are volume modes. In this case when $\vec{k} \parallel \vec{M}$, the backward volume magnetostatic (BWVM) mode is formed, and when $\vec{M}$ is out of plane of the film, and $\vec{k}$ lies in the plane of film, it is known as forward volume magnetostatic (FWVM) mode.

For the backward volume magnetostatic mode, the dispersion equation can be written as:

$$f_{BWVM} = 2\pi\gamma\sqrt{H(H + 4\pi M_s(\frac{1 - e^{-2kd}}{kd}))} \tag{2.17}$$

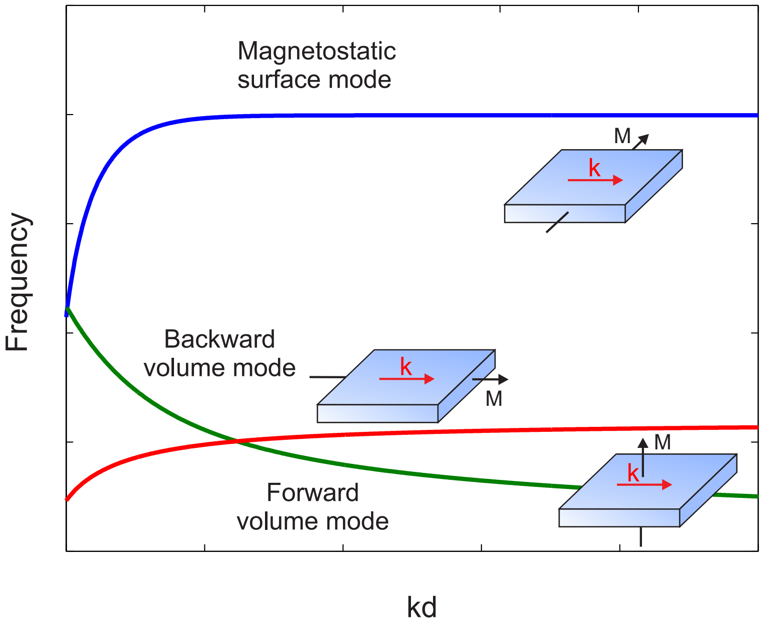

Figure 2.5: A schematic diagram of dispersions of different magnetostatic spin-wave modes (adapted from [64]).

and for the forward volume magnetostaic mode:

$$f_{FWVM} = 2\pi\gamma\sqrt{(H - 4\pi M_s)(H - 4\pi M_s(\frac{1 - e^{-2kd}}{kd}))} \tag{2.18}$$

It should be noted that Eq. 2.15 - 2.18 are based on the assumption that there is no contribution of anisotropy [33] in the magnetic element. Figure 2.5 shows the frequency behavior of different spin-wave modes depending on kd parameter, where "k" is the wave vector, and "d" is the film thickness.

Chapter 3

Experimental

3.1 Magnetic Film Structuring

In order to create micro-scale structures in magnetic films, positive or negative photolithography processes are used. To do so, in the framework of this project, four different 5 inches × 5 inches lithography reticles were designed by the author and produced in an external mask-shop. Each reticle contains 60 different 1 cm × 1 cm fields, and the magnetic elements are placed in these fields. All the reticles have positive polarity.

To create positive structures (e.g., dot arrays), the positive photolithography process is used. The lithography process is performed in the "Kieler-Nanolab" at Kiel University. The designed photolithography process includes the following steps:

- Drying the silicon wafer for 10 minutes on a hot plate at 120 °C. This eliminates any possible moisture from the surface of the wafer.
- Coating the wafer with a highly purified grade hexamethyldisilazane (HMDS), which promotes the adhesion of the surface.
- Spin-coating of 1.75 ml of AR-U 4060 image reversal photo-resist on the wafer. The spin coating is accomplished by using a rotating speed of 8000 rpm for 35 sec.

- Soft-backing of resist on the hot plate at 100 °C for 100 sec.
- Exposing the wafer to an UV light using a mask aligner exposure tool with an energy dose of 32.9 mW/cm^2. To maintain the structure size precession, the vacuum mode is used.
- Resist development by AR 300-47 diluted solution for 35 sec.
- Hard-backing on a hotplate for 120 sec at 110 °C
- To remove the residual resist from the areas that the developer cannot penetrate, a further plasma etching process is performed. The plasma etching is executed by using O_2 with a chamber pressure of 4.3×10^{-1} for 10 sec and power of 100 W.
- Ion beam etching with a plasma power of 1000 W, beam current of 350 mA and a voltage of 400 V.
- Resist removal by an N-Methylpyrrolidinone (NMP) solution in an ultrasonic bath.

The negative process is performed in the same manner. The only difference is adding an image-reversal baking step (240 sec at 120 °C) and a flood exposure step with an increased developing time with a total of 70 sec.

3.2 Magnetic Samples

In this thesis, three types of magnetic films with various structures are used. The sample used in Chapter 4 and Chapter 5 is an amorphous $(Fe_{90}Co_{10})_{78}Si_{12}B_{10}$ film with a thickness of d = 160 nm. The sample is deposited on a transparent glass wafer through the rf sputtering technique. During the deposition, an in-plane external magnetic field of 8 kA/m is applied, which leads to an induced uniaxial anisotropy. The film is structured to square elements with an edge length of 40 μm and an element separation of 10 μm.

The experiment performed in Chapter 6 is on a patterned soft magnetic $Ni_{81}Fe_{19}$ thin-film, which is deposited on a transparent glass substrate. The sample, with a dimension of 1 cm × 1 cm, was patterned into 30 μm × 30 μm tilted square magnetic elements allowing for simultaneous microscopic characterization of multiple elements.

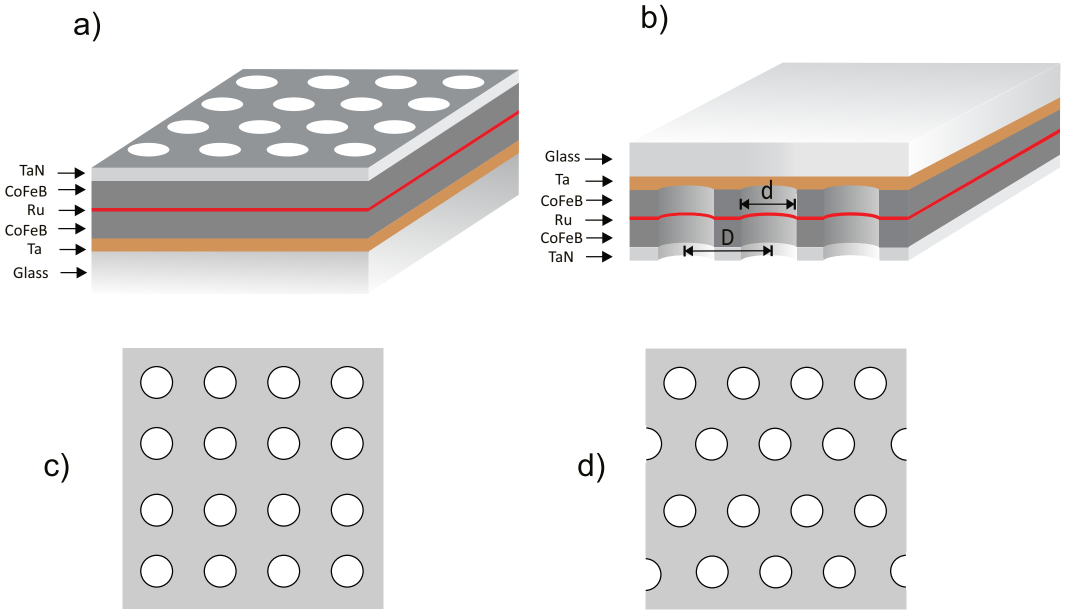

Figure 3.1: (a) Schematic drawing of a patterned multilayer sample. (b) The cross section of the film is up side down. (c) and (d) the square and hexagonal packing of antidot with a diameter of d = 4 μm and antidot arrays center-to-center distance of D = 16 μm respectively.

In Chapter 7, a single layer Ta (3nm)/($Co_{40}Fe_{40}B_{20}$) (50nm)/TaN (5nm) and an antiferomagnetically coupled Ta (3nm)/($Co_{40}Fe_{40}B_{20}$) (25nm)/Ru (0.8nm)/($Co_{40}Fe_{40}B_{20}$) (25nm)/TaN (5nm) film were deposited on a glass substrate with an induced in-plane anisotropy applied during film deposition. Using photolithography technique, samples are structured in to antidot arrays with various sizes, center-to-center distance and arrangement. The diameter of antidotes is d = 4 μm or d = 10 μm with a center-to-center distance (D) of 3×d or 4×d or 10×d, with square and hexagonal packing of antidot on the film surface. Figure. 3.1 displays the schematic arrangement of antidots on multilayer films.

3.3 Coplanar Waveguide

In order to deliver the high-frequency excitation field to the surface of the samples, a coplanar waveguide with the central wire width of 150 μm and a thickness of 17.5 μm, is built. When a current signal passes through the central wire of the waveguide, it generates a magnetic field in the transversal direction. To avoid any possible impedance mismatch in the measurement circuits, the waveguide and all the connectors and cables have an impedance of 50 Ω. Figure 3.2 illustrates the cross-section of the coplanar waveguide and the way that the magnetic sample is placed on it.

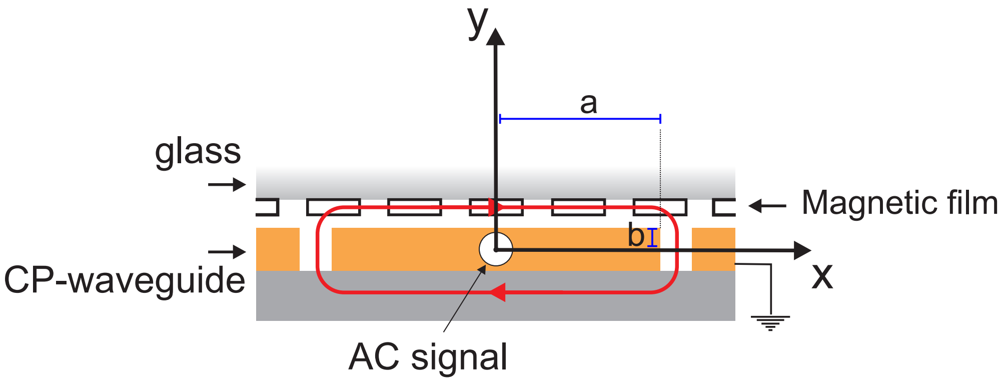

Figure 3.2: Schematic drawing of the cross section of the coplanar waveguide and the way that the sample is positioned on top. The red arrow shows the generated magnetic field (adapted from [65]).

The amplitude of excitation field generated by coplanar waveguide is calculated using the method introduced in Ref. [44]. Considering the radial field around a strip-line with a current density of j is [44]:

$$dH(X,Y) = \frac{j\ dxdy}{2\pi r} = \frac{I\ dxdy}{8\pi ab\sqrt{(x-X)^2+(y-Y)^2}} \tag{3.1}$$

Where "a" and "b" are the distance from the center of waveguide along x and y directions respectively. "I" is the current passing through the waveguide. The magnetic field along the x-axis can be written as [44]:

$$
\begin{aligned}
H_x = \frac{-I}{8\pi ab} u[\frac{1}{2} ln(\frac{g^2+u^2}{h^2+u^2}) + \frac{g}{u} arctan\frac{u}{g} - \frac{h}{u} arctan\frac{u}{h}] \\
- [v\frac{1}{2} ln(\frac{g^2+v^2}{v^2+h^2}) + \frac{g}{v} arctan(\frac{v}{g}) - \frac{h}{v} arctan(\frac{v}{h})]
\end{aligned}
\tag{3.2}
$$

Similarly, the out-of-plane field (field along the y-axis) can be written as [44]:

$$
\begin{aligned}
H_y = \frac{I}{8\pi ab} g[\frac{1}{2} ln(\frac{g^2+u^2}{v^2+g^2}) + \frac{u}{g} arctan\frac{g}{u} - \frac{v}{g} arctan\frac{g}{v}] \\
- [h\frac{1}{2} ln(\frac{u^2+h^2}{v^2+h^2}) + \frac{u}{h} arctan(\frac{h}{u}) - \frac{v}{h} arctan(\frac{h}{v})]
\end{aligned}
\tag{3.3}
$$

where

$$u = a - X \tag{3.4}$$

$$v = -a - X \tag{3.5}$$

$$g = b - Y \tag{3.6}$$

$$h = -b - Y \tag{3.7}$$

Using Eq. 3.2 and 3.3 the generated field around the waveguide is calculated and plotted in Fig. 3.3.

3.4 Magneto-optical Kerr Effect

In 1854, Michael Faraday discovered when the light passes through a pair of magnetic poles, the polarization plane of light rotates. Based on Faraday's

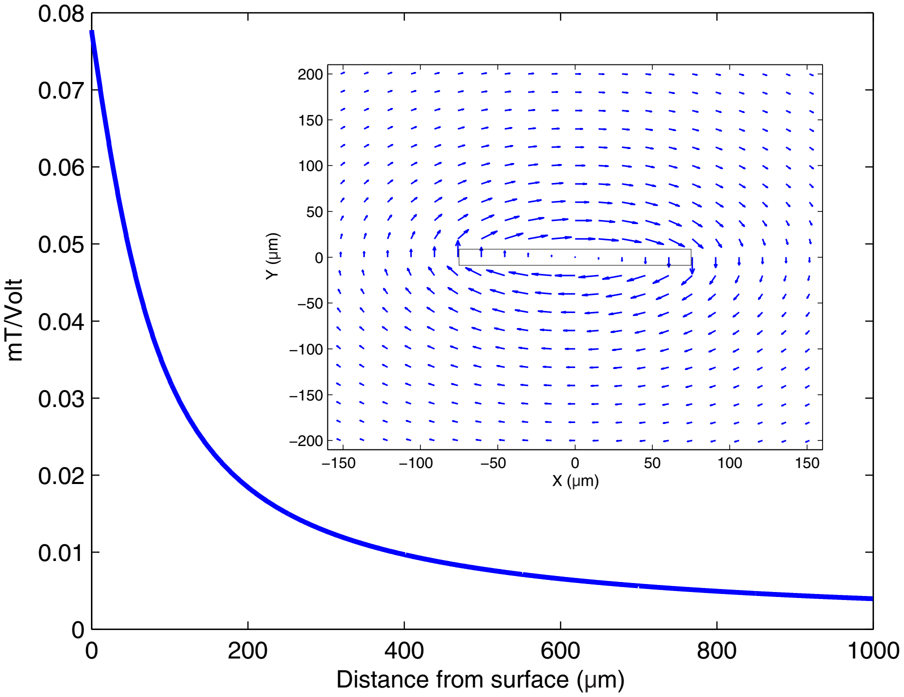

Figure 3.3: Calculated magnetic field in-plane component amplitude at the central point of the coplanar waveguide at various distances from the wave guide's surface (a coplanar waveguide with a width of 150μm). Inset Magnetic field orientation and amplitude of magnetic field generated by the wave guide.

observation, in 1877, John Kerr introduced the magneto-optical Kerr effect [66], which is the rotation of the polarization plane of a linearly polarized light when it is reflected from the surface of a magnetic element. Such rotation of light's plane of polarization can be detected by a polarizing microscope [56]. The appearance of Kerr effect is due to the Zeeman exchange splitting of the electron levels when exposed to a magnetic field [67] . When this appears with transmitted light, it is called the Faraday effect. It should be noted that the Kerr effect is a surface effect and, its depth of penetration is limited to approximately a few ten nanometers. Therefore, any magnetometry technique that is based on the magneto-optical Kerr effect only contains the information of the magnetic statues of the surface of the magnetic film.

The change of plane of polarization is shown in Fig. 3.4 (a-c). This

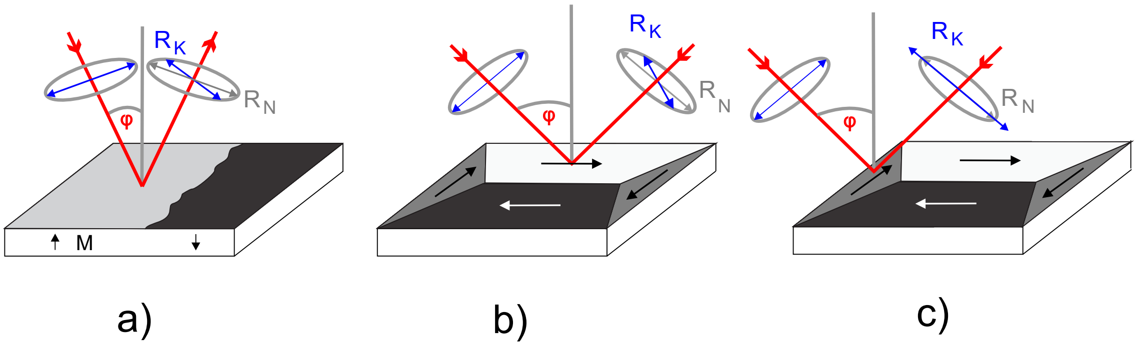

Figure 3.4: Geometries of different Kerr effect configuration. Depending on the magnetization direction and plane of incidence (a) polar, (b) longitudinal or (c) transverse geometry are generated (adapted from [58]). R_N and R_k are showing the normally reflected light and Kerr amplitudes, respectively.

Zeeman exchange splitting causes an additional component (Kerr amplitude R_K), which is transversal to the normally reflected amplitude R_N. Using an analyzer in front of the reflected light, the light amplitude of light passing through the analyzer can be calculated using Malus' law [68]:

$$I = I_0 \, cos^2\theta \tag{3.8}$$

Where I_0 indicates the reflected light intensity before entering the analyzer, and θ is the angle between the reflected light plane of polarization and the plane of the analyzer. As the Kerr effect is relatively weak, it is imperative to use an adequate bright light source. It should be noted that only p-polarized light can cause a transversal Kerr effect, and in this case, there is no rotation of the plane of polarization, however, the amplitude of the reflected light changes. Therefore, the transversal configuration is usable in the Kerr effect magnetometry but not in the direct Kerr effect magnetic domain imaging.

There are three main configurations of Kerr effect that can be distinguished depending on the light relative angle of incidence with the orientation of magnetization. Figure 3.4 (a) shows the configuration of the polar Kerr effect. The polar Kerr effect occurs when the sample has an out-of-plane magnetization, and the light angle of incidence is ϕ=0. When the magnetic field components lay in the plane of the film, two possibilities can occur. In the case where there is an oblique angle of incidence between the light and surface of the film (Fig. 3.4 (b)), the longitudinal Kerr effect configuration forms. When the magnetization is in the plane of the film and is perpendicular to the incidence plane of the light Fig. 3.4 (c), the transversal Kerr effect is built.

3.5 Time Resolved Kerr Microscopy

To study the lateral dynamic response of magnetic structured films, during this project, a new state-of-the-art stroboscopic time-resolved wide-field Kerr microscope with picosecond temporal resolution was developed [69]. A schematic drawing of the TR-MOKE setup is displayed in Fig. 3.5. The high temporal resolution of the setup is achieved by using a mode-locked diode-pumped and frequency-doubled Nd:YVO4 laser as the illumination source. The laser has a wavelength of λ=516nm with a pulse width of 7 ps and a fixed repetition rate of 50 MHz.The average output power of the laser, according to the producer specifications is approximately 150 mW. The laser light is sent to the microscope through a multi-mode optical fiber with a numerical aperture of NA = 0.5, a diameter of 1 mm, and a length of 1 m [69].

In order to obtain the in-plane and out-of-plane magnetization components, the microscope sensitivity is adjusted by focusing the optical fiber output on different positions in the back focal plane of the objective lens. Adjusting the position of the fiber output will change the plane of incidence light [70], and therefore the out-of-plane (polar) and in-plane (longitudinal) magneto-optical contrasts can be obtained [69]. When performing the imaging, the sample is placed upside down on the coplanar waveguide, which is then excited by an AC magnetic field (Fig. 3.6).

The precise focusing ability of the microscope is obtained using an objective lens with a correction ring is used. This allows focusing onto the magnetic

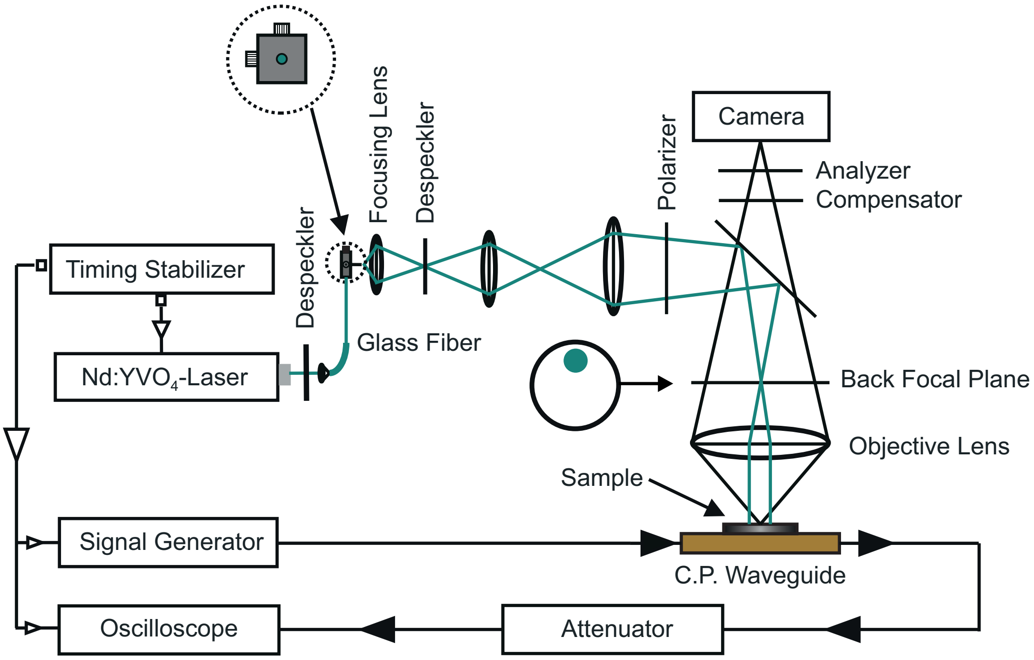

Figure 3.5: The schematic drawing of TR-MOKE setup, which consists of a mode-locked laser (illumination source), a magneto-optical Kerr microscope, and an AC magnetic field excitation source. The light source and AC field generator are triggered by the same clock to create a jitter-free measurement. The whole setup is computer controlled using a LabView user interface (adapted from [69]).

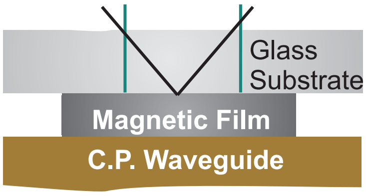

Figure 3.6: The schematic diagram shows the way that magnetic elements are positioned relative to the coplanar waveguide used in the TR-MOKE (adapted from [69]).

film surface through the glass substrate. In addition, such a lens can increase the available working distance. Therefore there would be a larger space between sample and lens, which is a critical requirement for imaging of magnetic samples with wire-bonding. The lateral resolution of the TR-MOKE set up is limited to 400 nm. To overcome the speckle patterns induced by laser coherency, two de-specklers are used. The first de-speckler (a rotating glass plate), with adjustable speed, is placed between the laser output and optical fiber input, and the second de-speckler with a vibrating polymeric plate is placed after the output of optical fiber and before the microscope input.

To increase the maximum excitation field amplitude, an amplifier with a bandwidth of 4 GHz and a maximum power of 5 W is used. As mentioned before, the high-frequency signal is converted to an AC field when it passes through the coplanar waveguide (see section 3.3). Both the signal generator and the laser are running from the same reference signal. The 50 MHz clock of the laser is derived from higher harmonics of the 10 MHz clock signal for the high frequency field excitation source [69]. This leads to a timing jitter of fewer than 0.5 ps.

The images obtained by the microscope are recorded using a digital CCD camera with a frame rate of 16 Hz. The TR-MOKE imaging is performed in a stroboscopic differential imaging manner. This is done by changing the AC field phases between the excitation field and the imaging laser pulse. Individual differential images (Δ) are obtained from subtracting two magnetization states with a phase shift of π [69]. The imaging is done using the following sequence:

- Taking a background image at a given AC magnetic field phase.
- Shifting field phase by 2π and taking the second image.
- Subtracting two images from each other.
- Storing the results as a 16 bit PNG file.

By such imaging manner, topographical contrast, as well as domain and domain wall contrasts, is eliminated, and the pure dynamic magnetization response (i.e., wall motion or magnetization rotation) is captured. To increase the signal to noise ratio (SNR) at any given AC field phase, 128 images are taken and the images are then averaged out. To monitor the applied voltage and in turn control the excitation field amplitude and phase, the output of the coplanar waveguide is continuously read by using a high-bandwidth sampling oscilloscope. Fig. 3.7 displays the simplified algorithm of the TR-MOKE imaging.

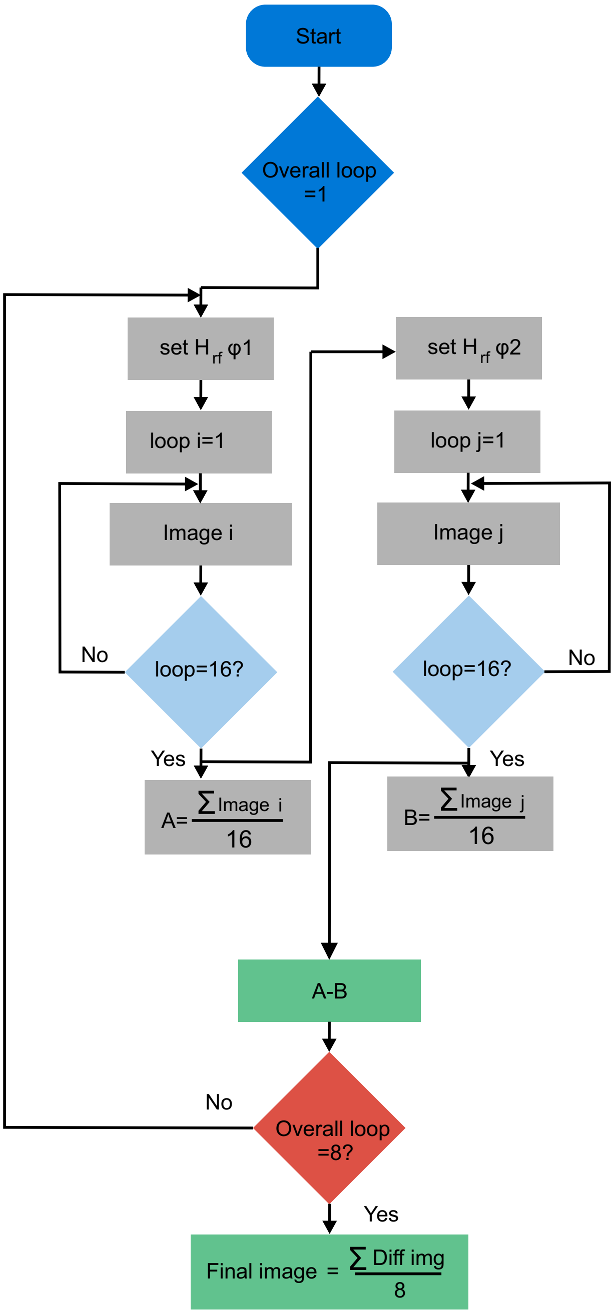

Figure 3.7: Simplified flowchart showing the high-level LabVIEW program that performs the TR-MOKE imaging.

The whole imaging process is computer-controlled by using two separated NI LabVIEW based interfaces; one for capturing, subtracting and averaging of images and the other one for controlling the timing, field frequency and amplitude of excitation field. As the laser has a fixed repetition rate of 50 MHz, only frequencies that are multiples of 50 MHz can be probed.

3.6 Pulsed Inductive Microwave Magnetometery

To measure the dynamic magnetic properties of the magnetic structured films, such as resonance frequency (f_{res}) and damping parameter (α), pulsed inductive microwave magnetometry (PIMM) [71, 72, 73, 74] was built in this project. Similar to the TR-MOKE, in the PIMM measurement the sample is placed upside down on the center of a coplanar waveguide. As shown in Fig. 3.8 the PIMM setup consists of a WaveExpert 100H sampling oscilloscope with a built-in Time Domain Reflectometry (TDR) unit, a pair of Helmholtz coils and a single layer rectangular coil for applying longitudinal and transversal DC magnetic fields, two power supplies, a coplanar waveguide for delivering the pulse field to the sample, and a computer LabView interface to control the measurement.

By changing the DC magnetic bias fields H_{bias}, the dynamic response of various magnetic domain configurations can be measured. Figure 3.9 displays the data collection and data post processing steps of the PIMM measurement. In a PIMM measurement, the magnetic sample will initially be saturated using a transverse DC magnetic field (along sample h.a.). Then a voltage pulse with a rise time of $t_{10/90}$=50 ps will be sent to the coplanar waveguide allowing for the measurement up to 20 GHz (f_{max}= $0.5/t_{risetime}$). The transmitted pulse from the coplanar waveguide is then measured and the DC saturation field is set to zero. The recorded signal is used as a reference (background) signal

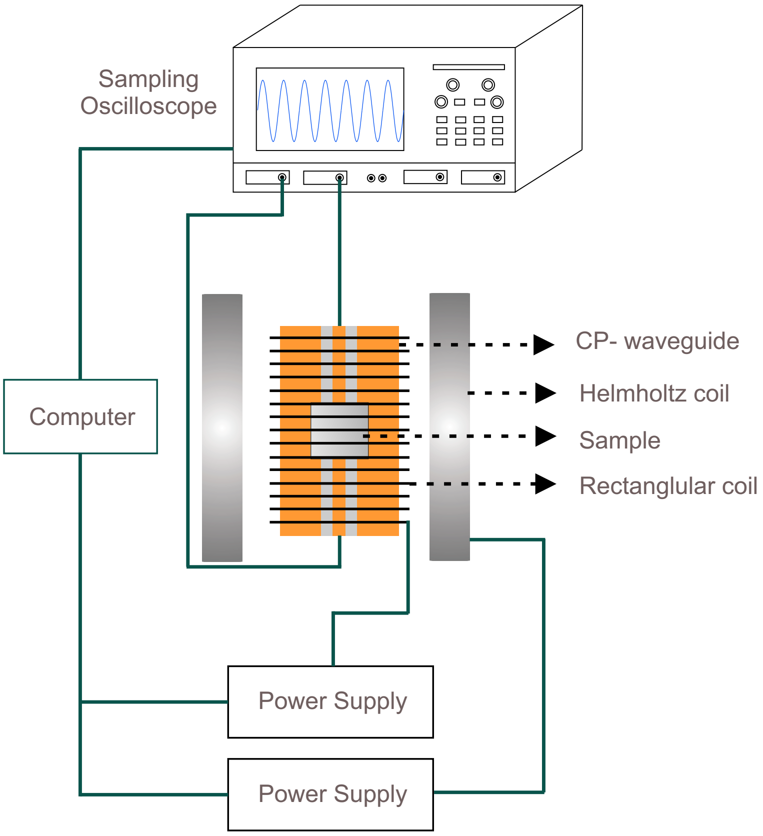

Figure 3.8: Schematic draw of pulsed inductive microwave magnetometer.

(Fig. 3.9 (a)). It should be noted that when the sample is in its saturation state, the applied pulse field does not have any impact on the sample. This is mainly because the pulse magnetic field and magnetic moments of the sample are aligned in the same direction, and therefore there is no applied torque on the film magnetization.

Once the background signal is measured and stored, the sample is initialized along its easy or hard anisotropy axis. Next, the DC bias field of interest is applied either in the e.a or h.a axis of the sample. Then the voltage pulse is sent through the coplanar waveguide. In this way, due to the existence of torque between the magnetic moments and applied excitation field, the magnetization state of the sample is changed, causing a change in the magnetic flux of the sample that, in turn, induces an inductive voltage into the coplanar waveguide. The induced signal is then be measured by the oscilloscope (Fig.

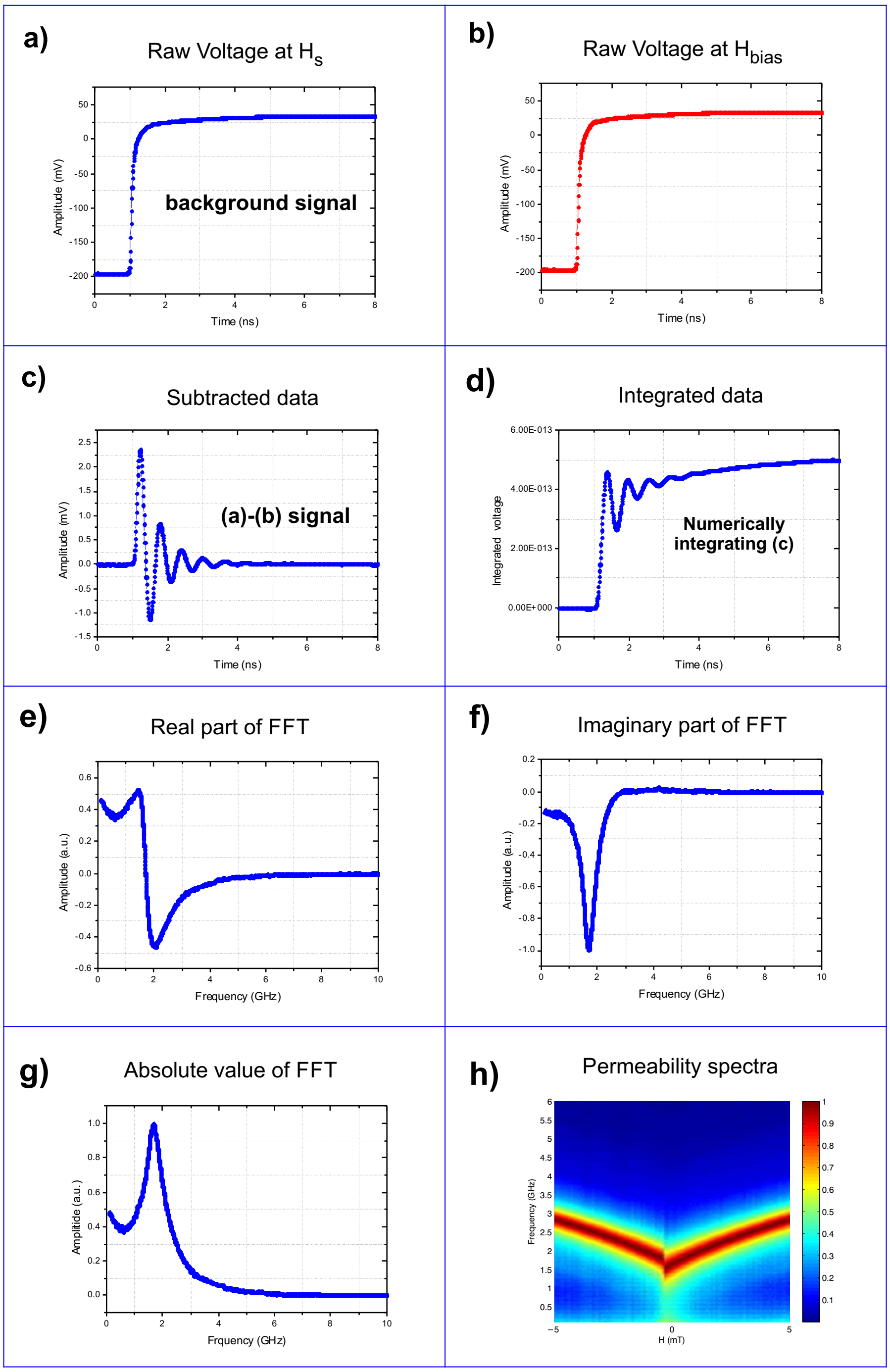

Figure 3.9: (a)-(b) exemplary raw data collected from PIMM measurement. (c)-(h) data post processing steps.

3.9 (b)). The inductive signal amplitude depends on the sample magnetization in the transversal direction through Faraday's law [75]. By subtracting the two recorded voltage signals, the temporal evolution of magnetization change is revealed (Fig. 3.9 (c)). Figure 3.9 (d) shows the numerically integrated signal of subtracted data. This shows the dynamic response of the magnetization of the sample. Applying Fast Fourier Transform (FFT) to the subtracted data, the imaginary (Fig. 3.9 (e)) and real part (Fig. 3.9 (f)) of the high frequency permeability, as well as absolute valuer of FFT (Fig. 3.9 (g)), can be calculated. By changing the DC bias fields and measuring inductive signal U(t) of multiple DC fields, a complete dynamic magnetic permeability spectrum of the sample is obtained (Fig. 3.9 (h)).

In this way, the dynamic response is investigated from the variation of the transmission amplitude of the microwave signal in a two-port configuration, basically measuring the amount of magnetic loss as a function of the rf excitation frequency. The resonance frequency corresponds to the frequency in which the absolute permeability peaks.

Unlike similar PIMM setups, in the presented PIMM measurement, the generation of voltage pulse and measurement of the induced signal is performed by the same unit (oscilloscope). This configuration results in a near jitter-free measurement. To calculate the damping parameter of the sample, an exponential function is fitted to the damped signal, from which the relaxation time is then calculated. The damping constant α, can be calculated using the following equation [76]:

$$\alpha = \frac{2}{\gamma \mu_0 M_s \tau} \tag{3.9}$$

Where τ is the relaxation time.

3.7 Inductive Measurements (B-H looper)

The basic magnetic properties of the magnetic samples are measured by an inductive magnetometer (a B-H looper) SHB Model 108 with a working frequency of 10 Hz. The B-H looper has a pair of Helmholtz coil with the ability to generate a maximum field of 20 mT. The pick up coil of the B-H looper enables it to measure the magnetic flux (B) at any given magnetic field (H). By this method the hysteresis loop of the magnetic sample, and in turn, the coercivity, quasi-static permeability and saturation field can be measured.

3.8 Micromagnetic Calculations

In order to create a proper design of experiments (DOE) and design the lithography reticle, the static domain configuration and dynamic response of different magnetic element shapes and sizes are simulated with MicroMagus micromagnetic numerical calculator [77]. Micromagus uses a finite-differential method (FDM) approach for numerical solution. Fig. 3.10 shows the exemplary results of such simulations. The shown simulated structure in Fig. 3.10 is a $Ni_{81}Fe_{19}$ film with a thickness of 30 nm.

The simulation is performed by simulating the initial domain configuration (Fig. 3.10 (a)). The dual-wavelength MOKE images [78] acquired later (Fig. 3.10 (b)) verified the simulation results. Next, a pulse-field was applied in different directions to estimate the dynamic responses from the element. Fig. 3.10 (c) displays the simulated response of the sample with a pulse of 100 ps rise-time compared to the result extracted from PIMM measurement shown in Fig. 3.10 (d). While the domain structure in the simulated data and MOKE images are similar, there is a clear difference in permeability and amplitude of the magnetization in the theoretical and experimental results. The magnetization changes in the experimental data over several nanoseconds can be attributed to the magnetization re-arrangement by domain wall processes. Another reason for the observed discrepancy is the size of the magnetic elements in the simulation, which is much smaller than the real magnetic sample.

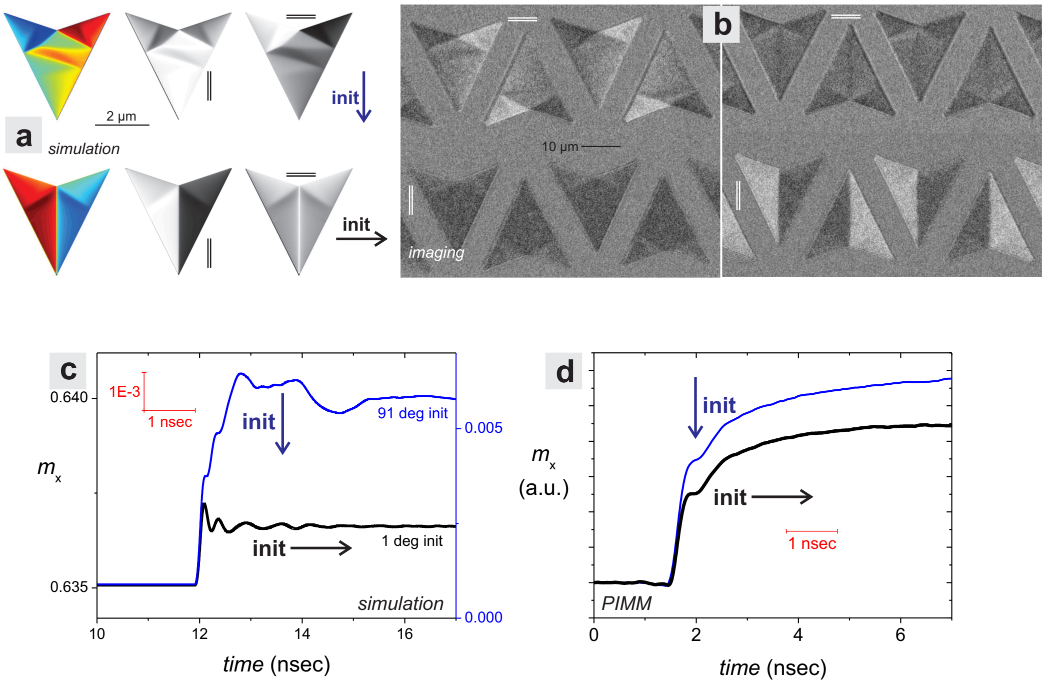

Figure 3.10: Simulation results compared to the experimental data. (a) simulated magnetic domain configuration at zero fields. (b) experimental MOKE images of the sample. (c) and (d) simulated and measured (by PIMM) magnetic dynamic responses of the magnetic element. The blue graph shows the magnetic dynamic response of the element when magnetically initialized along its easy axis; the black graph shows the response of the same element initialized along its hard axis

Chapter 4

Magnetization Dynamics in Large-Scale Elements

Reprinted article with permission from B. Mozooni, T. von Hofe, J. McCord, Picosecond wide-field magneto-optical imaging of magnetization dynamics of amorphous film elements, Phys. Rev. B 90, 054410, 2014, Copyright (2014) by the American Physical Society.
The article has been modified from its original version. Though the scientific results and interpretations are kept similar to the original article, the content has been edited to fit the format of this thesis.

4.1 Introduction

In this chapter, the application of the time-resolved Kerr microscopy method to study a non-LLG magnetodynamic behavior is demonstrated. Moreover, a solution to distinguish the in- and out-of-plane Kerr effect signals are shown. The chapter ends by proposing a more elaborate model of magnetization dynamics in large scale elements.

As explained in the previous chapter, the magnetization dynamics in magnetic films can be explained by the LLG equation (Eq. 2.12). Although, by formation of the magnetic domains and domain walls [79, 80, 81, 82, 83, 84, 85] the effective magnetic response is deviated from LLG equation. It is known that by the magnetic domains formation, the effective active magnetic volume is reduced, which leads to a reduction of high-frequency permeability. A detailed domain model of magnetization dynamics in soft magnetic films can be found in Ref. [82]. In short, the formulation of the domain model is done by assuming that the domain configuration is a nonlinear system of coupled and viscously damped oscillators with geometrically constrained motion. The model shows that different regions of thin-film (depending on the excitation field frequency) can contribute inconstantly in the magnetic dynamic response. In this case, due to the rotation or precession of magnetization in the center of patterned soft magnetic elements, the magneto-dynamic response might be ultimately damped by induced eddy current damping. Despite the mathematical explanation of magnetization dynamics by domain model, experimentally it is found that in addition to the contribution of the central area of the magnetic element to the magneto-dynamic response, the magnetization rotation in the regions confined by the closure domains also play a role in the high-frequency flux propagation [84].

The proposed models are mostly based on integral measurements in which instead of the localized magnetic behavior, the overall magnetic response of the entire sample area is taken into account.

To acquire a better picture of the magnetic dynamic response in large scale magnetic elements, the TR-MOKE is used. Unlike the integral measurements, TR-MOKE direct imaging can examine the magnetization dynamics of the magnetic films locally. Such a measurement is used to explain a more complex magnetic dynamic phenomena such as spin waves generation and propagation.

The sample investigated in this chapter was already introduced in Chapter 3, a patterned $(\mathrm{Fe}_{90}\mathrm{Co}_{10})_{78}\mathrm{B}_{10}\mathrm{Si}_{12}$ amorphous ferromagnetic thick film. Since the magnetic layer thickness is around 160 nm, it is in an asymmetric Bloch

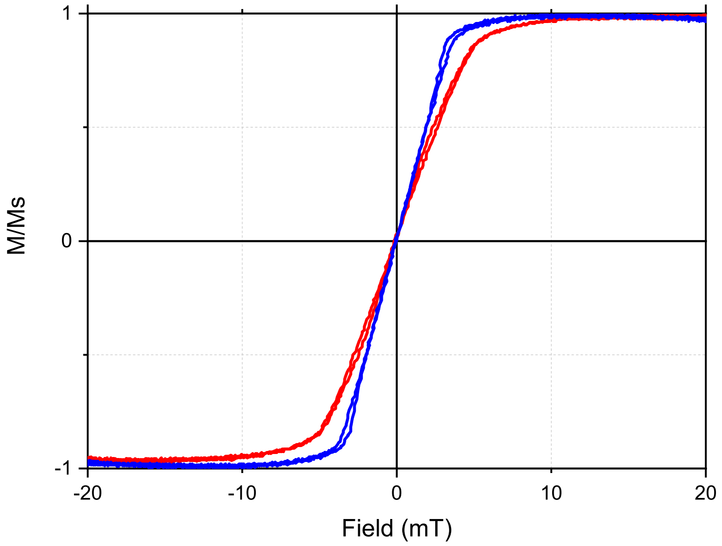

Figure 4.1: Magnetic element hysteresis loop along the easy (blue) and hard (red) anisotropy axises.

wall regime [86] (see Chapter 2).

4.2 Results and Discussion

The static magnetic properties of the sample are investigated by the B-H looper. Fig. 4.1 displays the magnetization hysteresis loop of the sample along the easy and hard anisotropy axis. The magnetic anisotropy field of the sample has been determined to be, $H_k = 1$ mT where $H_s = 5$ mT.

The dynamic magnetic properties of the sample are measured by PIMM. From PIMM data, a magnetic damping value of $\alpha = 0.008$ is determined. A more elaborate explanation of PIMM results is given later in this chapter.

The dynamic magnetic properties of the sample are measured by PIMM. From PIMM data, a magnetic damping value of $\alpha = 0.008$ is determined. A more elaborate explanation of PIMM results is given later in this chapter.

It should be noted that the sample magnetic state is excited with a

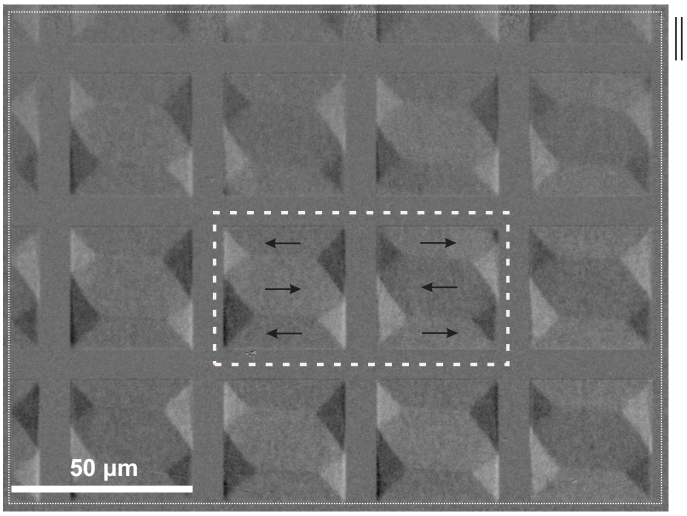

Figure 4.2: Static Kerr image shows an initial magnetic domain configuration with a Landau-like domain structure. The selected two neighboring magnetic elements are mirrored domain structures.

continuous AC magnetic field during the TR-MOKE imaging. The applied excitation field frequencies values at any given DC field are extracted from the PIMM results. In this case, the AC excitation field frequencies are mainly picked to be the resonance frequencies of the sample at different DC magnetic fields. To compare the magnetization dynamics at an excitation field equal to sample's resonance frequency with a non-resonance field frequency, the frequencies with the lowest permeability are also chosen. The temporal and laterally resolved images of the magnetization response allow for separation of the domain and domain wall high frequency induced effects [69].

Figure 4.2 displays the static MOKE image of the sample's initial magnetic domain configuration with a horizontal longitudinal sensitivity of the microscope. The image shows a Landau-like domain state. To obtain such domain state, the sample was first exposed to a DC saturation field H_s, and then demagnetized by a reversing and decreasing the AC magnetic field along the sample's easy anisotropy axis. Fig. 4.3 (a) and (b) show the selected neighboring mirrored elements from Fig. 4.2, and displays them together with dynamic TR-MOKE responses to a 3 GHz excitation AC magnetic field for polar and longitudinal microscope sensitivities in Fig. 4.3 (c, d) and Fig. 4.3 (e, f) respectively.

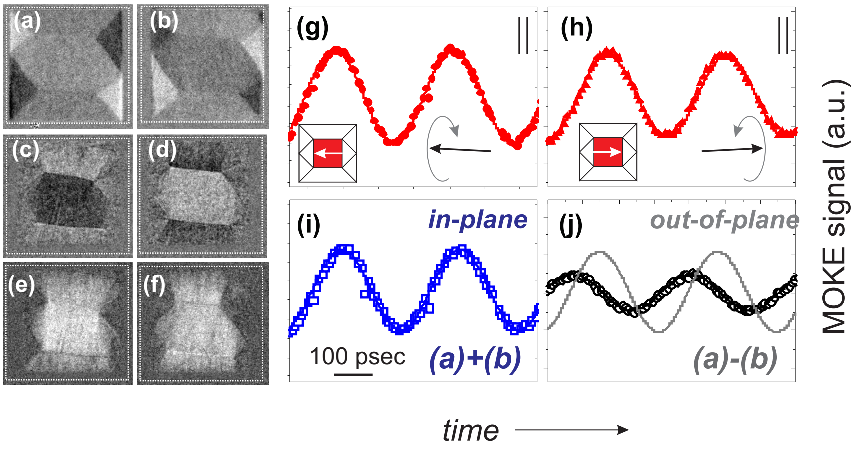

Figure 4.3: (a) and (b) display magneto-optical static domain images. (c) and (d) are corresponding TR-MOKE images of two adjacent mirrored domains (polar contrast). (e) and (f) are TR-MOKE images with microscope longitudinal sensitivity (contains both in- and out-of-plane signals). (g)-(j) display time evolution of magneto-optical signal amplitude using a 3 GHz excitation field. (g, h) Longitudinal contrast. (i) The averaged intensity of two domains contrasts ((i)/2+(j)/2, corresponds to a pure longitudinal signal). (j) The subtracted intensity of domains contrasts ((a)/2-(b)/2, pure polar component) (adapted from [69]).

As mentioned before, in order to show the maximum Kerr magneto-optical response, the dynamic domain images of two magnetic states from two AC excitation fields with a phase shift of $\pi/2$ are subtracted from each other. The Kerr contrast interpretation for polar sensitivity is straight forward. In contrast to that, the obtained images from longitudinal sensitivity configuration, contain both in-plane and out-of-plane dynamic magnetization information [69]. It should be noted that at lower frequencies the magneto-optical response contains pure in-plane magnetization contrast as no precessional out-of-plane motion takes place. Nevertheless, at high excitation field frequencies, this statement is not valid anymore, and the obtained Kerr signal is a combination of in- and out-of-plane magnetization response. To separate the in-plane and out-of-plane magneto-optical contrast from images acquired by microscope longitudinal sensitivity, the following solution proposed. The magneto-optical signals of two equivalent magnetic domains with a mirrored spin configuration are used. Considering the symmetry of responses, the pure in-plane MOKE response is calculated by summing up the MOKE signal extracted from the equivalent reversed domain structure. The out-of-plane contrast computes from the differentiating of these two responses [69].

The temporal progress of magneto-optical contrast corresponding to the dynamic magnetization response of the sample after being exposed to an excitation field frequency of 3 GHz, is shown in Fig. 4.3 (g)-(j). These figures display the acquired magneto-optical in-plane contrast of mirrored domains. It can be seen that the two domains have similar Kerr intensity amplitudes with a little phase shift. This is mainly due to the fact that the longitudinal microscope sensitivity encompasses both in- and out-of-plane contrasts. Figure. 4.3 (i) shows the added MOKE intensities from Fig. 4.3 (g) and (h) where Fig. 4.3 (j) displays the subtracted MOKE intensities. As previously mentioned, through the use of this method, the pure in-plane (Fig. 4.3 (i)) and out-of-plane (Fig. 4.3 (j)) response can be calculated. The in-plane and out-of-plane Kerr signals are clearly showing a phase shift of $\pi/2$, which is an indication of a dynamic magnetization precessional mechanism. This demonstrates the validity of the proposed solution.

Figure. 4.4 shows the static MOKE images of sample magnetization reversal along the easy axis. Figure 4.4 (a)-(i) indicate that the magnetization reversal starts with the magnetic domains nucleation at the edge of the magnetic elements (Fig. 4.4 (a), (b)). This is then continued by the formation of a 7-domain state. This is followed by domain walls movement over a DC field range from $H_{bias} = -3$ mT to $H_{bias} = 3$ mT (Fig. 4.4 (b)-(h)). At a DC field, around $H_{bias} = 4$ mT (Fig. 4.4 (h), (i)), the domain walls in the central part of the magnetic elements annihilate. For the easy axis reversal, no sign of hysteresis is observed, though, at high enough magnetic fields, indications of domain nucleation are found. As mentioned previously, magnetic domains formation affects the magnetization dynamics response of the magnetic element [69].

The measured permeability spectra along the sample's easy axis by PIMM

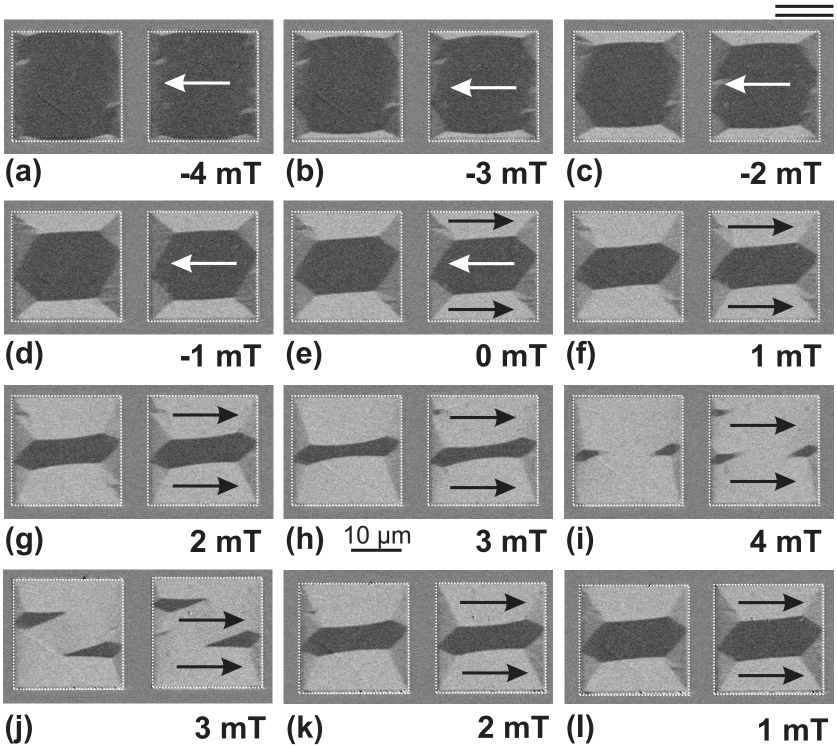

Figure 4.4: Static MOKE images of the magnetization reversal along the sample's easy axis [69].

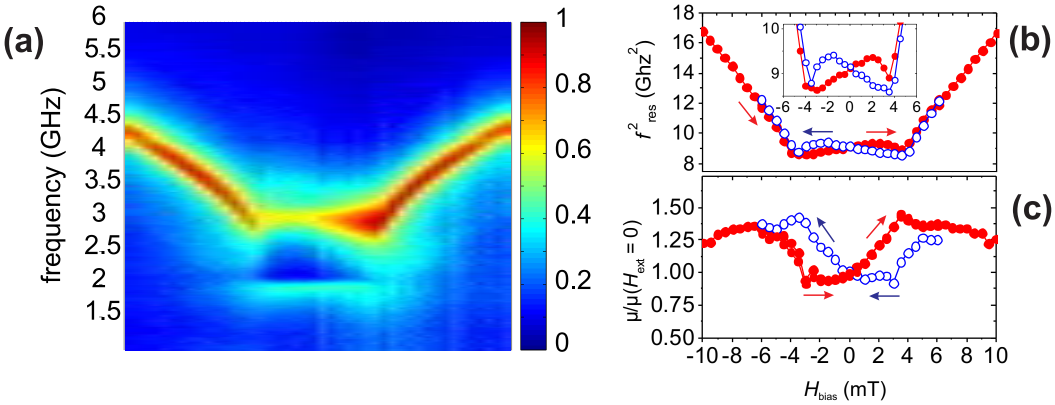

Figure 4.5: (a) Permeability spectra map of magnetic element measured by PIMM along sample easy axis. (b) Dominating precessional frequency square f_{res}^2, and (c) normalized peak permeability $|\mu|/|\mu|(0)$ for different H_{ext} (adpated from [69]).

is shown in Fig. 4.5 (a). Figure. 4.5 (b) displays the precessional frequency square f_{res}^2 versus H_{ext}. It can be seen that in high H_{ext} a Kittel behavior, $f_{res} \sim \pm H_{bias}^2$ [61], is observed. However, in the intermediate H_{ext} field range (-4 mT<H_{ext}<4 mT), the dominating precessional frequency $f_{res} \approx 3$ GHz remains nearly constant. This is due to the formation of a multi-domain state, which is shown in Fig. 4.4. Despite having a nearly constant value of resonance frequency in the intermediate H_{ext} field range, the permeability peak amplitude shows a strong dependency at H_{bias} and in turn the magnetic domains change. The maximum resonance frequency peak from PIMM is determined to be $f_{res} \approx 3$ GHz. This is well matched with experimental TR-MOKE results [69].

Figure. 4.6 shows the TR-MOKE images of magnetization dynamic response at different AC excitation magnetic field frequencies for AC field phase intervals of $\pi/2$. Depending on the field frequency, the corresponding time delay of a phase shift of $\pi/2$ varies from 5 nsec (at 50 MHz) to 76 psec (at 3.3 Ghz). At a low excitation AC field frequency (50 MHz), the magnetic response occurs through homogeneous rotation of magnetization in the domains with a magnetization alignment perpendicular to the excitation field, and mainly by 90° domain wall motion [69]. Besides, looking at Fig. 4.6 (a), an existing domain wall contrast at $\pi/2$ and $3\pi/2$ is observed, which is an indication of hysteretic nature of wall motion. The magnetic domain wall motion mechanism is the dominant magnetization dynamic response at lower frequencies (in this case, below 250 MHz). At a higher field frequency, the wall motion does not occur. This is due to the much slower nature of wall motion compared to the excitation field frequency [69].

By increasing the excitation field frequency, the dominant magnetization dynamic response is altered to the magnetization rotation mechanism in the central part of the magnetic element. This increases constantly and peaks around f_{res} (Fig. 4.6 (e), 0 and π). Such an observation is confirmed by the data obtained from PIMM. The strongest out-of-plane magneto-optical contribution

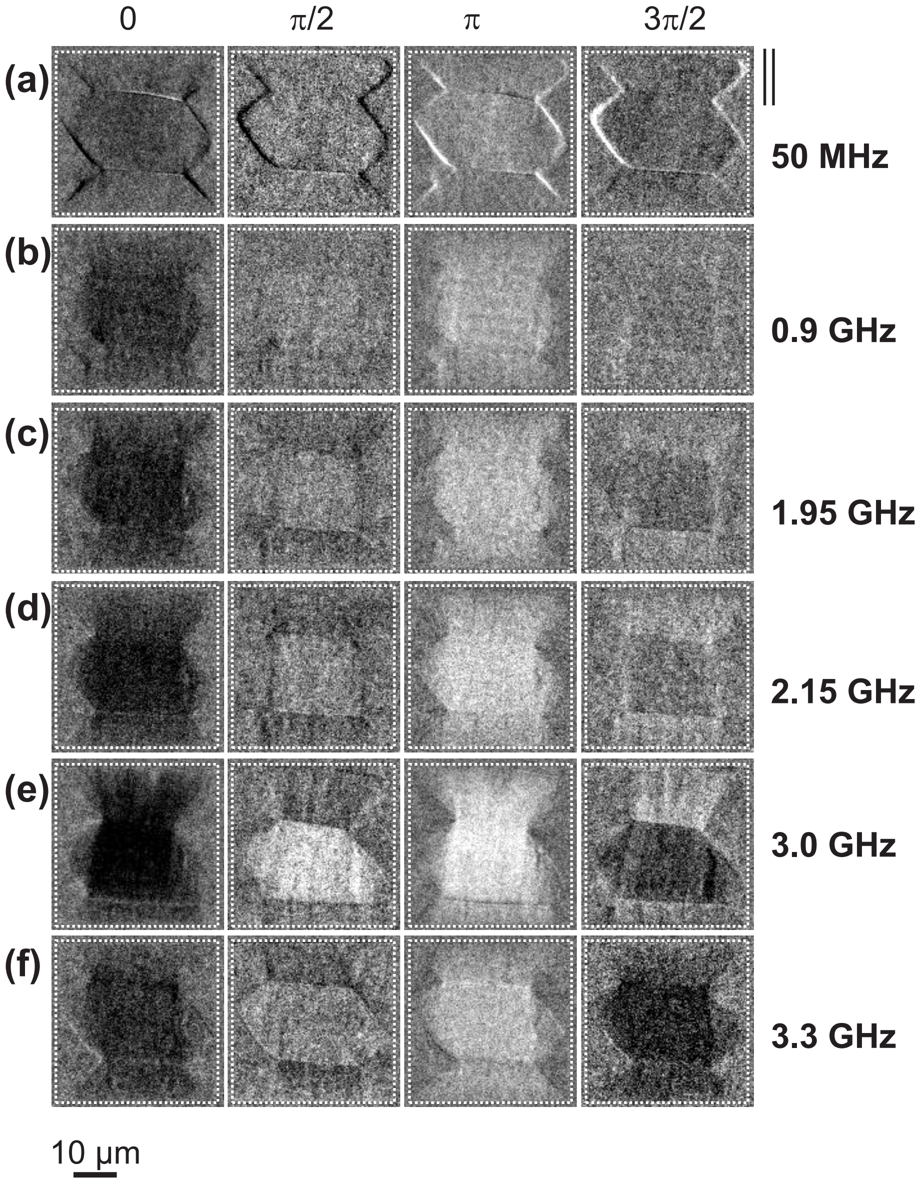

Figure 4.6: TR-MOKE images acquired by longitudinal microscope sensitivity for AC excitation field frequency of (a) 50 MHz, (b) 0.9 GHz, (c) 1.95 GHz, (d) 2.15 GHz, (e) 3.0 GHz, and (f) 3.3 GHz. As indicated above the figures, the images belong to every $\pi/2$ excitation field phases (adapted with minor modification from [69]).

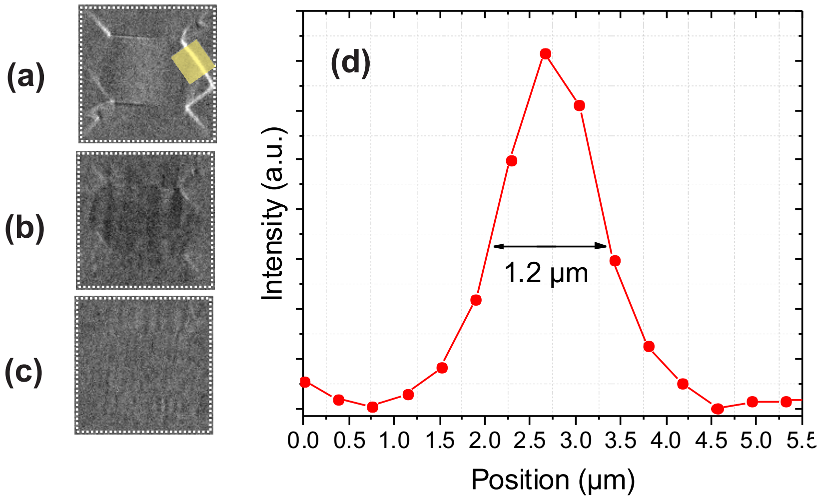

Figure 4.7: TR-MOKE images at (a) 50 MHz, (b) 150 MHz, and (c) 250 MHz. As indicated by the images, the wall motion is only visible at frequencies below 250 MHz. (d) Domain wall intensity analysis. A shown in (a), the intensity along the line perpendicular to the region of the domain wall movement vs. the position has been plotted, and by measuring the half-peak width, the average distance swept by the wall has been measured (adapted from [69]).

is visible at f_{res}, where a reverse Kerr contrast can be seen when comparing $\pi/2$ and $3\pi/2$ (Fig. 4.6 (e)).

In order to calculate the average domain wall speed, TR-MOKE images are used. The domain wall intensity along a perpendicular line to the domain wall movement direction (Fig. 4.7 (a) yellow box) versus the position has been plotted (see Fig. 4.7). The swept distance of the domain wall is calculated from the domain wall contrast at any given field frequency. Moreover, it is assumed that the swept area by domain wall is equal to half-peak width. Based on this assumption, the average distance swept by the wall has been calculated and then multiplied by the field frequency. For 50 MHz AC field, the domain wall speed is calculated to be $V_{\mathrm{DW}} \approx 60$ m/sec. However, at higher frequencies (e.g., 100 MHz), due to the low wall contrast (Fig. 4.6 (b, c)), the wall speed cannot be calculated [69].

Next, the longitudinal and polar MOKE signal separation method that

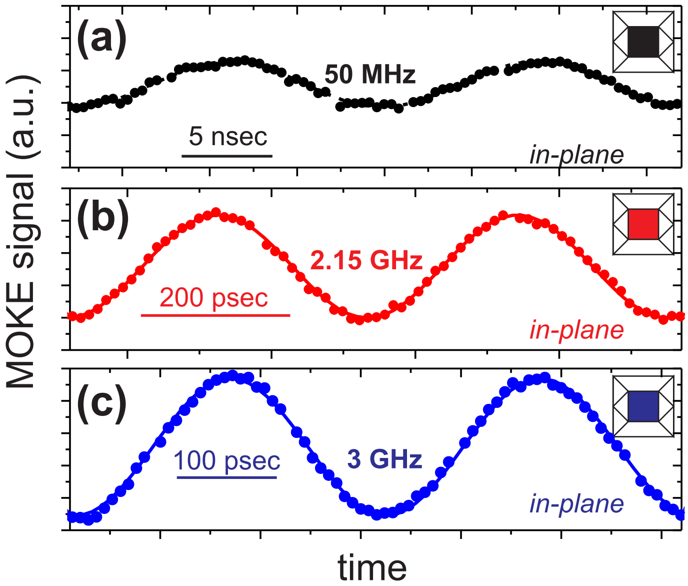

Figure 4.8: In-plane magnetization responses of central domain for excitation magnetic field frequencies of (a) 50 MHz, (b) 2.15 GHz, and (c) 3.0 GHz [69].

was previously explained is used. The pure out-of-plane and in-plane magnetization responses are distinguished. The results of such analysis for the in-plane magnetization responses in the central area of the magnetic element for AC excitation fields with frequencies of 50 MHz, 2.15 GHz, and 3 GHz are shown in Fig. 4.8 (a), (b) and (c) respectively [69].

To quantify the contribution of different domain regions in flux propagation, the in-plane and out-of plane magnetodynamic response of five separate domain regions is shown in Fig. 4.9. The out-of-plane component of TR-MOKE signals corresponds to the precessional movement. Therefore, in order to calculate the contribution of the magnetic precessional mechanism in the overall magnetization dynamic response, the out-of-plane component should be taken in to account. The average precessional motion at low frequencies ($f_{rf} = 0.9$ GHz) is identical for all domains, which have a magnetization perpendicular to the excitation field. By increasing the excitation magnetic field frequency, out-of-plane response (polar MOKE) increases and maxes out for all domains at $f_{rf} \approx 3$ GHz. The strongest out-of-plane precession is obtained from the central domain (Fig. 4.9 (a), red). At such high frequencies (close to $f_{resonance}$),

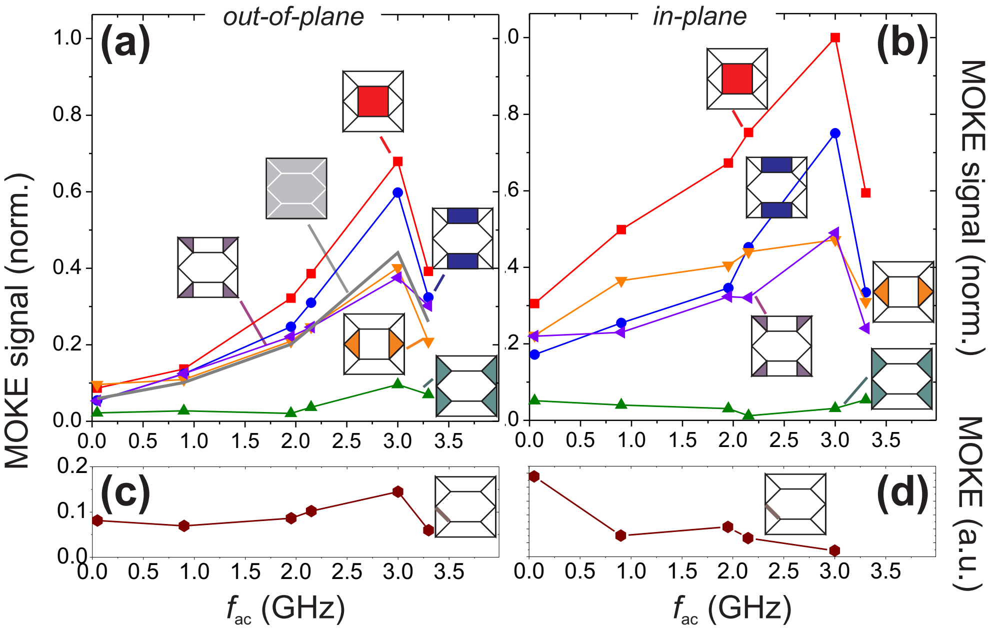

Figure 4.9: The local (a) out-of-plane and (b) in-plane magnetization response. The 90° domain wall contrast variation is displayed in (c) and (d) [69].

the closure domains magnetic spin, magneto-statically couples with the adjacent domains spins. Therefore, at a high enough magnetic field frequency in the closure domains (Fig. 4.9 (a), green), precessional motion occurs. As shown in Fig. 4.9 (b) green, no in-plane magnetization response occurs in the closure domains. As a result, it can be concluded that closure domains are not contributing to the magnetic flux propagation [69].

In addition, unlike other proposed magnetic flux propagation models, an in-plane magnetization dynamic response in the left and right corners of the central domain (central domain 'wings') is observed (Fig. 4.9 (b), orange). This indicates that the dynamic response in the central domains is not homogeneous. The flux response of the central region (Fig. 4.9 (b), red) and the surrounding edge domains (Fig. 4.9 (b), blue) as well as the wings (Fig. 4.9 (b), orange), increase in a similar way up to $f_{rf} \approx 1$ GHz. However, with further increases of f_{rf}, the response of the narrow 'wings' area increases slowly while the flux gets channeled into the central edge domain above and below the central domain.

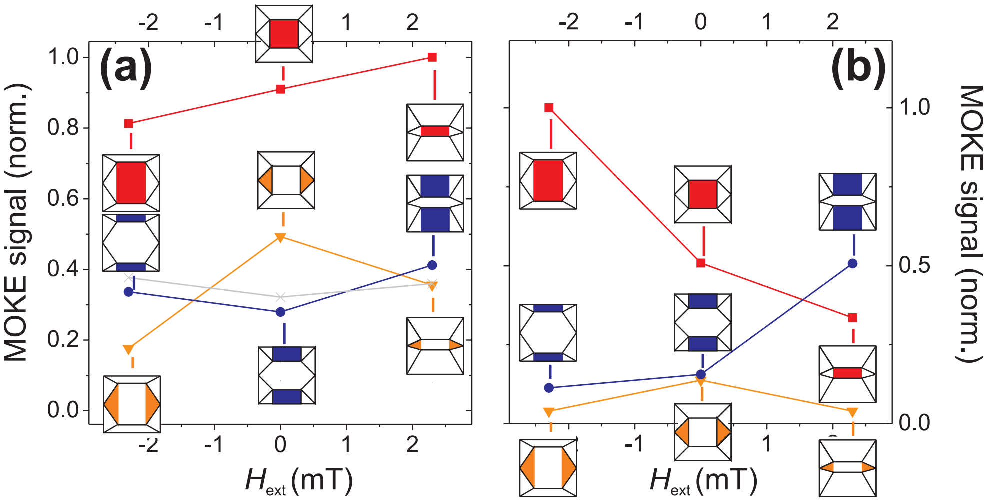

Figure 4.10: (a) Longitudinal MOKE signal for three different flux delivering regions in different bias DC fields. (b) Corresponding longitudinal MOKE contributions weighted by its surface area [69].

As shown in Fig. 4.9 (d), the magnetic domain wall in-plane magnetization response only occurs at lower frequencies, and it is reduced at frequencies above 50 MHz. This shows that at higher frequencies, domain wall motion does not occur. Interestingly, the TR-MOKE images show an out-of-plane precessional magnetization in the magnetic domain walls at resonance frequency $f_{res} = 3$ GHz (Fig. 4.9 (c)), which is a phenomenon that was not seen before. Indeed, this indicates a more complex magnetic response in such magnetic elements. By changing the excitation field frequency, the out-of-plane magnetization response is also changing.

Moreover, the dynamic magnetization response at a non-zero H_{ext} field has been investigated. The size of the magnetic domains has been changed, though the 7-domain state configuration is maintained. This is done by using a magnetic DC bias field along the easy axis of the magnetic sample. The corresponding domain shapes are presented in Fig. 4.4. The relative change of the magneto-optical signal at resonance for the central domain and the domains next to the edges for three different magnetic domain states corresponding to Fig. 4.4 (c), (e) and (g), are compared in Fig. 4.10. Figure. 4.10 (a) shows the local magnetic signal response, where Fig. 4.10 (b) displays the normalized Kerr signal by each regions surface size. As can be seen in Fig. 4.10 (a), the central domain response increases with decreases in domain width. This is in contrast with the expectation that the domain width or a dynamic demagnetization effect is the dominating factor determining changes of effective dynamic magnetic anisotropy [84, 87, 88]. This mismatch is due to the fact that the mentioned conclusions are derived from studying elongated stripe structures. However, for the square elements investigated here and for any smaller element, the local demagnetization field distribution and the occurrence of magneto-static Damon-Eschbach modes [89] have to be considered [69, 90, 91, 39].

The total magnetic response contribution is quantified by considering the size of individual regions in the calculation (Fig. 4.10 (b)). As can be seen, the main magneto-dynamic contributor changes from the central domain to the two neighboring edge domains with an increasing DC field. This is due to the changes in the individual domain size. Furthermore, the contribution of wing domains peaks at $H_{bias} = 0\ mT$ [69]. As discussed before, at zero magnetic bias field, the magneto-dynamic response of the magnetic element is not homogeneous. This observation is also examined for non-zero DC fields. The magnetization evolution at $f_{rf} = 3$ GHz across the magnetic element for higher DC fields is shown in Fig. 4.11 (a), the corresponding magnetic domain images of which are displayed in Fig. 4.11 (b) and (d) [69].

As seen, the maximum response perpendicular to the magnetization is in the center of the element. This response gradually decreases to the edge regions and is similar to the magneto-static Damon-Eschbach mode [69]. Moreover, as seen in Fig. 4.11 (c), magneto dynamic modes along the aligned magnetization take place. Also, an irregular response within the domain in other elements was found. A few examples are shown in Fig. 4.11 (e-f). Such modes are showing a similar characteristic to the ripple-like magnetic domain structure where a strong interaction with sample edges and domain walls are visible [69]. In addition to that, the occurrence of these modes seems to be related to the happening of microwave-induced switching of the magnetic domain structures

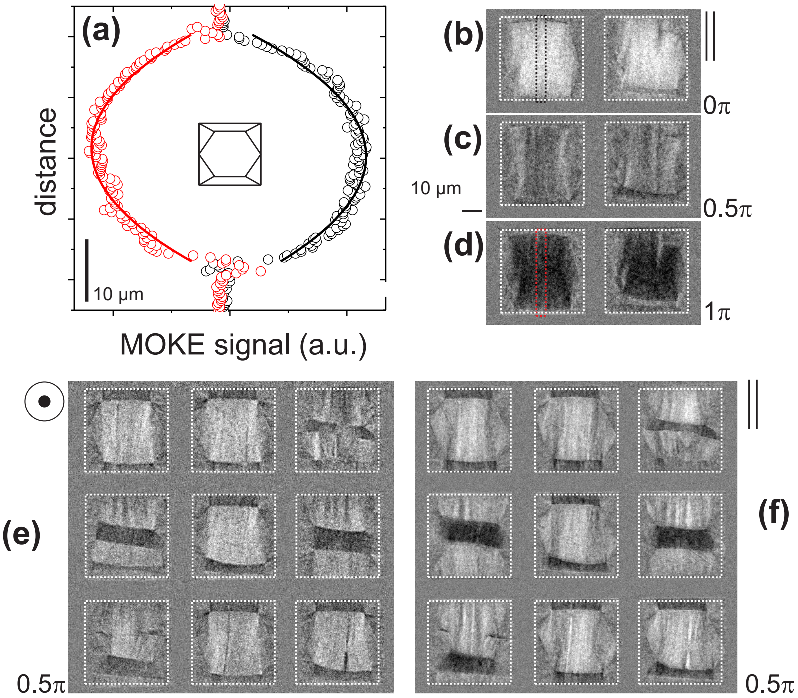

Figure 4.11: (a) TR-MOKE signal evolution throughout the magnetic elements for maximum and minimum magnetic field excitation. TR-MOKE images for (b) maximum, (c) intermediate, and (d) minimum MOKE signal. TR-MOKE images of same domain configurations acquired from (e) polar and (f) longitudinal microscope sensitivity [69].

[92].

4.3 Conclusion

The results of this work indicate that the magnetization dynamics processes in large-scale soft magnetic elements are much more complicated than the predicted response from domain models. Based on experimental data of integral measurements, a model of fast magnetization processes in patterned films was proposed by Mallary et al. in 1988 [93]. In that model, a pure magnetization rotation flux transfer is shown. In this case, it was suggested that the high-frequency response takes place through flux propagation limited to the center of the magnetic element, where the effective permeability in the closure domain regions at the edges of the element is insignificant (Fig. 4.12 (a)). A more elaborate model was proposed by Smith [82]. Similar to the results of this work, Smith's model predicted decreases in the domain wall motion above 10 MHz. In Smith's model, it was shown that a transformation from domain-wall-dominated magnetization reversal to the rotation-dominated around $f_{rf} = 100$ MHz takes place. The roll-off of domain wall motion is in agreement with the results of this thesis [69].

A more advanced model was proposed in Ref. [80]. It suggested that the flux propagation occurs due to the magnetization rotation in both center of the element and the closure domains (Fig. 4.12 (b). This is in agreement with the observations reported in this project. Unlike the TR-MOKE results, no response of magnetization in the closure domains was predicted.

In both mentioned models, the anisotropy field H_k determines the permeability in the central part of the element. This is in contrast with the observation reported in Ref. [84], where it shows the resonance modes depend on the domain-wall density as well. This is due to the narrow region of reduced permeability forming at the 180° domain walls, as seen in Fig. 4.12 (c) [69].

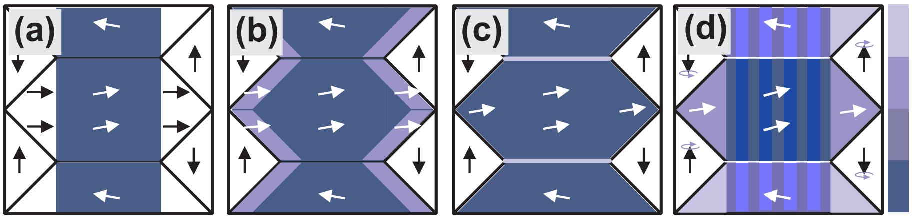

Figure 4.12: Summary of a few models for flux propagation mechanisms at high frequencies according to (a) Mallary [79] and Smith [82], (b) Ohashi [80], (c) Queitsch et al. [84], and (d) from the results of this thesis.[69].

So far, the suggested models are able to describe a few aspects of the occurring magneto dynamic effects. However, our TR-MOKE study reveals more complicated aspects of magnetization dynamic reversal in such magnetic elements. A new model based on the experiment here is shown in Fig. 4.12 (d). In this model (unlike other models), the closure domains also play a role in the magnetization dynamic response. This is shown to be due to magnetostatic coupling because of magnetization precession. The high-frequency permeability in the central top and down domains is reduced relative to the central domain. At the resonance frequency, inhomogeneous dynamic modes occur inside the domains. The main difference of this model compared to the other ones is that it considers the precessional out-of-plane magnetization contributions, which were not included in the early models [69].

Chapter 5

Domain Wall Induced Spin-Waves

Reprinted from "Direct observation of closure domain wall mediated spin waves", B. Mozooni et al.; Appl. Phys. Lett. 107, 042402, 2015, with the permission of AIP Publishing.

The article has been modified from its original version. Though the scientific results and interpretations are kept similar to the original article, the content has been edited to fit the format of this thesis.

5.1 Introduction

In this chapter, the time-resolved Kerr microscopy technique is used to study domain wall generated spin waves that have never been observed directly with an optical microscope. Mullenix et al. [94] show the domain wall induces spin waves in amorphous metallic films with in-plane anisotropy. These spin waves are playing a significant role in high frequency dynamic magnetic response of large scale patterned magnetic films [94]. Direct imaging of spin-wave modes with a time-resolved Kerr microscope can be used to determine the source of spin waves generation as well as their propagation mechanisms. The spin-wave studies are based on excitation and propagation. Practically, various techniques for spin waves excitation exist, including current pulse, magnetic field pulse, or laser pulse-induced spin wave excitation [95].

In this chapter, a new method to generate and propagate the spin waves is shown. To generate spin-waves, a source and a deriving force to excite the spin waves are needed. In this work, pinned magnetic domain walls are used as a source for spin wave generation, and a homogeneous excitation magnetic field plays a deriving force for this process. The acquired TR-MOKE images display the generation of spin waves from oscillating 90° domain walls [65]. Moreover, the results of this work show the possibility of guiding spin waves along a natural magnetic path, which is constricted by the 180° Bloch domain walls that act as a spin wave-guide. Such natural channels are acting like spin-wave conductors. This shows that to channelize and guide the spin-waves, no structural patterning is needed. It is also shown that spin waves can propagate over several tens of micrometers [65].

It should be noted that similar studies, which are performed on similar square elements with a closure domain [96, 45, 84, 88, 97, 69], did not show any sign of spin-wave propagation.

5.2 Results and Discussion

The sample used in this chapter is a patterned $(\mathrm{Fe}_{90}\mathrm{Co}_{10})_{78}\mathrm{Si}_{12}\mathrm{B}_{10}$ film, which was already introduced in Chapter 3. To examine the dynamic magnetic properties of the sample, the magnetodynamic response of the magnetic element exposed to an AC excitation magnetic field with frequencies from 50 MHz up to GHz range is imaged by TR-MOKE.

In order to perform the dynamic imaging, an AC excitation field with a base to peak effective amplitude of $H_{hf,bp} = 0.64$ mT is used. The TR-MOKE imaging is done using both longitudinal and polar microscope sensitivities. In order to implement a physical path for the propagation of spin waves, the sample

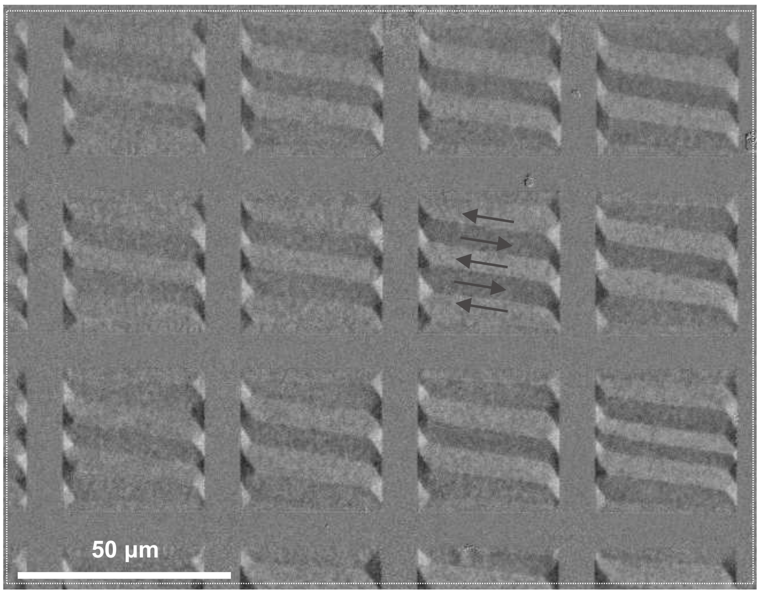

Figure 5.1: Static MOKE image showing a patterned magnetic film's domain configuration after demagnetizing along its hard anisotropy axis.

is initialized in a way that narrow magnetic domains with a width of approximately 7 μm are formed. This magnetic domain configuration is shown in Fig. 5.1. To create such a domain configuration, the sample is demagnetized by applying a cyclic decreasing AC magnetic field (starting from 10 mT) aligned to the sample's hard magnetic anisotropy axis [65].

Figure 5.2 shows the static MOKE image of the sample (Fig. 5.2 (a)) together with the magneto-optical time-resolved Kerr images obtained from AC magnetic field with various frequencies, which is applied along the sample's hard anisotropy axis. All images are obtained from longitudinal magneto-optical sensitivity of the microscope. The magnetization dynamic response to a low frequency 1 Hz field is shown in Fig. 5.2 (b). This indicates a clear movement of closure domain walls. The domain wall motion occurs in synchronization with the frequency of the applied magnetic excitation field. The TR-MOKE images acquired from magnetic field frequencies of f_{hf} = 50 MHz, 100 MHz, 150 MHz, 200 MHz, 300 MHz, and 2 GHz are shown in Fig. 5.2 (c-h). As seen in Fig. 5.2 (c-f), for excitation field frequencies up to 200 MHz, closure domain oscillation takes place. However, by increasing the frequency to f_{hf} = 300 MHz

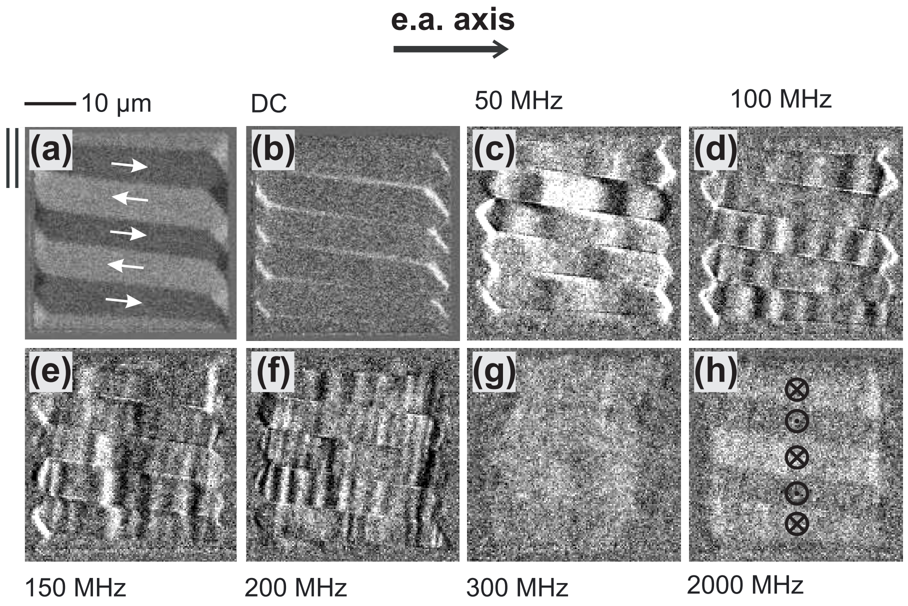

Figure 5.2: (a) Initial magnetic domain configuration after demagnetizing the sample along its hard anisotropy axis. (b)-(h) dynamic response of magnetic element to AC field frequencies of (b) 1 Hz (c) 50 MHz, (d) 100 MHz, (e) 150 MHz, (f) 200 MHz, (g) 300 MHz, and (h) 2 GHz [65].

and above, no sign of domain wall movement can be seen (Fig. 5.2 (g, h)). This is due to the fact that at lower frequencies domain walls motion is quick enough to respond to the induced torque of excitation field, though at higher field frequencies domain, the walls motion lags behind the AC field [98]. It should be noted that similar to the previous chapter, the images are the results of subtracting two images from 2π phase-shift. This is done to obtain the highest magnetic domain wall contrast.

The TR-MOKE dynamic magnetization images are in agreement with Ref. [81, 98]. In these two works, a decrease of inductive response at frequencies around 100 MHz is reported and explained to be due to a roll-off of domain walls motion. By increasing the field frequency, the magnetodynamic response is changed to the precession of magnetization in the domain (Fig. 5.2 (h)). The magnetization precessional motion is visible in the images obtained by the polar magneto-optical contrast ($\odot$ and $\otimes$, Fig. 5.2 (h)). Furthermore, as demonstrated at field frequencies of 300 MHz and above, the closure domain region is not contributing to the magnetic flux propagation anymore [65].

Looking to Fig. 5.2 (c-f), it can be seen that with the domain wall excitations, spin waves are initiated in the vicinity of 90° closure domain walls. This is due to the existence of an inhomogeneous demagnetizing field close to the domain walls. Such demagnetizing field acts as an effective potential well for the spin waves generation [65, 99, 100]. Additionally, the out-of-plane magnetization components of precessing domain walls can also lead to the generation of spin waves [65]. The direction of spin-waves propagation is determined to be along the magnetization direction of the domains. Looking at Fig. 5.2, one can see the inhomogeneous nature of spin waves magnetodynamic response.

In addition, in this chapter, it is shown that not only can the spin waves generation be performed in a controlled manner, but also the spin-wave wavelength and density can be tuned by changing the frequency of the excitation magnetic field. It has been determined that by increasing the AC field frequency, the wavelength of the spin waves decreases while the number of generated spin waves are linearly increasing [65].

Figure. 5.3 (a) shows the spin-wave behavior in different magnetic elements on thin-film at an excitation field frequency of 100 MHz. This indicates the dependency of spin-wave generation with domain wall characteristics. As can be seen in multiple domains, when the closure domains are not oscillating, no spin-wave is generated. This provides additional evidence that verifies the 90° domain wall oscillations are the source of spin-wave generation [65]. Instead, as soon as a pronounced movement of two closure domain walls takes place, the spin waves generation phenomena appear.

Figure 5.3 (b) displays the changes of magnetization in field phases of 0π, 0.5π, 1π and 1.5π. Looking at images obtained with a field phase of 0.5π and 1.5π, an out-of-phase response of domain wall relative to magnetization response in the center of the domain is visible. This shows that oscillating domain wall motion has a phase lag of magnetization response [65, 101, 102]. Similarly, by examining the polar MOKE contrast, an out-of-plane magnetization response

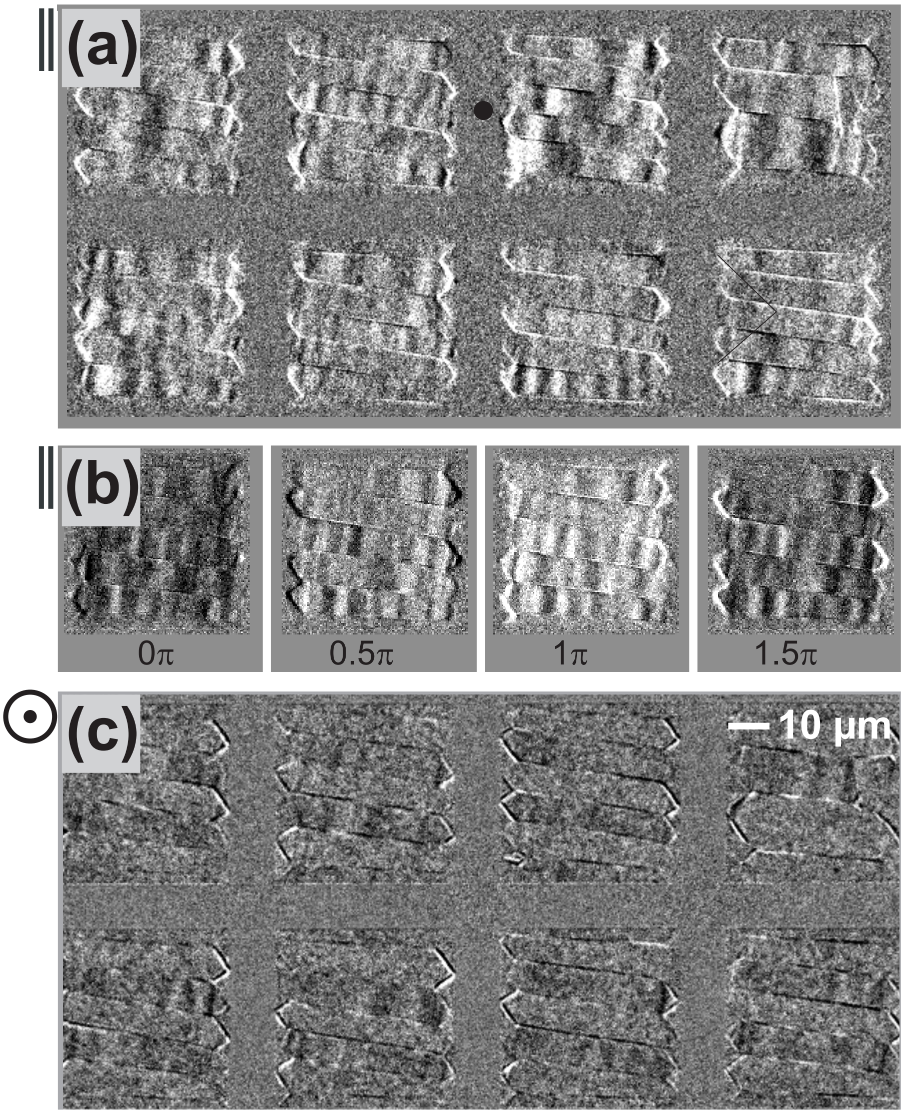

Figure 5.3: Acquired differential TR-MOKE images of the magnetic element using an AC magnetic field with a frequency of 100 MHz. (a) spin-wave behavior in multiple magnetic elements and (b) in different field phases. (c) TR-MOKE images obtained from polar magneto-optical sensitivity (adapted with minor modification form [65]).

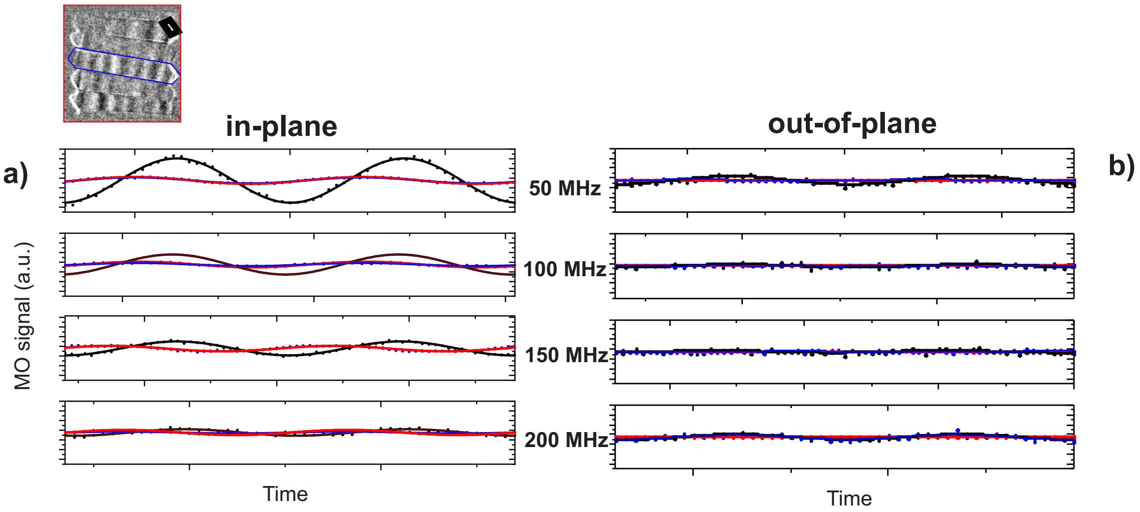

Figure 5.4: Evolution of magneto-optical contrast by time for (a) in-plane and (b) out-of-plane microscope sensitivity for 50 MHz, 100 MHz, 150 MHz and 200 MHz rf field frequency (from top to bottom respectively). The region of interest is shown on above the plot.

in the domain walls are visible (Fig. 5.3 (c)). This is due to the precessional magnetization motion in domain wall [101]. Such precessional motion in the magnetic domain walls is also reported for transverse-type domain walls in magnetic nano-wires [103] and for 90° walls [102]. Looking at Fig. 5.3 (a) and Fig. 5.3 (c), it can be concluded that without out-of-plane magnetization excitation in the domain walls, no spin waves will be generated [65].

Figure 5.4 displays the evolution of magneto-optical contrast by time for the in-plane and out-of-plane microscope sensitivity with AC field frequencies of 50 MHz to 200 MHz for an exemplary magnetic element. The regions where the intensity is extracted are color-coded, black for the domain wall, blue for the center of the domain, and red for the whole magnetic element response. As seen from the in-plane amplitude, at a lower frequency (50 MHz), the highest amplitude of magneto-optical signals belongs to the domain wall, which is a sign of dominant wall oscillation at lower frequencies. By increasing the frequency, wall motion reduces. However, the domain response stays constant from 50 MHz to 200 MHz. Moreover, there exists almost a 90° phase shift between wall excitation and domain response of rf-field excitation.

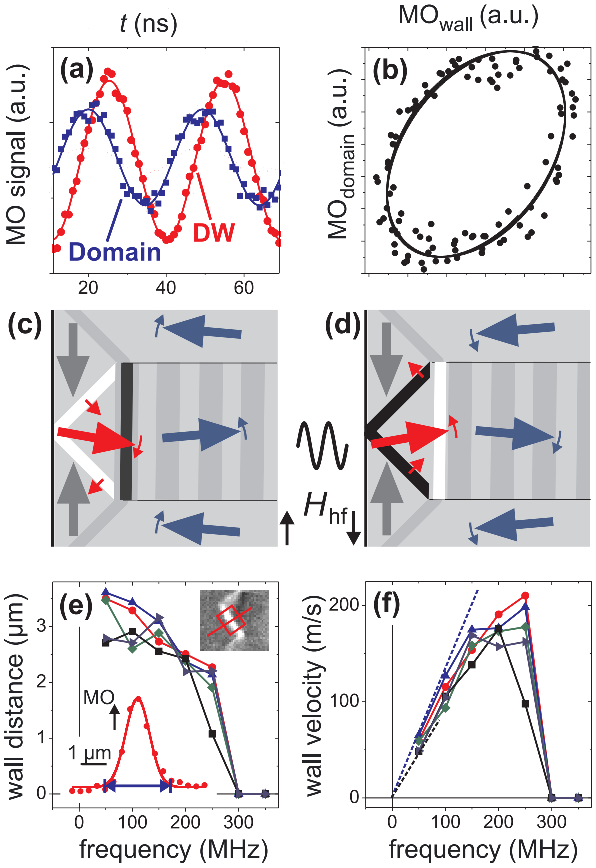

Figure 5.5: (a) Selected magneto-optical evolution within the magnetic element and domain wall response and (b) Kerr signal over domain wall response at 100 MHz. (c) sketch of magnetization response with upward (c) and downward (d) excitation field. (e) The swapped distance of domain walls at different field frequencies. (f) domain wall velocities with excitation frequency [65].

The domain wall characteristics and velocity are analyzed by investigating the magneto-optical Kerr signal (Fig. 5.5). The extracted MOKE intensity analysis shows the domain wall motion is out-of-phase with the AC excitation field. This can be seen in Fig. 5.5 (a) and (b) for a frequency of $f_{\text{hf}} = 100$ MHz . Figure 5.5 (c) and (d) show the out-of-phase magnetization response of the closure domains and the central domain region for upward and downward magnetic field excitation field H_{hf}, respectively. The magnetization response in the closure domain region is reversed compared to the central region [65]. Using the same method shown in Chapter 4, the domain wall velocity is calculated. Figure 5.5 (e) shows the distance swapped by the domain walls at a given

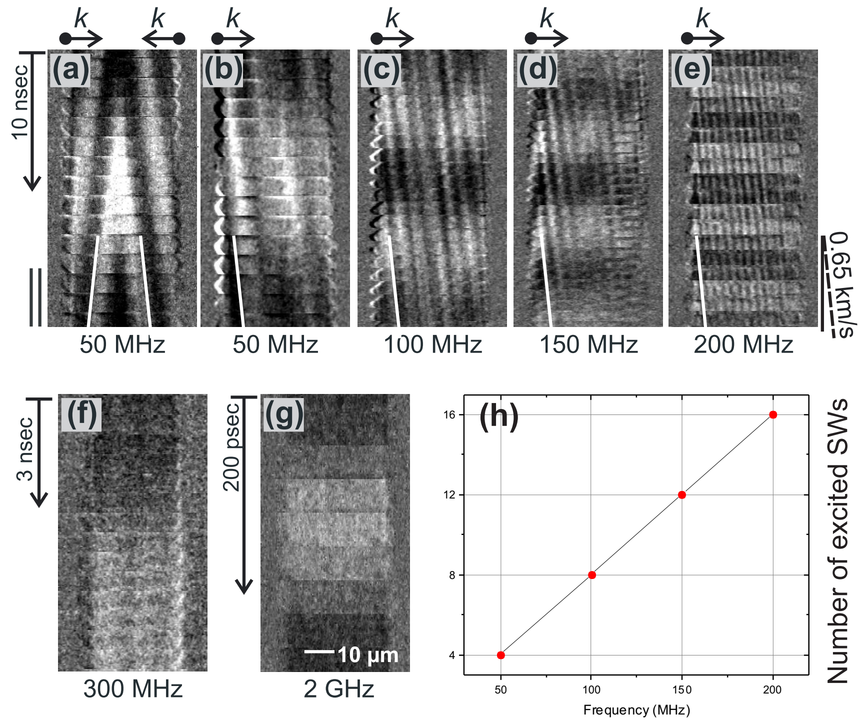

Figure 5.6: TR-MOKE response of one narrow domain with time field frequencies of (a), (b) 50 MHz, (c) 100 MHz, (d) 150 MHz, (e) 200 MHz, (f) 300 MHz, and (g) 2 GHz. A line representing a spin wave velocity of $v_{SW} = 0.65$ km/s is shown in (a-e). (k shows the direction of spin wave propagation). (h) number of excited spin waves at given field frequencies ((a-g) from Ref. [65]).

frequency. To increase the accuracy of calculation, the analysis is done on 5 different magnetic elements. As seen, domain wall movement reduces with increasing frequency and drops to zero at frequencies above $f_{\text{hf}} = 250$ MHz. The results of the domain wall velocity in different excitation frequencies are shown in Fig. 5.5 (f). Through this method, a maximum domain wall velocity of around $V_{DW} = 200$ m/s is calculated. At $f_{\text{hf}} = 300$ MHz and above no noticeable domain wall motion occurs [65].

Figure 5.6 shows the time evolution of spin waves movement in an individual domain for different field frequencies. The images obtained from dynamic Kerr microscope and magnetization response extracted from an individual magnetic domain versus time, from top to bottom, are shown [65]. As seen in Fig. 5.6 (a), spin-waves are generating from domain wall oscillations from both edges of the elements. As shown, in this uncommon case, the spin waves travel from 90°

walls to both sides and annihilate. As mentioned before, the spin waves within a magnetic domain, which are generated from one side of the element, penetrate through the whole element in the spin-wave path formed by the 180° domain walls. The frequency dependence of spin-wave characteristics is displayed in Fig. 5.6 (b-f). At a very high field frequency of 2 GHz, no domain wall oscillation is seen, and in turn, there are no spin wave generation phenomena (Fig. 5.6 (g)). The magneto-optical analysis shows a linear relationship between the excitation magnetic field frequency and the number of activated spin waves within the domains (Fig. 5.6 (h)). For the selected example, it varies from 4 excitations per domain for 50 MHz field frequency to 16 excitations per domain for a frequency of 200 MHz. The excitation frequency acts as a linear regulator of spin-wave frequency. The spin-wave wavelength can be directly tailored [65].

From spin-wave velocity calculation, it was determined that the velocity of spin propagation is constant. Further, it was seen that the spin-waves velocity is independent of the excitation field frequency. The spin-wave velocity is determined to be approximately $V_{SW} = 0.65$ km/s [65].

Chapter 6

Spin-Waves Generation in Magnetic Landau Structure

The content of this chapter is published in *"Homogeneous microwave field emitted propagating spin waves: Direct imaging and modeling", M. Lohman, **B. Mozooni**, J. McCord; Journal of Magnetism and Magnetic Materials, 2018.* The article has been modified from its original version. Though the scientific results and interpretations are kept similar to the original article, the content has been edited to fit the format of this thesis.

6.1 Introduction

As mentioned in Chapter 5, the high propagation velocity of spin waves makes them an appealing topic of many research projects. There are a variety of methods to generate spin waves such as using local antennas [104], confined excitation of magnetization [105] or as shown in Chapter 5 using pinned magnetic domain walls. In this chapter, an alternative method of spin-wave generation is shown. It is demonstrated that in the presence of high-frequency magnetic excitation fields, the edges of a magnetic element with a magnetic Landau structure can act as a source to generate spin waves. The introduced method in this chapter is an easy way to generate, guide, and focus spin waves in a controlled

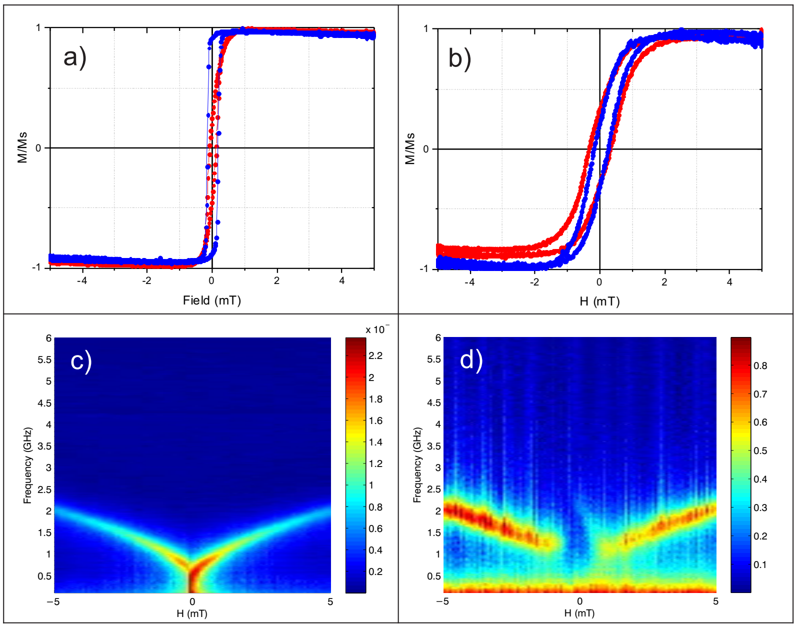

Figure 6.1: Magnetic properties of the sample used in this chapter. (a)-(b) magnetic hysteresis loops along sample easy (blue) and hard (red) anisotropy axis for unstructured and structured film, respectively. (c)-(d) permeability spectra of unstructured and structured film correspondingly.

manner. Unlike the previous chapter, this is done in large magnetic structures rather than micromagnetic structures such as domain walls. TR-MOKE is used to image the spin-wave generation and propagation in such structures.

6.2 Results and Discussion

Figure 6.1 shows the basic dynamic magnetization properties as well as dynamic magnetic permeability spectra of the unstructured film and compares it to the patterned film, which is used for TR-MOKE imaging. Comparing the magnetic hysteresis loop of the unstructured film (Fig. 6.1 (a)) to the structured one (Fig. 6.1 (b)) by increases of magnetic saturation field of sample from H_s = 0.5 mT to H_s = 3 mT is seen. Also, PIMM results show that by patterning the film, the permeability peak is split (Fig. 6.1 (d)), which is not the case in the unstructured film (Fig 6.1 (d)). From PIMM results, the patterned structure resonance frequency is calculated to be 1.3 GHz when it is magnetically in the Landau domain state. Next, the dynamic magnetic response of the patterned film is investigated using the TR-MOKE and applying an AC magnetic field with a base-to-peak amplitude of 0.38 mT and field frequencies from 50 MHz up to 4 GHz. The excitation field is applied along the square elements' diagonal. This is to ensure the same magnetic torque is acting on all the magnetic domains of the Landau state. The TR-MOKE images are acquired from the longitudinal sensitivity of the microscope that contains both in-plane and out-of-plane dynamic responses of the sample [106].

Prior to the imaging, the sample is initialized in a way that a magnetic 4-domain state (Fig. 6.2 (a)) is formed. In this magnetic configuration, the magnetic stray field distribution along the magnetic element width is zero. The AC excitation magnetic field H_f is applied diagonally to the sample. Figure 6.2 (b)-(h) show the magnetization dynamic response for pairs of the magnetic element to an AC magnetic field with frequencies of 0.05 GHz to 4 GHz. As mentioned before, since the oblique plane of incidence is used, the dynamic images contain both in-plane and out-of-plane magnetization responses [106].

Looking at Fig. 6.2, three different types of dynamic responses are determined. At a low excitation field frequency of 0.05 GHz (Fig. 6.2 (b)), magnetization reversal takes place mainly by domain wall motion. By increasing the excitation field frequency to the resonance frequency, the reversal mechanism changes to the magnetization precessional response (Fig. 6.2 (c)-(e)). This is the dominant mechanism for AC field frequencies of 1 GHz to 2.5 GHz. Nevertheless, the alternating background domain contrast shows up to 4 GHz (Fig. 6.2 (f)-(h)). At excitation field frequencies of 2.5 GHz and above (Fig. 6.2 (e)-(h)) a modulated magnetic behavior is observed. This is an indication of the generation of spin waves, which are restricted to the individual domains. The wavefront of spin waves is lined up parallel to the edges of the element. The spin waves especially can be distinguished at higher excitation field frequencies (Fig. 6.2 (g, h)) [106].

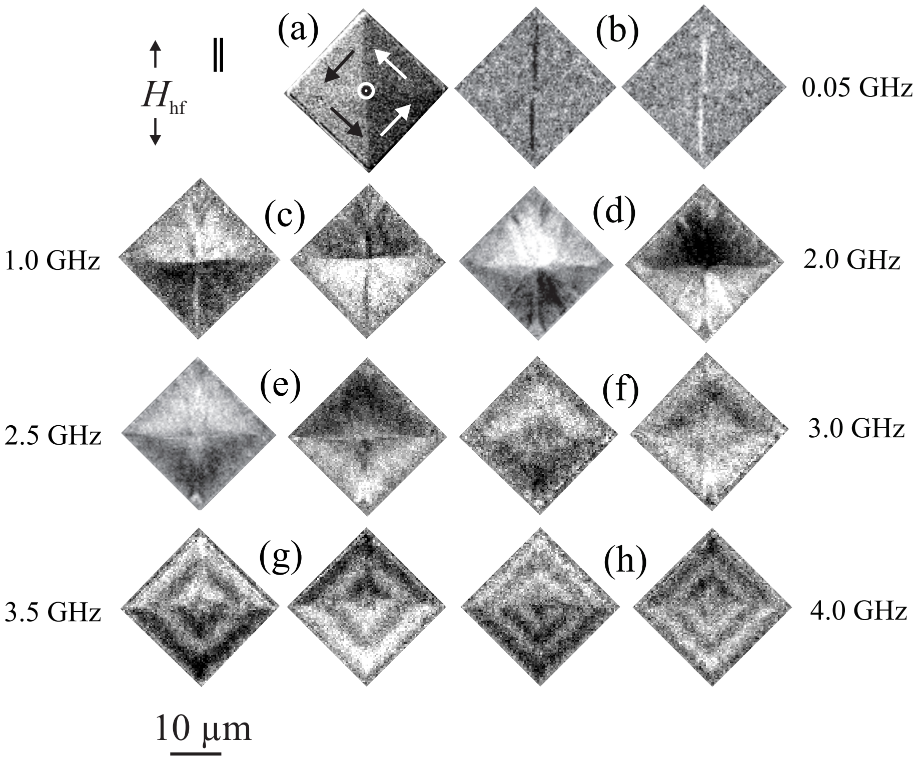

Figure 6.2: (a) Magnetic element with Landau domain configuration. (b)-(h) TR-MOKE images obtained from field frequencies of 50 MHz to 4.0 GHz (adapted from [106]).

Looking to the (Fig. 6.2 (f)-(h)), one can see the propagating nature of generated spin waves, especially for field frequencies of 3.5 GHz and 4.0 GHz. To see this propagating characteristic with greater details, the full excitation cycle (250 ps) of magnetic elements for an AC field frequency of 4 GHz is shown in Fig. 6.3. The visible characteristics of magnetization reversal that can be seen in Fig. 6.3 is the magnetization precessional response of the sample. The underlying contrast in the top and bottom domains cycles once per field period with a phase shift of $\pi/2$ relative to the dynamic field excitation (compare t_d = 60 ps to t_d = 190 ps) [106].

In order to calculate the spin-wave propagation velocity, the method introduced in Chapter 4 and Chapter 5 is used. Figure 6.4 displays the temporal evolution of cross-sectional MOKE contrast for an AC field frequency of 4 GHz. With this, the spin-wave propagation velocity at 4 GHz is calculated to be V_{sw} = 22.5 km/s.

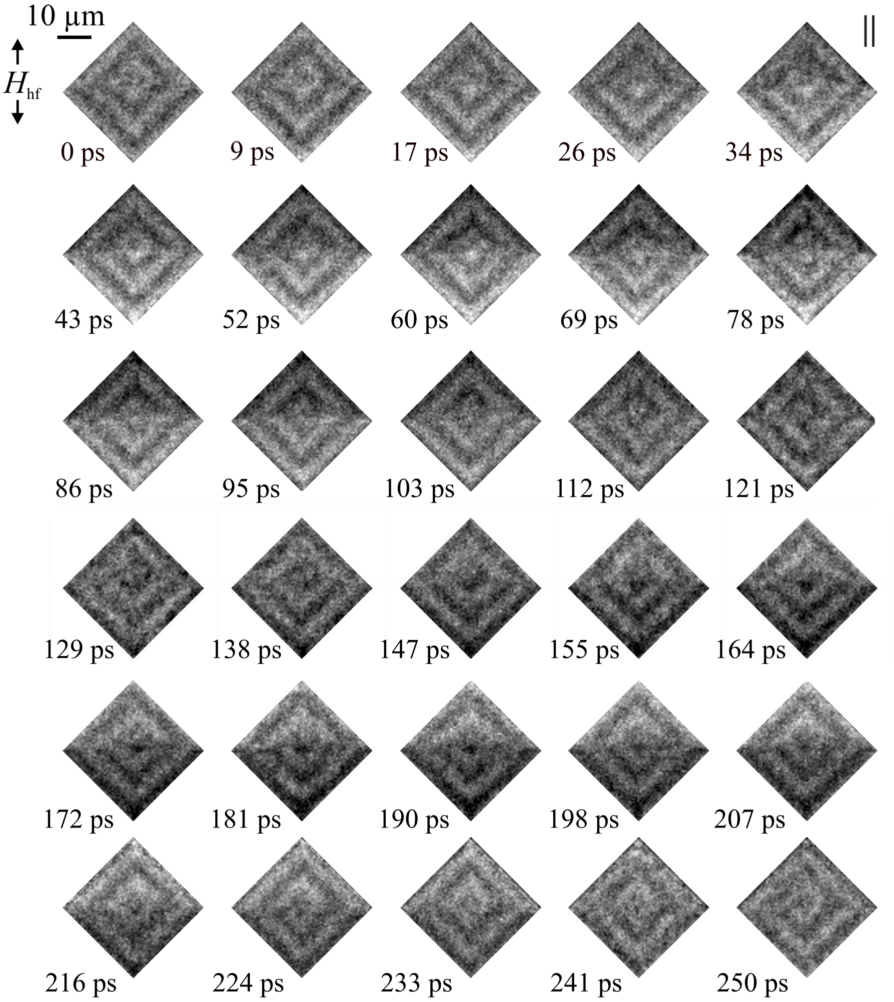

Figure 6.3: TR-MOKE images showing magnetization response of magnetic element to field frequencies of 4 GHz for a full period of excitation. The time delay is given in picoseconds for all images (adapted form [106]).

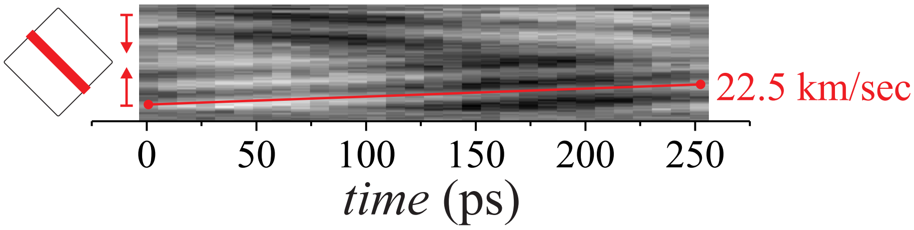

Figure 6.4: Temporal evolution of magnetic domains cross-sectional TR-MOKE signal for an AC filed with a frequency of 4 GHz [106].

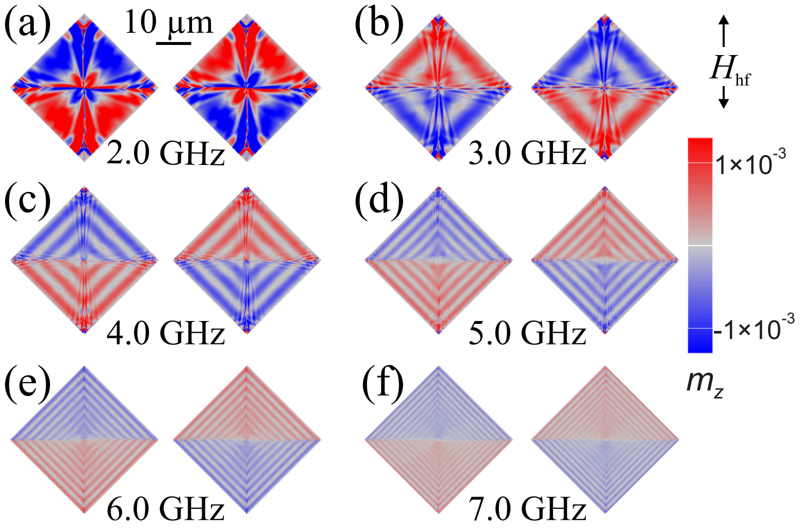

Figure 6.5: (a)-(f) Dynamic magnetization dynamic response of sample in a Landau state obtained from simulation. m_z shows the variation of the out-of-plane magnetization [106].

Understanding the physical nature of the spin-wave generation is not straightforward. From experimental TR-MOKE observation, it is not clear whether spin waves are generating from the magnetic vortex at the center of the magnetic element or from the edges of it. To understand the origin and fundamental properties of observed spin waves, the magnetic dynamic response of magnetic element to an AC excitation field with frequencies from 2 GHz up to 7 GHz and a base-to-peak field amplitude of 0.12 mT is simulated. The used simulation parameters are as follows:

- In-plane cell size = 15 nm
- Vertical dimension of the cell (film thickness) = 30 nm
- Saturation polarization (J_s) = 1 T
- Exchange stiffness constant (A) = 1.3×10^{-11} J/m
- $\alpha = 0.01$

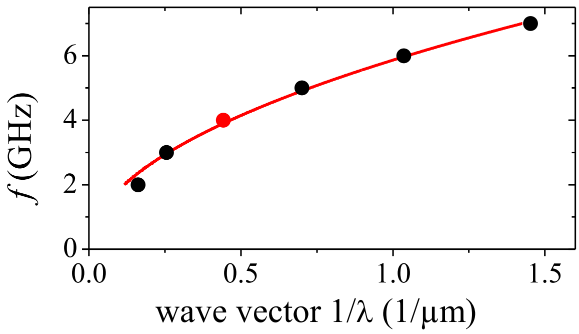

Figure 6.6: The dispersion relation of the propagated spin waves calculated from simulation data of Fig. 6.5 [106].

Figure 6.5 displays the simulated magneto-dynamic out-of-plane response of the sample in its Landau state, exposed to an AC field with varying frequencies. Similar to the experimental TR-MOKE imaging results, the precessional out-of-plane response of magnetization is seen. However, the amount of magnetization precession decreases at higher frequencies. For all shown frequencies, spin waves are visible. Moreover, consistent with TR-MOKE results, in the simulation, spin waves are restricted to the individual domains, and the wavefronts are aligned parallel to the edges of the element. It is also determined that by increasing the AC field frequency, the spin waves period decreases. The corresponding dispersion relation derived from the micromagnetic simulations is displayed in Fig. 6.6 [106]. Such dependency is an indication of Damon–Eschbach spin-wave modes (see Fig. 2.5).

Figure. 6.7 exhibits the temporal modeled magnetization dynamics response of the sample exposed to an excitation field with a frequency of 4 GHz. Comparing the modeled images from Fig. 6.7 to the experimental results Fig. 6.3 show nearly identical responses. In addition, the spin wave propagation velocity calculated from simulation results is in well agreement with the calculated valued from experimental results. Based on the results shown in Fig. 6.8 a velocity of $V_{sw} = 21.8$ km/s is calculated from the simulated data.

The used magnetic field history of the simulation is shown in Fig. 6.9 (a).

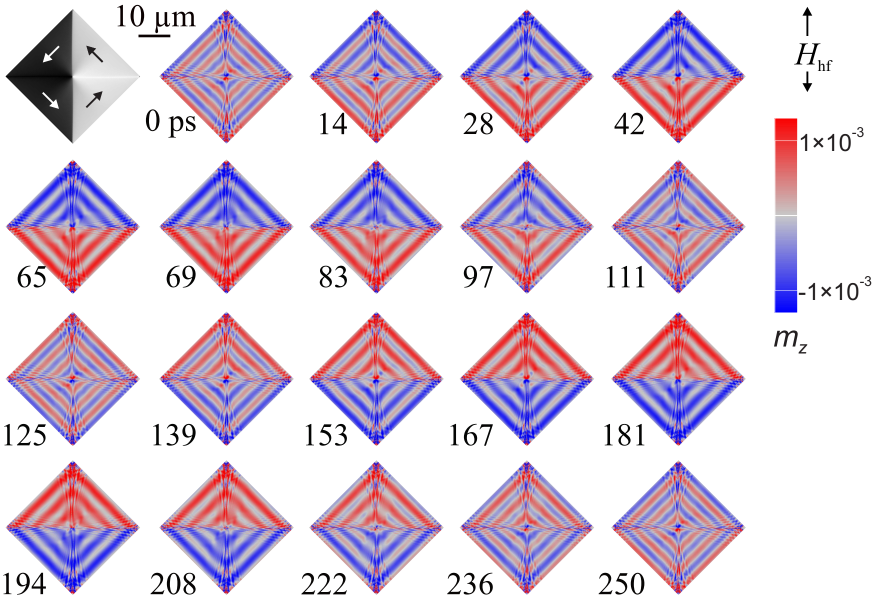

Figure 6.7: Temporal evolution of dynamic magnetization response acquired from simulation for H_{hf} at 4 GHz. m_z is showing the variation of the out-of-plane magnetization m_z. The time delay indicated in the plot is in picoseconds [106].

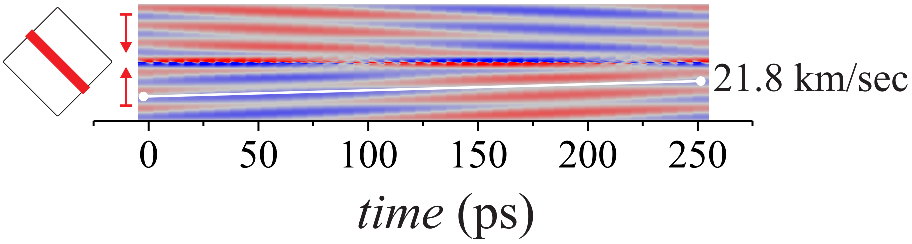

Figure 6.8: Temporal evolution of magnetic domains cross-sectional simulated TR-MOKE signal for an AC filed with a frequency of 4 GHz.

The lateral development of magnetization m_z, with time over the first 7 cycles of field excitation, is displayed in Fig. 6.9 (b). The corresponding cross-sectional development of m_z with time is plotted in Fig. 6.9 (c). It can be seen by switching on the dynamic field; spin-waves are generated from the edges of the elements. With every cycle of field excitation, another spin-wave is emitted from the element's edge to the center. The main reason for spin-wave emittance from the edge regions with applied homogeneous excitation field is the local dynamic demagnetization field N_{dyn}, which results in an effective field distribution close to the element's borders. In other words, spin waves are generated from local resonant excitations in the inhomogeneous dynamic magnetization field near the sample's boundaries [106].

In short, it has been shown in the simulation that the spin waves are generating from magnetic elements' edges and then propagate to the center of the element. From simulation results, no significant spin wave generation from the central vortex is observed.

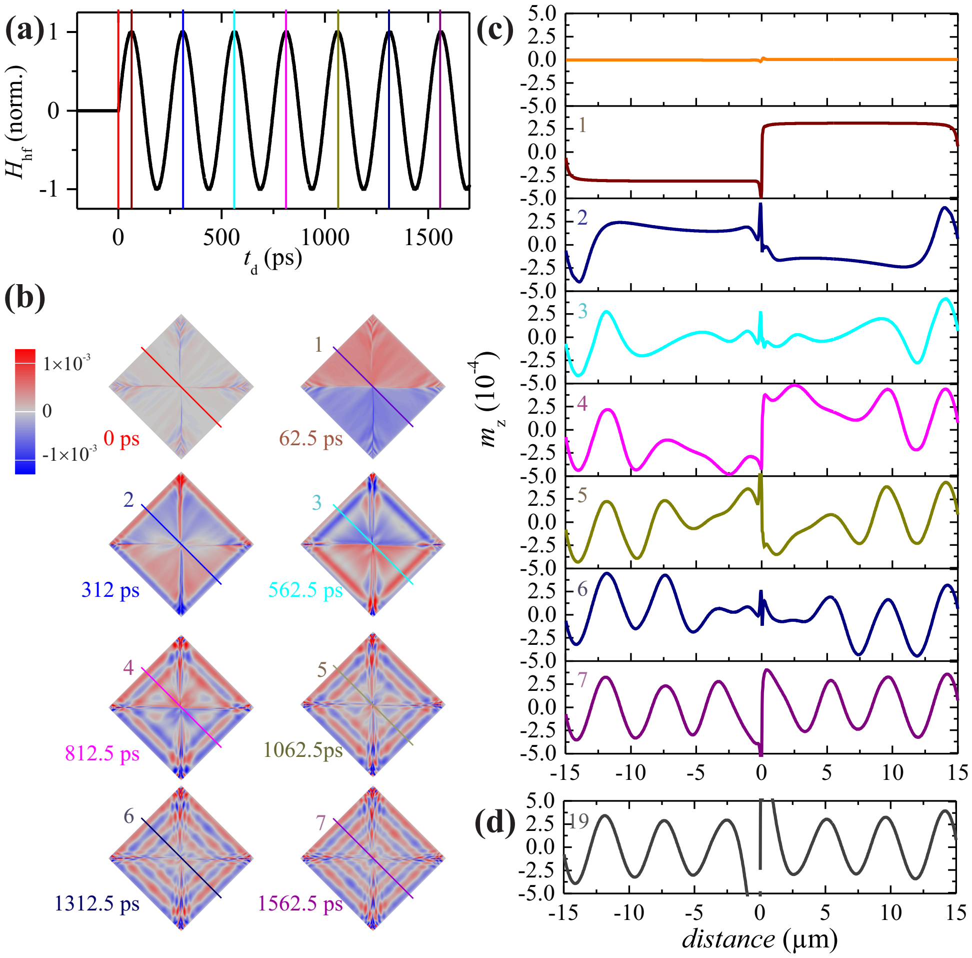

Figure 6.9: (a) Time evolution of excitation field and (b) out-of-plane magnetization m_z. (c) Evolution of m_z across the center of the element 1700 ps after applying AC field with a frequency of 4 GHz. (d) out-of-plane magnetization m_z, across the center of the element after the 19th field cycle [106].

Chapter 7

Magnetodynamics in Multilayer Structured Magnetic Films

7.1 Introduction

In this chapter the magnetodynamics of weakly antiferromagnetically coupled Ta (3nm)/($Co_{40}Fe_{40}B_{20}$) (25nm)/Ru (0.8nm)/($Co_{40}Fe_{40}B_{20}$) (25nm)/TaN (5nm) film is investigated. As mentioned in Chapter 3, the film used here is lithographically patterned into an antidot array. The focus of the current chapter is to understand the dynamic magnetization behavior of a structured multilayer magnetic film. Therefore, multilayer film magnetic dynamic properties are compared to a single layer film. Furthermore, the impact of patterning on magnetization dynamics is reported. TR-MOKE direct imaging of such a magnetic system reveals complicated magnetostatically excited modes and exhibits the changing character of these modes by changing the DC magnetic bias field. Similar to previous chapters, the excited superimposed standing spin-waves between the antidot arrays is probed using TR-MOKE. Such excited spin waves are studied in Ref. [107], based on the information acquired by scanning time-resolved MOKE. In this project, the direct imaging of these modes is shown. The work demonstrates another method to tailor the magnetization dynamics in patterned magnetic elements that can be used in magnonics related applications

[108].

As discussed in Chapter 6, the realization of complex magnetization dynamics behavior requires both experimental and theoretical simulation. The focus of this chapter is on the experimental side, and the simulation part is the subject of another doctoral thesis. Therefore, the numerical calculation is out of the scope of this chapter.

7.2 Results and Discussion

To inspect the impact of film structuring on basic magnetic properties of the magnetic film, the magnetic hysteresis loops of magnetic samples are measured inductively. Figure 7.1 (a) and (b) display the measured hysteresis loops of single- and multilayer unstructured films, respectively. Measurements are performed along with both easy and hard anisotropy directions of the samples. By comparing a single layer film (Fig. 7.1 (a)) to a multilayer one (Fig. 7.1 (b)), it can be noted that unlike single layer film multilayer film magnetization reversal along its easy axes takes place in two steps, which can be seen from the existence of two sub-loops. This is due to the antiferromagnetically coupling [109] of two ferromagnetic layers in which a separated switching event in each magnetic layers occurs, i.e., by decreasing the external magnetic field (H_{ex}) from saturation field (H_s) at a certain field amplitude, the first ferromagnetic layer reverts its magnetization direction and then by further magnetic field reduction the second layer switches.

Figure. 7.1 (c-j) exhibits the hysteresis loops of various antidot sizes and configurations for single (left plots) and multilayer samples (right plots). As mentioned in Chapter 3, for ease of expression, antidots configurations in this text are coded in a way that reflects the sample patterning details. The samples' name is coded as "nx-md", where "n" indicates the diameter of antidots in μm. "x" shows either "s" or "h", which are standing for square or hexagonal packing of

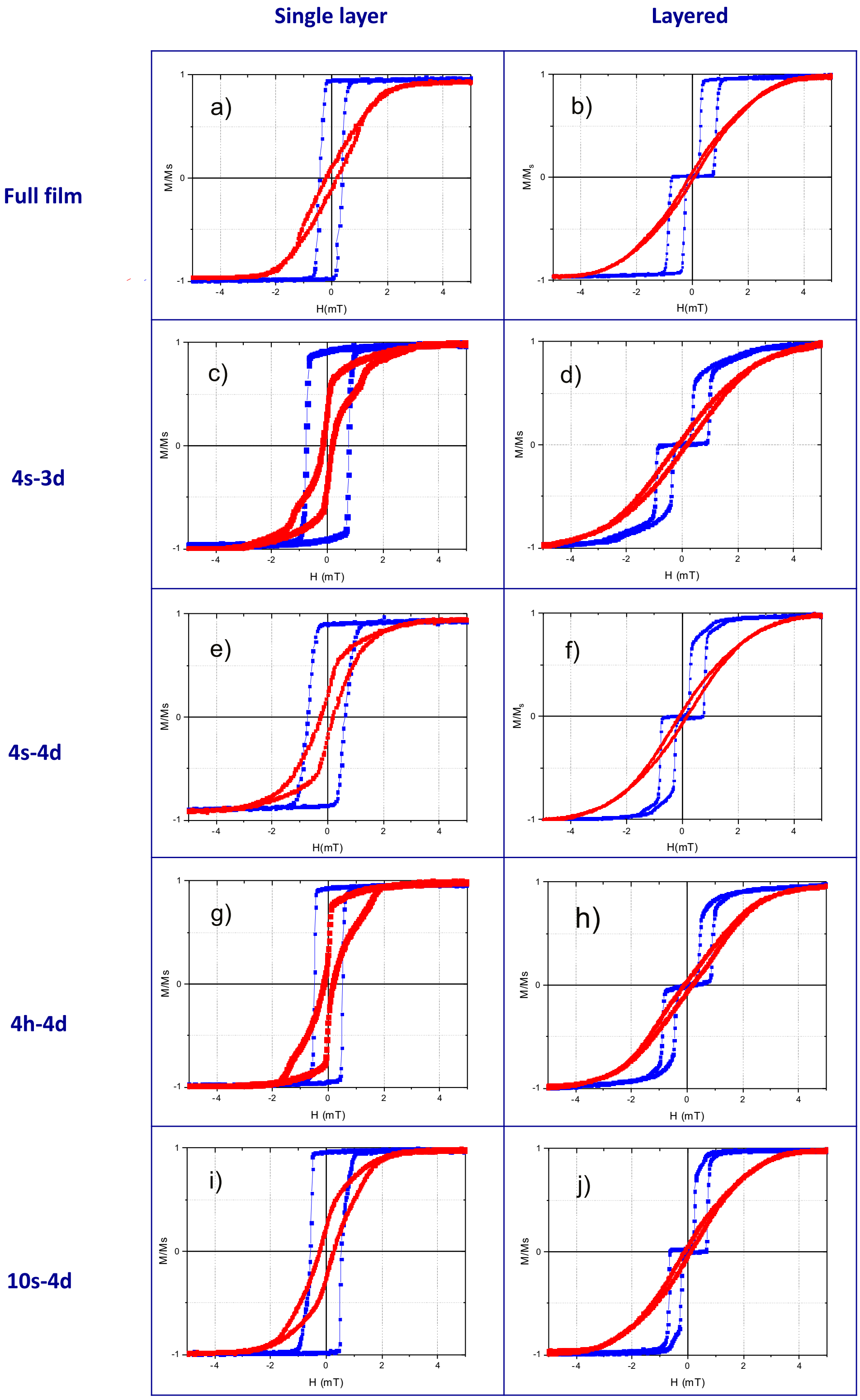

Figure 7.1: Magnetic hysteresis loops of (a) and (b) of unstructured single- and multi-layer, respectively. (c-j) Various antidot arrangements in single (left plots) and multilayer (right plots) films along sample easy (blue) and hard (red) anisotropy axis.

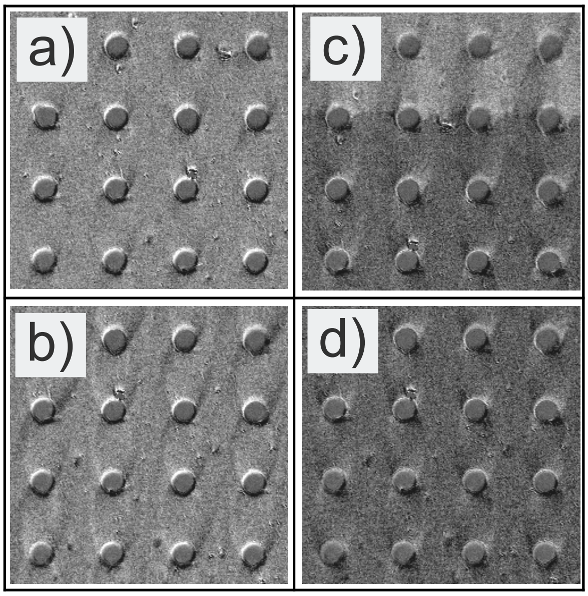

Figure 7.2: Static MOKE images of structured single layer film at a DC bias field of (a) 1 mT, (b) -0.57 mT, (c) -0.68 mT, (d) -0.78 mT.

antidots respectively. "m" shows the center-to-center distance of antidots where "d" is the diameter of the antidots.

As seen in Fig. 7.1, in general antidot patterning increases magnetic samples coercivity (H_c) along the easy anisotropy axis. This is due to the pinning effect of domain walls at the antidot edge and enhanced demagnetization fields [110]. Furthermore, structuring the films increases the sample's saturation field (H_s). This is even more pronounced in the case of multilayer films.

Figure 7.2 shows the static images of a single layer structured sample with an antidot 4s-4d layout. Starting from the sample's magnetic saturation field H_s (Figure 7.2 (a)), decreasing the bias field to H_{bias} = -0.57 mT regions form where the stray fields of two antidots are coupled parallel to the direction of the external field (Fig. 7.2 (b)). By further decreasing the field to H_{bias} = -0.68 mT (Fig. 7.2 (c)), the magnetic film magnetization partly switches. At H_{bias} = -0.78 mT the sample's magnetization reversal takes place. This is indicated in the reverse contrast of the MOKE image shown in Fig. 7.2 (d).

Figure. 7.3 (a-c) displays the static magnetic domain configuration of multilayer 4s-4d sample with corresponding magnetic hysteresis loop and permeability spectra. As seen in Fig. 7.3 (a), starting from a DC bias field of slightly below saturation field (H_s = 2.0 mT) due to the existence of demagnetizing field at the antidot boundaries, magnetic domains start to nucleate at the antidotes circumference. By decreasing the bias field to H_{bias} = 0.4 mT a magnetic state forms, which is the combination of areas where two films magnetizations are parallel and anti-parallel with respect to each other. Further decreasing the field (H_{bias} = -0.8 mT) places the layers in a totally anti-parallel state. At H_{bias} = -1.4 mT again the combination of parallel and anti-parallel regions are formed. At H_{bias} = -2.0 mT sample magnetization is reverted.

To measure the dynamic magnetic characteristics of magnetic elements, the dynamic magnetic permeability spectra is measured using the pulsed inductive microwave magnetometry (PIMM) technique. Figure 7.4 (a-b) shows the measured resonance frequency of structured and unstructured samples in various DC bias fields. The blue and red show single layer and multilayer films. Comparing unstructured samples (Fig. 7.5 (a)) to the structured samples (4s-4d antidots) (Fig. 7.5 (b)), a resonance frequency drop is seen. This resonance frequency drop at a bias field close to H_{bias} = 0 mT is the highest for the single-layer structured film. The resonance frequency drop is due to magnetic domain formation and, consequently, the reduction of active magnetic volume in the magnetic element [82]. At H_{bias} = 0 mT, the resonance frequency of the structured multilayer film is approximately 30% (400 MHz) larger than the corresponding single-layer film. This is a clear advantage of multilayer films over the single layers. Figure 7.4 (a-b) shows the f_{res}^2 versus bias field. As shown at a high enough bias field, all the samples show a Kittel behavior. This is attributed to the fact that at a larger bias field (close to H_s) a nearly uniform magnetic configuration is forming.

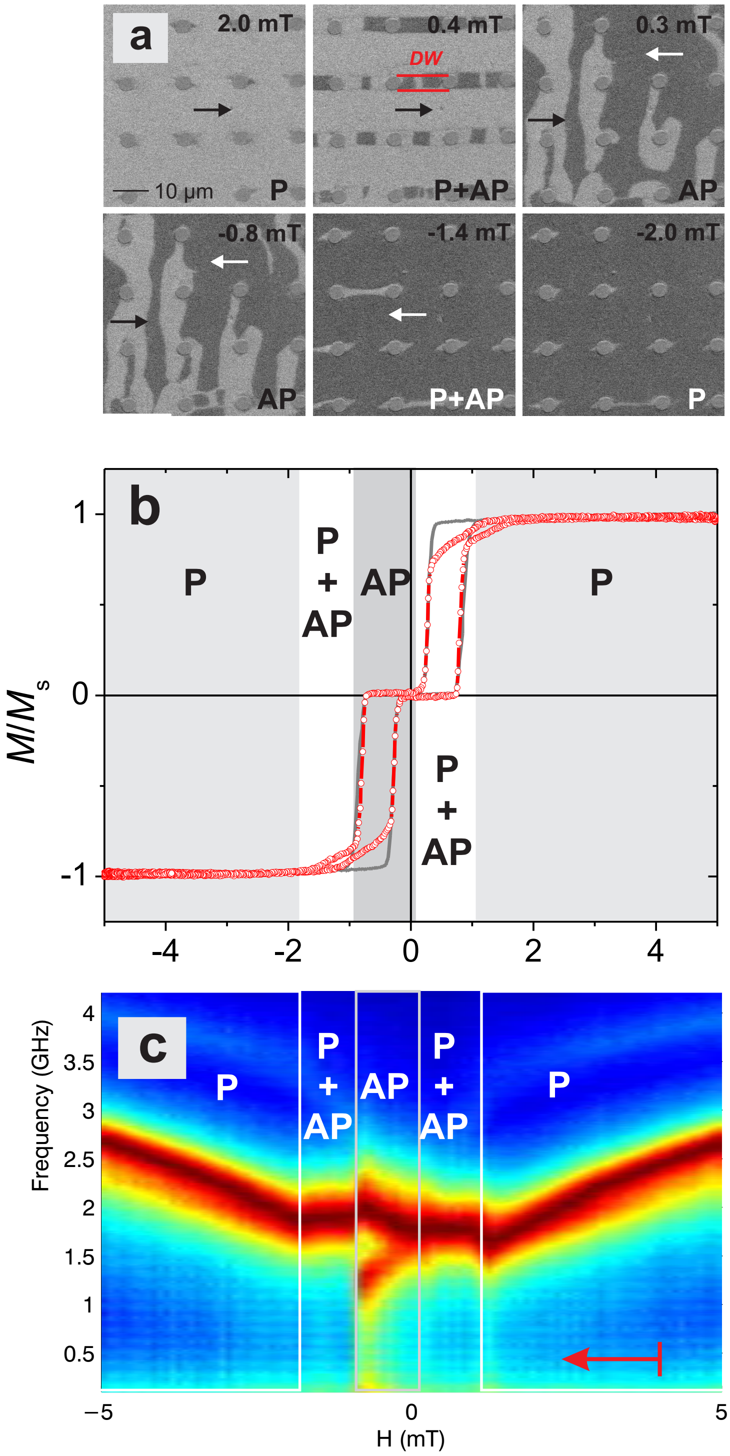

Figure 7.3: Static magneto optical images of multilayer 4s-4d sample at a DC bias fields from H_{bias} = 2 mT to H_{bias} = -2 mT. (b) corresponding magnetic hysteresis loop of sample with details of layers magnetization direction of layers with respect to each other (P: parallel, AP: anti-parallel). (c) complementary permeability spectra of sample.

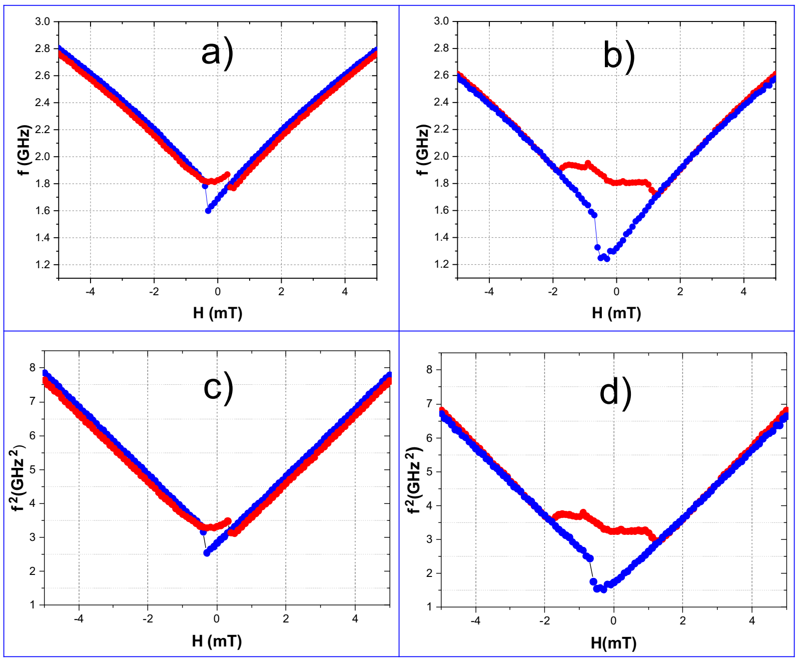

Figure 7.4: (a) and (b) measured resonance frequency for unstructured and structured (4s-4d antidot) single layer (blue) and multilayer (red) films in various DC bias field. (c)-(d) corresponding f_{res}^2 plots.

Figure 7.5 (a-b) shows the permeability spectra of unstructured single and multilayer samples. In the case of the single-layer unstructured sample (Fig. 7.5 (a)), the permeability spectra show a single resonance frequency whereas the multilayer unstructured film (Fig. 7.5 (b)) shows permeability peak splitting at low bias fields. In other words, the structured multilayer film has two resonance frequencies at low bias fields. At higher bias fields, both samples have an identical permeability response. Figure 7.5 (c-j) displays the PIMM results of structured single (left) and multi-layer (right) films. As seen from the permeability spectra, in structured single layer samples, at low bias fields, there is a region in the permeability spectrum, where the resonance frequency drops to lower values. As mentioned, a low resonance frequency is a bottleneck in high-frequency applications.

Furthermore, by changing the antidot packing from a square like order to a hexagonal arrangement in multilayer films, the resonance frequency peak

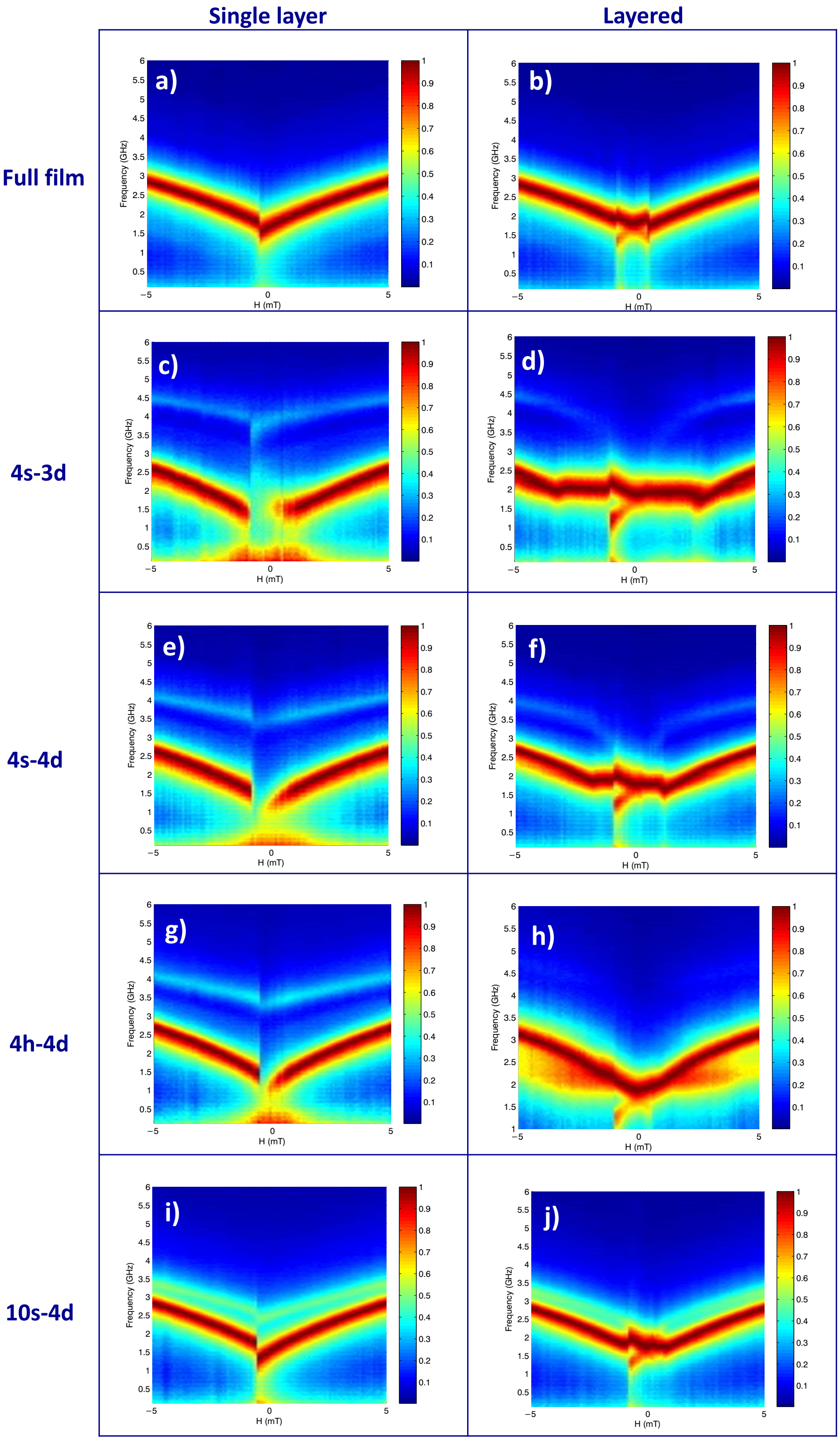

Figure 7.5: Measured permeability spectra map of (a)-(b) unstructured single and multilayer films respectively. (c)-(j) structured single (left plots) and multilayer films (right plots).

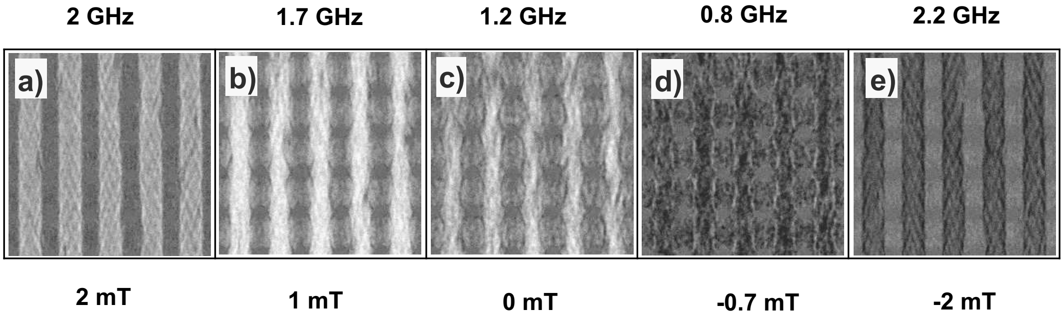

Figure 7.6: (a)-(e) TR-MOKE images obtained from single layer structured magnetic film using an AC excitation field along sample hard anisotropy axis. The used DC field amplitude and AC field frequency is indicated in the plots.

is broadened. Moreover, by increasing the distance between antidots, the resonance frequency peak became narrower.

Next, the frequency response of the single and multilayer samples are imaged with TR-MOKE. To do so, the magnetic elements are initialized with external DC magnetic fields. Then a continuous AC excitation field with a frequency identical to the corresponding resonance frequency of the sample at any given bias DC field is applied.

Figure 7.6 shows the TR-MOKE images obtained from a single layer structured magnetic element with 4s-4d antidot configuration. In Fig. 7.6 (a), at a magnetic bias DC field of H_{ex}= 2 mT magnetic flux channels with a spin-wave interference pattern in the area confined by antidots can be seen. At H_{ex}= 1 mT (Fig. 7.6 (b)) vertical flux channels between antidots exists, although there is no sign of spin wave interference. At H_{ex}= 0 mT (Fig. 7.6 (c)) in addition to the vertical channels, a non-uniform modulated pattern appears horizontally along sample's hard anisotropy axis. Figure 7.6 (d) shows the magnetization dynamics response at H_{ex}= -0.7 mT. There is a magnetically non-homogeneous area and signs of domain formation around the antidots. This dynamic magnetization response is well agreed with PIMM results, where the f_{res} shows a sudden fall. By reaching H_{ex}= -2 mT a magnetization dynamic response similar to H_{ex}= 2 mT is visible.

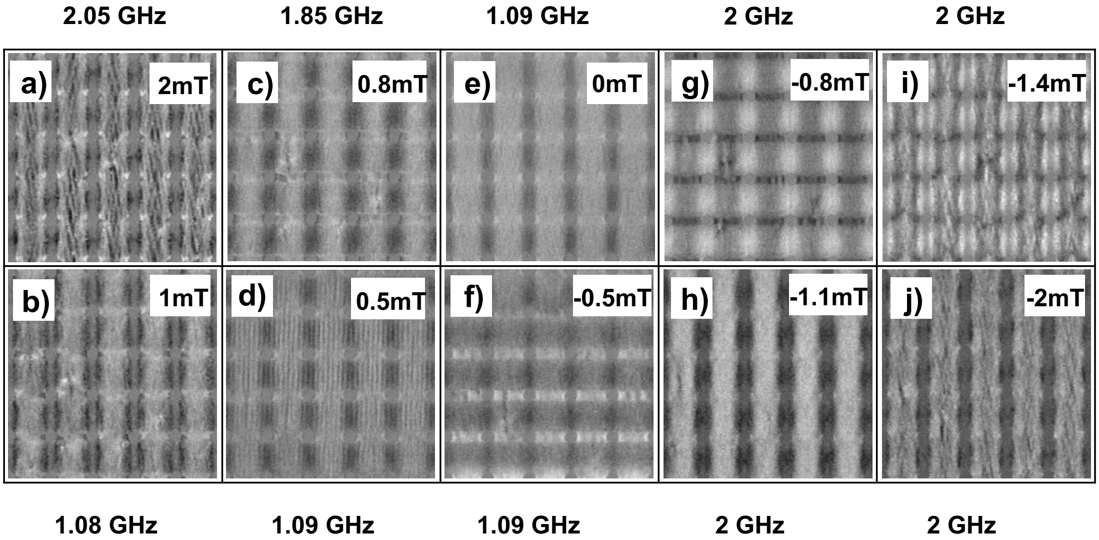

Figure 7.7: (a)-(j) TR-MOKE images obtained from the multilayer sample with an antidot configuration of 4s-4d. The excitation DC field amplitude and corresponding AC field frequencies are indicated in the plot. The AC excitation field is applied along the sample's hard anisotropy direction.

The magnetization dynamics in multilayer films are more complicated than single-layer ones. Figure 7.7 exhibits the TR-MOKE images acquired from the multilayer sample with an antidot configuration of 4s-4d. Starting from a bias field H_{ex}= 2 mT (Fig. 7.7 (a)), in the restricted areas by two antidots, magnetic flux channels along sample's easy axis form. The flux channels are aligned parallel to the direction of the excitation field. The magnetization dynamics in these channels are not uniform, and a modulated oscillation of spins that forms spin-wave interference pattern can be observed. This complex dynamics response arises from the various spatial dipolar interactions. The result of such spin-antidot interactions is the formation of magnetic charges at the antidot edges. The formed magnetic charges, in turn, produce a local anisotropic energy density of the spins [111]. Hence, the spin precession occurs mainly due to the spin confinement through the antidot edges and localized inhomogeneous internal field [112]. In addition, transversely, in the vicinity of the antidot edges, there are magnetic domains nucleation sites.

By decreasing the bias field to H_{ex}= 1 mT (Fig. 7.7 (b)) at the boundary of flux channels, small regions with a different oscillation phase can be observed.

This anti-phase response can be seen in the reverse contrast regions, which is a sign of locally out-of-phase dynamic response. Such behavior suggests a magnetic flux transferring mechanism due to stray field coupling of neighboring spins. Further decreasing of the external field to H_{ex}= 0.8 mT (Fig. 7.7 (c)), three distinct magnetodynamic characteristics are visible. This includes the region between two antidots horizontally (along hard anisotropy axis), vertically (along easy anisotropy axis) between two antidots and the square region surrounded by each four antidots. At H_{ex}= 0.5 mT and H_{ex}= 0 mT (Fig. 7.7 (d) & (e) respectively) the effect of layering starts to appear. Figure 7.7 (e) displays the magnetic dynamics response of the multilayer structured film at a magnetic bias field of H_{ex}= 0 mT, where the horizontal channels between antidots are less pronounced.

At a bias field of H_{ex}= -0.5 mT (Fig. 7.7 (f)), again three types of magnetic responses are visible, which can be seen in the vertical and horizontal directions, as well as the central of the are confined by four antidots. As expected, at H_{ex}= -0.8 mT (Fig. 7.7 (g)) the excited magnetization dynamic modes are identical to the H_{ex}= 0.8 mT response with a reversed sign. Similarly, at H_{ex}= -1 mT (Fig. 7.7 (h)) the dynamic magnetization response is the mirrored state of H_{ex}= 1 mT. By reaching the bias field of H_{ex}= -1.4 mT (Fig. 7.7 (i)), the observed basket-weave pattern inside flux channels appears one more time, and then it gets more pronounced at H_{ex} = -2 mT (Fig. 7.7 (j)).

Chapter 8

Summary

In this project, an in-house TR-MOKE microscopy method, as well as the pulsed inductive microwave magnetometry set up, has been built. A detailed explanation of these two methods can be found in Chapter 3. These two complementary techniques are used to study the magnetization dynamics in various lithographically patterned magnetic films. The results of such studies play a significant role in the understanding of complicated magnetization dynamics in structured magnetic films. In addition, it provides knowledge of tailoring dynamic magnetic properties in such a magnetic medium.

In Chapter 4, TR-MOKE was used to identify different fundamental magneto-dynamic modes in magnetic thick-film elements with a Landau-like domain configuration. Using this method, areas with differing high-frequency permeability are distinguished. Moreover, a method to separate the in- and out-of-plane Kerr signals has been proposed. With this, a more elaborated model to explain the fast magnetization processes in soft magnetic elements is suggested.

Also, it is shown that despite using an in-plane AC field to excite the magnetic element, out-of-plane magnetization response, as well as dynamic magnetostatic coupling between magnetic domains, are observed. The TR-MOKE images also show a phase mismatch between the AC excitation magnetic field and the induced domain wall motion. Unlike other suggested mechanisms, the TR-MOKE direct imaging proves the existence of magnetization precession in magnetic domain walls at the resonance frequency of the magnetic element. It is also seen that at magnetic resonance AC frequency switches the magnetic domain configuration, indicating a relation of the dynamic domain modes with switching events.

In Chapter 5, direct observation of existence, generation, and the propagation of spin waves from oscillating magnetic domain walls are demonstrated. The direct observation of spin waves exhibits the benefits of developed TR-MOKE. It is shown that the spin waves can be generated from an oscillated domain wall. These radiated spin waves can propagate along with the areas restricted by narrow magnetic domains. Also, it has been demonstrated that by varying the oscillation frequency, the wavelength of the spin waves can be tuned in a controlled manner. Independent from excitation field frequency, a constant velocity of spin-wave propagation is observed. Therefore, a method to tailor the spin waves generation is proposed. This is based on modifying the magnetic domain and domain structure by a DC magnetic field that leads to domain wall configuration change. Moreover, it was shown that spin waves could be guided by magnetic domain walls instead of using an antenna or wave-guide.

In Chapter 6, using experimental results of TR-MOKE and complementary micromagnetic simulations, the existence of edge emitted spin waves are shown. It is found that spin waves are generated by local resonant excitations from areas near the sample's edges, and then propagate to the center of the element. The spin-waves generation was found to be due to the in-homogeneous dynamic magnetization field at the corners and edges of the elements. The frequencies of the spin waves were shown to be tunable by the excitation frequency. The spin waves in the magnetic domains show very low damping over several micrometers. Also, it is proven that domain walls are acting as a natural border for spin waves propagation, whereas magnetic elements edges provide a source to create plane spin waves, which are annihilating by domain walls.

In Chapter 7, the magnetodynamics in weakly antiferromagnetically coupled Ta (3nm)/($Co_{40}Fe_{40}B_{20}$) (25nm)/Ru (0.8nm)/($Co_{40}Fe_{40}B_{20}$) (25nm)/TaN (5nm) structured magnetic film is presented. Multilayer film dynamic properties are compared to the single-layer film. Furthermore, the impact of patterning on magnetization dynamics is shown. TR-MOKE direct imaging reveals complicated magnetostatically excited modes in such films and exhibits the changing characteristics of these modes by changing of DC magnetic bias field. This chapter demonstrates another method to tailor the magnetization dynamics in patterned magnetic elements. A variety of magnetic thin films from a single layer magnetic film, as well as antiferromagnetically coupled ones, are investigated. It is shown that layering partly compensates the magnetic element resonance frequency f_{res} drop caused by film structuring.

Appendix A

List of Published Articles

List of published articles during this doctoral study:

- B. Mozooni, J. McCord, **“Direct observation of closure domain wall mediated spin waves"**, Applied Physics Letters 107.4 (2015), p. 042402.

- B. Mozooni , T. von Hofe, J. McCord, **“Picosecond wide-field magneto-optical imaging of magnetization dynamics of amorphous film elements"**, Physical Review B 90 (2014), p. 054410.

- M. Lohman, B. Mozooni, J. McCord **“Homogeneous microwave field emitted propagating spin waves: Direct imaging and modeling"**, Journal of Magnetism and Magnetic Materials 450 (2018), pp. 7 –12.

- R. Holländer, M. Lohman, C. Müller, B. Mozooni, J. McCord **“Component selection in time-resolved magneto-optical wide-field imaging for the investigation of magnetic microstructures"**, Journal of Magnetism and Magnetic Materials 432, (2017), pp. 283-290.

- NO. Urs, B. Mozooni, P. Mazalski, M. Kustov, P. Hayes, S. Deldar, E. Quandt, J. McCord **“Advanced magneto-optical microscopy: Imaging from picoseconds to centimeters-imaging spin waves and temperature distributions"**, AIP Advances 6, (2016), p. 055605.

- J. Trützschler, K. Sentosun, B. Mozooni, R. Mattheis, J. McCord **“Magnetic domain wall gratings for magnetization reversal tuning and confined dynamic mode localization"**, Scientific Reports 6, (2016), p. 30761.

- T. von Hofe, N. O. Urs, B. Mozooni, T. Jansen, C. Kirchhof, D. E. Bürgler, E. Quandt, J. McCord, **“Dual wavelength magneto-optical imaging of magnetic thin films"**, Applied Physics Letters 103, (2013), p. 142410.

Appendix B

Copyrights Acknowledgment

- Chapter 4: see next page
- Chapter 5: see next page
- Chapter 6: see next page
- Latex template: modified from http://www.LaTeXTemplates.com

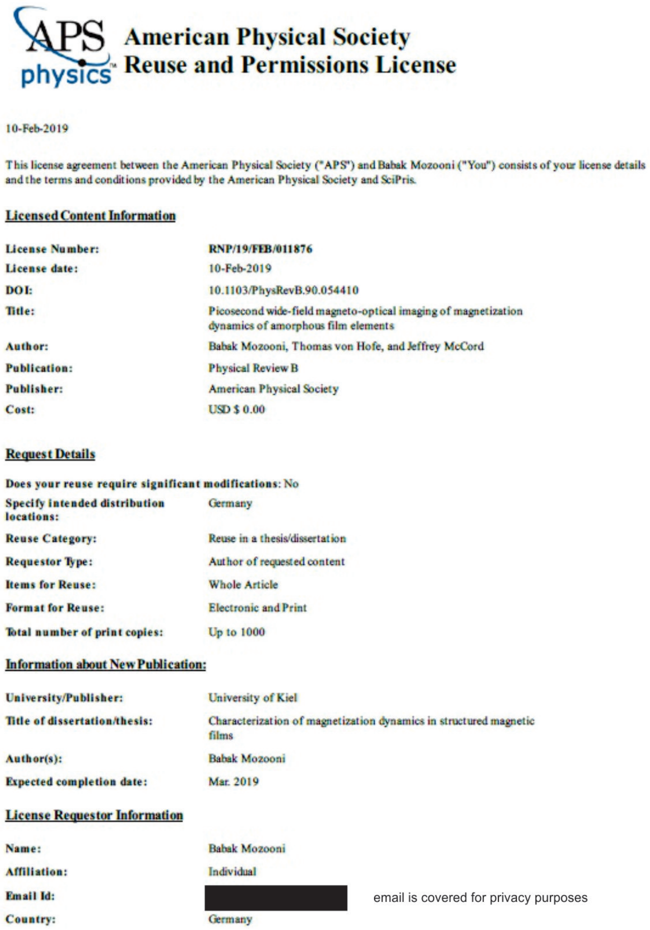

American Physical Society Reuse and Permissions License

10-Feb-2019

This license agreement between the American Physical Society ("APS") and Babak Mozooni ("You") consists of your license details and the terms and conditions provided by the American Physical Society and SciPris.

Licensed Content Information

License Number:	RNP/19/FEB/011876
License date:	10-Feb-2019
DOI:	10.1103/PhysRevB.90.054410
Title:	Picosecond wide-field magneto-optical imaging of magnetization dynamics of amorphous film elements
Author:	Babak Mozooni, Thomas von Hofe, and Jeffrey McCord
Publication:	Physical Review B
Publisher:	American Physical Society
Cost:	USD $ 0.00

Request Details

Does your reuse require significant modifications: No

Specify intended distribution locations:	Germany
Reuse Category:	Reuse in a thesis/dissertation
Requestor Type:	Author of requested content
Items for Reuse:	Whole Article
Format for Reuse:	Electronic and Print
Total number of print copies:	Up to 1000

Information about New Publication:

University/Publisher:	University of Kiel
Title of dissertation/thesis:	Characterization of magnetization dynamics in structured magnetic films
Author(s):	Babak Mozooni
Expected completion date:	Mar. 2019

License Requestor Information

Name:	Babak Mozooni
Affiliation:	Individual
Email Id:	[redacted]
Country:	Germany

email is covered for privacy purposes

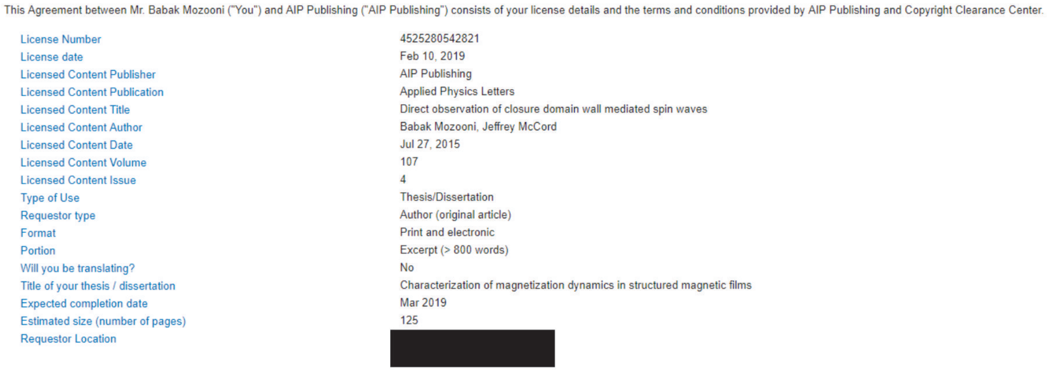

This Agreement between Mr. Babak Mozooni ("You") and AIP Publishing ("AIP Publishing") consists of your license details and the terms and conditions provided by AIP Publishing and Copyright Clearance Center.

License Number	4525280542821
License date	Feb 10, 2019
Licensed Content Publisher	AIP Publishing
Licensed Content Publication	Applied Physics Letters
Licensed Content Title	Direct observation of closure domain wall mediated spin waves
Licensed Content Author	Babak Mozooni, Jeffrey McCord
Licensed Content Date	Jul 27, 2015
Licensed Content Volume	107
Licensed Content Issue	4
Type of Use	Thesis/Dissertation
Requestor type	Author (original article)
Format	Print and electronic
Portion	Excerpt (> 800 words)
Will you be translating?	No
Title of your thesis / dissertation	Characterization of magnetization dynamics in structured magnetic films
Expected completion date	Mar 2019
Estimated size (number of pages)	125
Requestor Location	[redacted]

address is covered for privacy purposes

Title:	Homogeneous microwave field emitted propagating spin waves: Direct imaging and modeling
Author:	Mathis Lohman,Babak Mozooni,Jeffrey McCord
Publication:	Journal of Magnetism and Magnetic Materials
Publisher:	Elsevier
Date:	15 March 2018

© 2017 Elsevier B.V. All rights reserved.

Logged in as:
Babak Mozooni
Account #: [redacted]

Please note that, as the author of this Elsevier article, you retain the right to include it in a thesis or dissertation, provided it is not published commercially. Permission is not required, but please ensure that you reference the journal as the original source. For more information on this and on your other retained rights, please visit: https://www.elsevier.com/about/our-business/policies/copyright#Author-rights

Bibliography

[1] H. Sepehri-Amin et al. “Design of spin-injection-layer in all-in-plane spin-torque-oscillator for microwave assisted magnetic recording”. In: *Journal of Magnetism and Magnetic Materials* 476 (2019), pp. 361 –370.

[2] B.D. Terris, T. Thomson, and G. Hu. “Patterned media for future magnetic data storage”. English. In: *Microsystem Technologies* 13.2 (2007), pp. 189–196.

[3] B D Terris and T Thomson. “Nanofabricated and self-assembled magnetic structures as data storage media”. In: *Journal of Physics D: Applied Physics* 38.12 (2005), R199.

[4] M. Cubukcu et al. “Ultra-Fast Perpendicular Spin–Orbit Torque MRAM”. In: *IEEE Transactions on Magnetics* 54.4 (2018), pp. 1–4.

[5] Johan Akerman. “Toward a Universal Memory”. In: *Science* 308.5721 (2005), pp. 508–510.

[6] S. P. Li, Santosh Kulkarni, and Saibal Roy. “Erase/restorable asymmetric magnetization reversal in polycrystalline ferromagnetic films”. In: *Journal of Applied Physics* 112.10, 103918 (2012), p. 103918.

[7] A A Serga, A V Chumak, and B Hillebrands. “YIG magnonics”. In: *Journal of Physics D: Applied Physics* 43.26 (2010), p. 264002.

[8] Alexey B. Ustinov, Andrei V. Drozdovskii, and Boris A. Kalinikos. “Multifunctional nonlinear magnonic devices for microwave signal processing”. In: *Applied Physics Letters* 96.14, 142513 (2010), p. 142513.

[9] S. Neusser and D. Grundler. “Magnonics: Spin Waves on the Nanoscale”. In: *Advanced Materials* 21.28 (2009), pp. 2927–2932.

[10] V. V. Kruglyak, S. O. Demokritov, and D. Grundler. “Magnonics”. In: *Journal of Physics D-Applied Physics* 43.26 (2010), p. 260301.

[11] J. Ding, M. Kostylev, and A. O. Adeyeye. “Magnonic crystal as a medium with tunable disorder on a periodical lattice”. In: *Physical Review Letters* 107 (2011), p. 047205.

[12] P. Nemec et al. “Antiferromagnetic opto-spintronics”. In: *Nature Physics* 14 (2018), pp. 229–241.

[13] C. Chappert, A. Fert, and F. N. Van Dau. “The emergence of spin electronics in data storage”. In: *Nature Materials* 6.11 (2007), pp. 813–823.

[14] S. A. Wolf et al. “Spintronics: A Spin-Based Electronics Vision for the Future”. In: *Science* 294.5546 (2001), pp. 1488–1495.

[15] Del Atkinson. et al. “Magnetic domain-wall dynamics in a submicrometre ferromagnetic structure”. In: *Nature Materials* 2 (2003), pp. 85–87.

[16] S. I. Kiselev et al. “Microwave oscillations of a nanomagnet driven by a spin-polarized current”. In: *Nature* 425 (2003), pp. 380–383.

[17] D. S. Gardner et al. “Integrated on-chip inductors using magnetic material (invited)”. In: *J. Appl. Phys.* 103.7 (2008), 07E927.

[18] Stuart S. P. Parkin, Masamitsu Hayashi, and Luc Thomas. “Magnetic Domain-Wall Racetrack Memory”. In: *Science* 320.5873 (2008), pp. 190–194.

[19] Pavel F. Bessarab et al. “Lifetime of racetrack skyrmions”. In: *Scientific Reports* 8.3433 (2018).

[20] Sang-Koog Kim. “Micromagnetic computer simulations of spin waves in nanometre-scale patterned magnetic elements”. In: *Journal of Physics D: Applied Physics* 43.26 (2010), p. 264004.

[21] Jason M. Bartell et al. “Imaging Magnetization Structure and Dynamics in Ultrathin $Y_3Fe_5O_{12}$/Pt Bilayers with High Sensitivity Using the Time-Resolved Longitudinal Spin Seebeck Effect”. In: *Phys. Rev. Applied* 7 (4 2017), p. 044004.

[22] T. Maruyama et al. “Observations of charge-ordered and magnetic domains in LuFe2O4 using transmission electron microscopy”. In: *Phys. Rev. B* 86 (5 2012), p. 054202.

[23] C. Cheng, W. Cao, and W.E. Bailey. “Phase-resolved imaging of edge-mode spin waves using scanning transmission x-ray microscopy”. In: *Journal of Magnetism and Magnetic Materials* 424 (2017), pp. 12 –15.

[24] V. Uhlir et al. “Dynamic switching of the spin circulation in tapered magnetic nanodisks”. In: *Nature Nanotechnology* 8 (2013), pp. 341–346.

[25] R. Brandt et al. “Size-dependent magnetization switching characteristics and spin wave modes of FePt nanostructures”. In: *Journal of Applied Physics* 113.20, 203910 (2013), p. 203910.

[26] M. M. Decker et al. “Time Resolved Measurements of the Switching Trajectory of Pt/Co Elements Induced by Spin-Orbit Torques”. In: *Phys. Rev. Lett.* 118 (25 2017), p. 257201.

[27] W. Yu et al. “Time resolved scanning Kerr microscopy of hard disk writer structures with a multilayered yoke”. In: *Applied Physics Letters* 102.16, 162407 (2013), p. 162407.

[28] S. R. Singamaneni et al. “Polarized neutron reflectivity studies on epitaxial BiFeO3/La0.7Sr0.3MnO3 heterostructure integrated with Si (100)”. In: *AIP Advances* 8.5 (2018), p. 055821.

[29] K. Zhernenkov et al. “Frequency dependence of magnetization reversal in thin Fe(100) films”. In: *Phys. Rev. B* 88 (2 2013), p. 020401.

[30] Nara Rubiano da Silva et al. “Nanoscale Mapping of Ultrafast Magnetization Dynamics with Femtosecond Lorentz Microscopy”. In: *Phys. Rev. X* 8 (3 2018), p. 031052.

[31] E Bellini et al. “Unexpected exchange bias behaviour in CoFeB ultrathin films for MTJ sensors investigated by Lorentz microscopy”. In: *Journal of Physics D: Applied Physics* 46.30 (2013), p. 305001.

[32] G. Gubbiotti et al. “Spin wave dispersion and intensity correlation in width-modulated nanowire arrays: A Brillouin light scattering study”. In: *Journal of Applied Physics* 124.8 (2018), p. 083903.

[33] S.O. Demokritov, B. Hillebrands, and A.N. Slavin. “Brillouin light scattering studies of confined spin waves: linear and nonlinear confinement”. In: *Physics Reports* 348.6 (2001), pp. 441 –489.

[34] C. Mathieu et al. “Lateral Quantization of Spin Waves in Micron Size Magnetic Wires”. In: *Phys. Rev. Lett.* 81 (18 1998), pp. 3968–3971.

[35] V. Demidov et al. “Nonlinear Propagation of Spin Waves in Microscopic Magnetic Stripes”. In: *Phys. Rev. Lett.* 102 (17 2009), p. 177207.

[36] Y. Tserkovnyak et al. “Nonlocal magnetization dynamics in ferromagnetic heterostructures”. In: *Rev. Mod. Phys.* 77 (4 2005), pp. 1375–1421.

[37] A. Yamaguchi et al. “Broadband ferromagnetic resonance of $Ni_{81}Fe_{19}$ wires using a rectifying effect”. In: *Phys. Rev. B* 78 (10 2008), p. 104401.

[38] G.T. Rado and J. R. Weertman. “Spin-wave resonance in a ferromagnetic metal”. In: *J. Phys. Chem. Solids* 11.3-4 (1959), pp. 315–333.

[39] S. Tamaru et al. “Measurement of magnetostatic mode excitation and relaxation in permalloy films using scanning Kerr imaging”. In: *Physical Review B* 70.10 (2004), p. 104416.

[40] A. Neudert et al. “Excitation and Imaging of Precessional Modes in Soft-Magnetic Squares”. In: *IEEE Trans. Magn.* 44.11 (2008), pp. 3083–3086.

[41] M. Kryder, P. Koeppe, and F.H. Liu. “Kerr effect imaging of dynamic processes”. In: *IEEE Trans.Magn.* 26 (1990), p. 2995.

[42] M. R. Freeman and B. C. Choi. “Advances in magnetic microscopy”. In: *Science* 294.5546 (2001), pp. 1484–1488.

[43] I. Neudecker et al. “Modal spectrum of permalloy disks excited by in-plane magnetic fields”. In: *Physical Review B* 73.13 (2006), p. 134426.

[44] Dmitry Chumakov et al. “Nanosecond time-scale switching of permalloy thin film elements studied by wide-field time-resolved Kerr microscopy”. In: *Phys. Rev. B* 71 (1 2005), p. 014410.

[45] A. Neudert et al. “Small-amplitude magnetization dynamics in permalloy elements investigated by time-resolved wide-field Kerr microscopy”. In: *Phys. Rev. B* 71.13 (2005), p. 134405.

[46] Pierre Weiss. “Lhypothese du champ molculaire et la propriet’e ferromagnetique”. In: *J. Phys. Theor. Appl.* 6 (1907), pp. 661–690.

[47] W Heisenberg. “On the theory of magnetostriction and magnetization curve”. In: *Z. Phys* 69 (1931), pp. 287–297.

[48] H Barkhausen. “Zwei mit Hilfe der neuen Verstärker entdeckte Erscheinungen”. In: *Physische Zeitschrift* 20 (1919), pp. 401–403.

[49] Bloch. “On the theory of the exchange problem and remanence phenomenon of ferromagnets”. In: *Z. Phys.* 74 (1932), pp. 295–335.

[50] F. Bitter. “On Inhomogeneities in the Magnetization of Ferromagnetic Materials”. In: *Phys. Rev.* 38 (10 1931), pp. 1903–1905.

[51] L Landau and J. Lifshitz. “On the theory of the dispersion of magnetic permeability in ferromagnetic bodies”. In: *Phys. Z. Sowjetunion* 8 (1935), pp. 153–169.

[52] B. D. Cullity and Graham C. D. *Introduction to Magnetic Materials.* Wiley-IEEE Press, 2008.

[53] J. M. D. Coey. *Magnetism and Magnetic Materials.* Cambridge University Press, 2010.

[54] H Kirchmayr. “Encyclopedia of Materials: Science and Technology”. In: Elsevier, 2001, pp. 4754–4757.

[55] J. Fassbender and J. McCord. “Magnetic patterning by means of ion irradiation and implantation”. In: *Journal of Magnetism and Magnetic Materials* 320.3–4 (2008), pp. 579 –596.

[56] Alex Hubert and Rudolf Schäfer. *Magnetic Domains: The Analysis of Magnetic Microstructures*. Springer, 2009.

[57] C KITTEL. “Physical Theory of Ferromagnetic Domains”. In: vol. 21. Reviews of Modern Physics, 1949, 541–583.

[58] A. Hubert and R. Schäfer. *Magnetic domains*. Springer Heidelberg-New York, 1998.

[59] Giorgio Bertotti. *Hysteresis in Magnetism: For Physicists, Materials Scientists, and Engineers*. Academic Press, 1988.

[60] Miltat J., Albuquerque G., and Thiaville A. “Spin Dynamics in Confined Magnetic Structures”. In: *Topics in Applied Physics, Springer* 83 (2002).

[61] Charles Kittel. “On the Theory of Ferromagnetic Resonance Absorption”. In: *Phys. Rev.* 73 (2 1948), pp. 155–161.

[62] Jeffrey McCord et al. “Tuning of magnetization dynamics by ultrathin antiferromagnetic layers”. In: *Applied Physics Letters* 92.16, 162506 (2008), p. 162506.

[63] R.W. Damon and J.R. Eshbach. “Magnetostatic modes of a ferromagnet slab”. In: *Journal of Physics and Chemistry of Solids* 19.3–4 (1961), pp. 308 –320.

[64] Anjan Barman and Arabinda Haldar. “Chapter One - Time-Domain Study of Magnetization Dynamics in Magnetic Thin Films and Micro- and Nanostructures”. In: vol. 65. Solid State Physics. Academic Press, 2014, pp. 1 –108.

[65] Babak Mozooni and Jeffrey McCord. “Direct observation of closure domain wall mediated spin waves”. In: *Applied Physics Letters* 107.4 (2015), p. 042402.

[66] John Kerr. “On rotation of the plane of polarization by reflection from the pole of a magnet”. In: *Philosophical Magazine Series* 5 (1877), pp. 321–343.

[67] O.V. Borovkova et al. “Transverse magneto-optical Kerr effect at narrow optical resonances”. In: *Nanophotonics* 8.2 (2019).

[68] E. F. Kingsbury. “THE KERR ELECTROSTATIC EFFECT”. In: *Review of Scientific Instruments* 1.1 (1930), pp. 22–32.

[69] Babak Mozooni, Thomas von Hofe, and Jeffrey McCord. “Picosecond wide-field magneto-optical imaging of magnetization dynamics of amorphous film elements”. In: *Phys. Rev. B* 90 (5 2014), p. 054410.

[70] B. E. Argyle and J. G. McCord. “New laser illumination method for Kerr microscopy”. In: *Journal of Applied Physics* 87.9 (2000), pp. 6487–6489.

[71] D.O. Smith. In: *J. Appl. Phys.* 29 (1958), p. 264.

[72] Peter Wolf. “Free Oscillations of the Magnetization in Permalloy Films”. In: *Journal of Applied Physics* 32.3 (1961), S95–S96.

[73] Anthony B. Kos, Thomas J. Silva, and Pavel Kabos. “Pulsed inductive microwave magnetometer”. In: *Review of Scientific Instruments* 73.10 (2002), pp. 3563–3569.

[74] Sangita S. Kalarickal et al. “Ferromagnetic resonance linewidth in metallic thin films: Comparison of measurement methods”. In: *Journal of Applied Physics* 99.9, 093909 (2006), p. 093909.

[75] T.J. Silva et al. “Inductive measurement of ultrafast magnetization dynamics in thin film Permalloy”. In: *J. Appl. Phys.* 85 (1999), pp. 7849–7862.

[76] G. M. Sandler et al. “Determination of the magnetic damping constant in NiFe films”. In: *Journal of Applied Physics* 85.8 (1999), pp. 5080–5082.

[77] D.V. Berkov. “Micromagnetic simulations of the magnetization dynamics in nanostructures with special applications to spin injection”. In: *J. Magn. Magn. Mat.* 300 (2006), pp. 159–163.

[78] Thomas von Hofe et al. “Dual wavelength magneto-optical imaging of magnetic thin films”. In: *Applied Physics Letters* 103.14, 142410 (2013), pp. –.

[79] M.L. Mallary. “Conduction of flux at high frequencies in Permalloy stripes by small-angle rotations”. In: *J. Appl. Phys.* 57.1 (1985), p. 3952.

[80] K. Ohashi. “Mechanism of 90 ° wall motion in thin film heads”. In: *IEEE Trans. Magn.* 21.5 (1985), pp. 1581–1583.

[81] B. C. Webb et al. “High-Frequency Permeability of Laminated and Unlaminated, Narrow, Thin-Film Magnetic Stripes”. In: *J. Appl. Phys.* 69.8 (1991), pp. 5611–5615.

[82] N. Smith. “Dynamic Domain Model for Magnetic Thin-Films”. In: *IEEE Transactions on Magnetics* 27.2 (1991), pp. 729–741.

[83] W. P. Jayasekara, J. A. Bain, and M. H. Kryder. “High frequency initial permeability of NiFe and FeAlN”. In: *IEEE Transactions on Magnetics* 34.4 (1998), pp. 1438–1440.

[84] U. Queitsch et al. “Domain wall induced modes of high-frequency response in ferromagnetic elements”. In: *J. Appl. Phys.* 100.9 (2006), p. 093911.

[85] C. Patschureck et al. “Magnetization dynamics of buckling domain structures in patterned thin films”. In: *Physical Review B* 86.5 (2012), p. 054426.

[86] Alex Hubert and Rudolf Schäfer. *Magnetic Domains - The Analysis of Magnetic Microstructures.* Berlin: Springer, 1998.

[87] M. Wolf, R. Schäfer, and J. McCord. “Precessional frequency of ferromagnetic elements: Influence of magnetic domain width”. In: *Journal of Magnetism and Magnetic Materials* 321.18 (2009), pp. 2920–2924.

[88] C. Patschureck et al. “Magnetic domain compensation effect on the magnetodynamic response of ferromagnetic elements”. In: *Appl. Phys. Lett.* 97.5 (2010), p. 052507.

[89] R. W. Damon and J. R. Eshbach. “Magnetostatic Modes of a Ferromagnetic Slab”. In: *J. Appl. Phys.* 31.5 (1960), p. 104.

[90] K. Yu. Guslienko et al. “Effective dipolar boundary conditions for dynamic magnetization in thin magnetic stripes”. In: *Physical Review B* 66.13 (Oct. 2002), p. 132402.

[91] K. Y. Guslienko, R. W. Chantrell, and A. N. Slavin. “Dipolar localization of quantized spin-wave modes in thin rectangular magnetic elements”. In: *Physical Review B* 68.2 (2003), p. 024422.

[92] P. M. Pimentel et al. “Kerr microscopy studies of microwave assisted switching”. In: *Journal of Applied Physics* 102.6 (2007), p. 063913.

[93] M. Mallary and A.B. Smith. “Conduction of flux at high frequencies by a charge-free magnetization distribution”. In: *IEEE Trans. Magn.* 24.6 (1988), p. 2374.

[94] J. Mullenix et al. “Spin-wave resonances in the presence of a Bloch wall”. In: *Phys. Rev. B* 89 (22 2014), p. 224406.

[95] T. A. Ostler et al. “Ultrafast heating as a sufficient stimulus for magnetization reversal in a ferrimagnet”. In: *Nat. Commun.* 3 (2012), p. 666.

[96] D. Chumakov et al. “Nanosecond time-scale switching of permalloy thin film elements studied by wide-field time-resolved Kerr microscopy”. In: *Phys. Rev. B* 71.1 (2005), p. 014410.

[97] C. Hengst et al. “Acoustic-domain resonance mode in magnetic closure-domain structures: A probe for domain-shape characteristics and domain-wall transformations”. In: *Phys. Rev. B* 89.21 (2014), p. 214412.

[98] U. Queitsch et al. “Domain wall induced modes of high-frequency response in ferromagnetic elements”. In: *J. Appl. Phys.* 100.9, 093911 (2006), p. 093911.

[99] J. P. Park et al. “Imaging of spin dynamics in closure domain and vortex structures”. In: *Phys. Rev. B* 67 (2 2003), p. 020403.

[100] J. P. Park et al. “Spatially Resolved Dynamics of Localized Spin-Wave Modes in Ferromagnetic Wires”. In: *Phys. Rev. Lett.* 89 (27 2002), p. 277201.

[101] S. W. Yuan and H. N. Bertram. “Magnetic Thin-Film Domain-Wall Motion under Dynamic Fields”. In: *J. Appl. Phys.* 72.3 (1992), pp. 1033–1038.

[102] B. Mozooni, T. von Hofe, and J. McCord. “Picosecond wide-field magneto-optical imaging of magnetization dynamics of amorphous film elements”. In: *Phys. Rev. B* 90 (5 2014), p. 054410.

[103] L. Thomas et al. “Oscillatory dependence of current-driven magnetic domain wall motion on current pulse length”. In: *Nature* 443 (2006), pp. 197–200.

[104] Giacomo Talmelli et al. “Spin-Wave Emission by Spin-Orbit-Torque Antennas”. In: *Phys. Rev. Applied* 10 (4 2018), p. 044060.

[105] I Neudecker et al. “Imaging magnetic excitations in confined magnetic structures”. In: *Journal of Physics D: Applied Physics* 41.16 (2008), p. 164010.

[106] Mathis Lohman, Babak Mozooni, and Jeffrey McCord. “Homogeneous microwave field emitted propagating spin waves: Direct imaging and modeling”. In: *Journal of Magnetism and Magnetic Materials* 450 (2018), pp. 7 –12.

[107] Henning Ulrichs, Benjamin Lenk, and Markus Münzenberg. “Magnonic spin-wave modes in CoFeB antidot lattices”. In: *Applied Physics Letters* 97.9 (2010), p. 092506.

[108] Andrzej Wawro et al. “Magnetic Properties of Coupled Co/Mo/Co Structures Tailored by Ion Irradiation”. In: *Phys. Rev. Applied* 9 (1 2018), p. 014029.

[109] M. E. Schabes, E. E. Fullerton, and D. T. Margulies. “Theory of antiferromagnetically coupled magnetic recording media”. In: *IEEE Transactions on Magnetics* 37.4 (2001), pp. 1432–1434.

[110] X. M. Liu, J. Ding, and A. O. Adeyeye. “Magnetization dynamics and reversal mechanism of Fe filled Ni80Fe20 antidot nanostructures”. In: *Applied Physics Letters* 100.24 (2012), p. 242411.

[111] R. P. Cowburn, A. O. Adeyeye, and J. A. C. Bland. “Magnetic domain formation in lithographically defined antidot Permalloy arrays”. In: *Applied Physics Letters* 70.17 (1997), pp. 2309–2311.

[112] S. Neusser et al. “Spin-wave localization between nearest and next-nearest neighboring holes in an antidot lattice”. In: *Applied Physics Letters* 93.12, 122501 (2008), p. 122501.

[113] D. Tripathy J. Ding and A. O. Adeyeye. “Dynamic response of antidot nanostructures with alternating hole diameters”. In: *EPL (Europhysics Letters)* 98.1 (2012), p. 16004.

Index